2008

High Intensity Laser Power Beaming for Wireless Power Transmission

Daniel Edward Raible
Cleveland State University

HIGH INTENSITY LASER POWER BEAMING

FOR WIRELESS POWER TRANSMISSION

DANIEL EDWARD RAIBLE

Bachelor of Electrical Engineering

Cleveland State University

May, 2006

submitted in partial fulfillment of requirements for the degree

MASTER OF SCIENCE IN ELECTRICAL ENGINEERING

at the

CLEVELAND STATE UNIVERSITY

May, 2008

This thesis has been approved

for the Department of Electrical and Computer Engineering

and the College of Graduate Studies by

_____

Advisor, Taysir H. Nayfeh

_____

Department/Date

_____

Thesis Committee Co-Chairperson, Fuqin Xiong

_____

Department/Date

_____

Ana V. Stankovic

_____

Department/Date

_____

Petru S. Fodor

_____

Department/Date

To my family…

ACKNOWLEDGEMENTS

HIGH INTENSITY LASER POWER BEAMING

FOR WIRELESS POWER TRANSMISSION

DANIEL EDWARD RAIBLE

ABSTRACT

This paper describes work supporting the development of a high intensity laser power beaming (HILPB) system for the purpose of wireless power transmission. The main contribution of this research is utilizing high intensity lasers to illuminate vertical multi-junction (VMJ) solar cells developed by NASA-GRC. Several HILPB receivers are designed, constructed and evaluated with various lasers to assess the performance of the VMJ cells and the receiver under a variety of conditions. Several matters such as parallel cell back-feeding, optimal receiver geometry, laser wavelength, non-uniform illumination and thermal effects at high intensities are investigated. Substantial power densities are achieved, and suggestions are made to improve the performance of the system in future iterations. Thus far, the highest amount of energy obtained from a receiver during these tests was 23.7778 watts. In addition, one VMJ cell was able to achieve a power density of 13.6 watts per cm^2, at a conversion efficiency of 24 %. These experiments confirm that the VMJ technology can withstand and utilize the high intensity laser energy without damage and/or significant reduction in the conversion efficiency.

TABLE OF CONTENTS

Page

NOMENCLATURE

ISSL: Industrial Space Systems Laboratory

CSU: Cleveland State University

AFRL: Air Force Research Laboratory

NGST: Northrop Grumman Space Technology

LIMO: Lissotschenko Mikrooptik GmbH

LASER: Light Amplification by Stimulated Emission of Radiation

HILPB: High Intensity Laser Power Beaming

VMJ: Vertical Multi-Junction

NASA: National Aeronautics and Space Administration

GRC: Glenn Research Center

PV: Photovoltaic

RFID: Radio-Frequency Identification

TET: Transcutaneous Energy Transfer

UAV: Unmanned Aerial Vehicle

COTS: Commercial off the Shelf

MPT: Microwave Power Transmission

CBS: Columbia Broadcasting System

JPL: Jet Propulsion Laboratory

SHARP: Stationary High Altitude Relay Platform

MWLC: Micro-Wave Light Craft

LEO: Low Earth Orbit

GEO: Geosynchronous Orbit

SBM: Space-Based Microwave

PS: Power Sphere

PVCC: Photovoltaic Cavity Converter

EADS: European Aeronautic Defense and Space Company

POWOW: Power With Out Wires

I-V: Current-Voltage Relationship

I_{sc}:   Short-Circuit Current

V_{oc}:   Open Circuit-Voltage

V_{mp}:   Maximum Power Voltage

I_{mp}:   Maximum Power Current

P_{mp}:   Maximum Power

FF: Fill Factor

Ŋ%:   Conversion Efficiency

QE: Quantum Efficiency

LAPSS: Large Area Pulsed Solar Simulator

TEM_{00}: Transverse Electro-Magnetic Gaussian

DPAL: Diode Pumped Alkali Vapor Laser

HEL: High Energy Laser

ATP: Acquisition Tracking & Pointing

ABL: Airborne Laser

TBM: Tactical Ballistic Missiles

IR: Infra-Red

PCB: Printed Circuit Board

CFM: Cubic Feet per Minute

RPM: Revolutions per Minute

FPGA: Field Programmable Gate Array

GUI: Graphical User Interface

FET: Field Effect Transistor

LIST OF TABLES

LIST OF FIGURES

Figure   **Page**

xvii

CHAPTER I

INTRODUCTION

Although the notion of wireless power transmission is now almost 200 years old, it remains innovative as ever while developing technology pursues the concept. New advances in solid state light amplification by stimulated emission of radiation (lasers) and photovoltaic (PV) technologies generate an opportunity to revisit this concept. The implementation of the high intensity laser power beaming (HILPB) system will extend the capabilities of existing applications here on Earth, and create many new avenues for the exploration of our universe.

1.1 Overview and Applications of Wireless Power Transmission

Wireless power transmission is the process by which electrical energy is sent from a power source to a load, without the use of conventional interconnecting wires. This is ideal in applications where either an instantaneous amount or a continuous delivery of energy is needed, but where conventional conduction wires are prohibitively inconvenient, expensive, hazardous or impossible.

The underlying physics of wireless power transmission resembles that of wireless communications, but with an important difference. Unlike information transfer, where the percentage of received power must be only sufficiently high enough to recover the signal, wireless power transmission places a critical emphasis on the maximum amount of possible energy transfer and conversion efficiency. Ideally, a wireless power transmission system would have the ability to transmit any amount of power to any point in space, but practical limitations such as conversion efficiencies at the source and the receiver, and disturbances in the transmission medium will always limit the performance of an implemented system.

Low-level and short-range wireless power transfer has found niche applications in everyday life, such as with radio-frequency identification (RFID) tags, induction charging of portable consumer electronics, electromagnetic card readers and transcutaneous energy transfer (TET) systems in artificial hearts and other surgically implanted devices [8].

Wireless power transfer is a revolutionary concept whose full potential has yet to be realized. High intensity long-range transmission is an enabling technology, by extending the capabilities of existing applications and facilitating the development for completely new paradigms. A HILPB system will have the potential to connect lunar habitats, landing sites and power-plants. It will have the capability to deliver energy indefinitely to remote vehicles and crafts such as unmanned aerial vehicle (UAV) swarms, high altitude airships, orbiting satellites, extra-terrestrial robotic rovers and deep space probes, thereby increasing their coverage, autonomy and endurance. A high intensity long range wireless power transmission system could be used to relay power

from a solar farm or a nuclear reactor to the dark side of the moon, and can be easily reconfigured to serve as a flexible virtual power grid.

The concept of a long range wireless power transmission system has been ahead of its practical implementation for a long time, but this gap is shrinking. The current state of the art in technology is providing for a high intensity long range wireless power transmission system to be designed using many commercial off-the-shelf (COTS) components. The vast application potential makes the pursuit of the HILPB system a worthwhile endeavor.

1.2 Existing Work in Wireless Power Transmission

The discussion of significant amounts of wireless power transmission began with Nikola Tesla near the end of the nineteenth century. Tesla built upon his previous research in radio transmission to successfully design, construct and demonstrate several wireless power transmitters. His designs were operated on the principles of electromagnetic radiation through tuned circuitry. Although he could power light bulbs and vacuum tubes within the vicinity of his transmitters, Tesla had a much broader vision for where his technology should be used. Rather than stringing up copper conductors on wooden poles in an effort to connect the country to a power distribution grid, he envisioned a worldwide system of radiated energy. His large scale experiments probed

the very fabric of our Earth's electrical conduction characteristics in an effort to exploit it for this purpose.

Although Tesla was not afforded an opportunity to complete his research, much of his work is being revisited today for applications such as virtual lightning rods and weaponry. The potentially volatile nature of this technology due to the large amounts of uncontrollable radiated energy has partially prevented it from gaining support for wireless power transmission applications.

Around the middle of the twentieth century, research on applying microwave communications technology to wireless power transmission was started. This work mainly focused on utilizing the technology to transmit energy from solar power satellites down to Earth, or to provide power and propulsion to other spacecraft. Several large scale ground based microwave demonstrators have been constructed and operated. The drawback to this technology is that microwaves have very long wavelengths which exhibit a moderate amount of diffraction over long distances. This necessitates a large power receiver dish, which limits the flexibility of this technology to certain applications. The ability for HILPB to focus large amounts of power to a small aperture across long distances is what separates it from the microwave technology, and this broadens the number of potential applications for the technology.

1.3   New Approaches, Laser Power Beaming

Since Schawlow and Towne's early patented ideas at Bell Labs [1 and 2] which led to the development of laser technology, wireless power transmission has been a considered application. The laser's efficient atmospheric propagation window, and its ability to deliver large amounts of photonic energy to a small aperture make it an ideal source for wireless power transmission. Original research proposed the use of lasers to provide thermal energy for beamed energy propulsion to spacecraft. Later, it was proposed to use the laser with a photovoltaic receiver, to effectively beam electrical power from one location to another. The main limiting factors to the laser power beaming (LPB) system are the conversion efficiencies of the laser (electrical to photonic) and the photovoltaic cells (photonic to electrical). The advancement of both of these technologies is allowing for greater power handling capacities and conversion efficiencies. However, although there are a variety of photovoltaic cells on the market approaching conversion efficiencies of 40 % (such as triple junction cells), these technologies cannot operate at intensities 1000 times or greater than that of the sun.

This work proposes the use of vertical-multi junction (VMJ) photovoltaic cells for utilization in the laser power beaming application. These cells were originally developed by NASA-GRC scientists and are currently produced by Photovolt, Inc. for high intensity solar energy applications (greater than 2500 suns), such as parabolic and Fresnel solar concentrators. VMJ cells offer high power density and conversion efficiencies through

the use of edge-illuminated semiconductor junctions and can operate at favorable laser wavelengths.

1.4   Research Objectives

The first objective of this work is to design, construct and test a preliminary engineering model of a HILPB receiver as a proof-of-concept hardware device. The receiver needs to meet the thermal and electrical demands of the system, and will be tested with various laser sources to evaluate the performance of the VMJ cells for this application. Next, the receiver design needs to be refined, in order to demonstrate substantial power densities and conversion efficiencies. This will be accomplished by investigating matters such as the parallel-cell back-feeding, optimal receiver geometry, non-uniform illumination and thermal effects at high intensities. New iterations of the receiver will be designed, constructed and tested to support these investigations and to provide solutions to problems encountered during development. Finally, suggestions will be made to improve the future performance of the design, based on the analysis of the data collected from these experiments.

1.5   Document Overview

This paper is organized as follows: Chapter 2 investigates the history of wireless power transfer, from the early days of induction and electromagnetic radiation, to microwave power transmission and finally laser power beaming. The enabling PV and laser technologies for HILPB are discussed in Chapter 3. The experimental apparatus are described in Chapter 4, including the design, construction and validation of the HILPB receivers and the supporting electronics. Chapter 5 contains the experimental results and conclusions concerning issues such as parallel cell array back-feeding, optimal receiver geometry and proper laser wavelengths to maximize conversion efficiency, the impact of non-uniform beam distribution and thermal effects at high intensities. Finally, Chapter 6 offers a summary of the results and suggestions for future work.

CHAPTER II

HISTORY OF LONG-RANGE WIRELESS POWER TRANSFER

From the beginnings of wireless power transfer with the prolific Tesla literally igniting the world on fire with his kilovolts of energy, the prospects of a large scale system have engaged many researchers to push the technology further. Airships, lunar bases and spacecraft applications have been identified as benefactors of this concept, and as the technology progresses so do the capabilities of the wireless power transmission systems.

2.1   Electromagnetic Radiation

The origins of wireless power transfer can be traced back to the first half of the nineteenth century with the invention of the electromagnet by William Sturgeon, the discovery of electromagnetic induction by Michael Faraday and the mathematical modeling of electromagnetic radiation by James Maxwell. These discoveries were combined and demonstrated by Nicholas Callan's construction of the induction coil and Guglielmo Marconi's Hertz-wave transmitter apparatus, but it wasn't until Nikola Tesla's

coupled-tuned-circuit oscillator that the concept of wireless power transmission became widely known. His vision of a "world system for the transmission of electrical energy without wires" [3, 4 and 5] led him to design his own transmitter, whose power handling capacity was five orders-of-magnitude greater than those of its predecessors. It consisted of two flat coil variations of his Tesla coil design, with the capability to tune its operating frequency.

Tesla's apparatus was demonstrated as early as 1891 in his New York laboratories. While conducting an experiment, his electro-mechanical oscillators started to generate a resonant frequency in the surrounding buildings, causing them to shake violently. As the speed of the oscillators grew, he hit the resonant frequency of his own laboratory, and had to terminate the experiment with a sledgehammer to avoid a catastrophe. During these experiments, the radiated energy lit up vacuum tubes within the proximity of the oscillators, providing impressive evidence for the potential of wireless power transmission. This type of electrical conduction (the movement of energy through space and matter, and not just the production of voltage across a conductor) was named the Tesla effect.
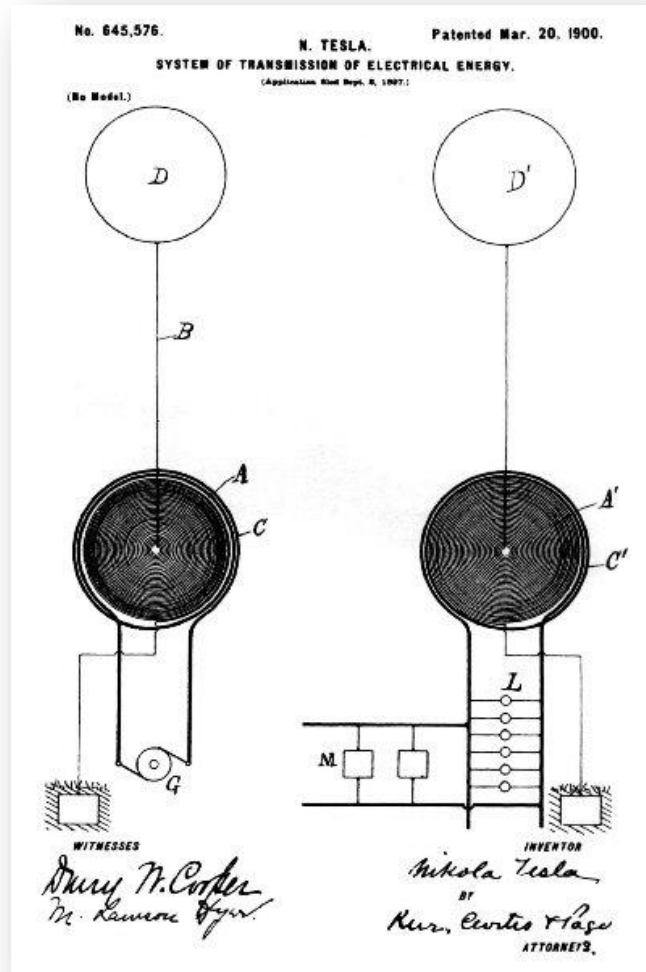
Figure 1:   Tesla's Wireless Energy Apparatus [3]

Tesla demonstrated his wireless power transmission method to the public over the next few years, including the 1893 World Fair at Chicago where he powered fluorescent lamps and single node bulbs with his apparatus. He delivered a well received demonstration lecture to the Institute of Electrical Engineers (IEE) in London and the American Institute of Electrical Engineers (AIEE) in New York City, which fueled his desire to design and construct a large scale wireless power transmission demonstrator.
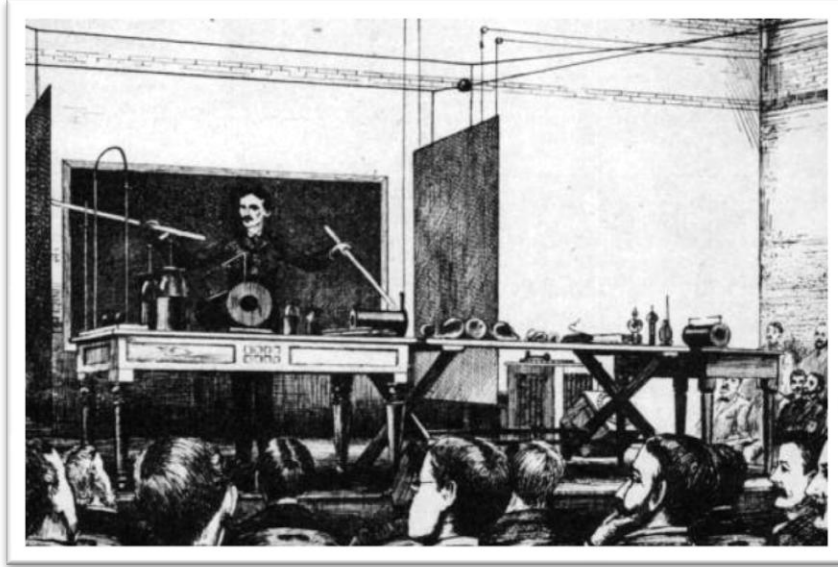
Figure 2:   Tesla's Wireless Energy Lecture - *Wikipedia*

By 1900, he applied for patents describing improvements to his system [3, 4 and 5], and he began construction of his large 187 foot Wardenclyffe Tower facility on Long Island to conduct his high-voltage, high-frequency experiments. The main focus of Wardenclyffe was to serve as a wireless power transmission facility, and allow him to increase the intensity of the generated electrical oscillations. This was to be the first of many such installations around the world, thus creating a global system of multi-channel broadcasting and wireless industrial transmission of electric power.
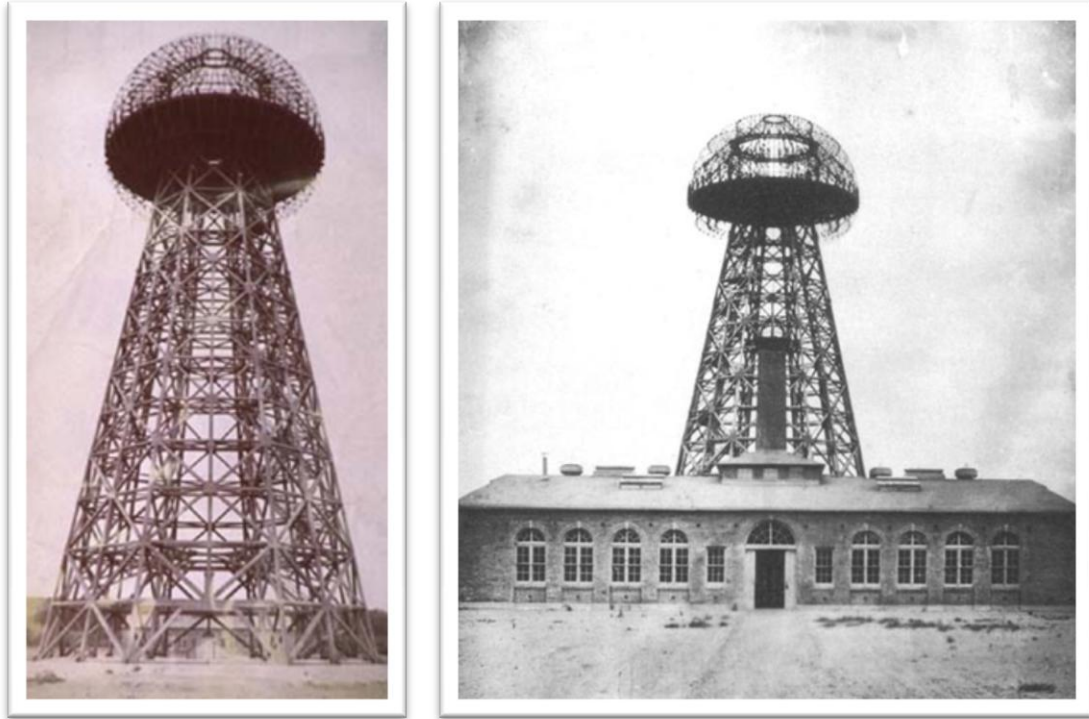
Figure 3:   Tesla's Wardenclyffe Tower - *Wikipedia*

At Wardenclyffe, he operated across a range of frequencies from 1 kHz to 100 kHz at powers up to 1.5 MW in an effort to excite and exploit the Earth's inherent resonant LC circuits through the ionosphere and the natural ground. Excitation at these frequencies would yield the most economical method of power transmission, and his apparatus indicated an efficient range between $30 - 35$ kHz. Under certain conditions, he found that he could send pulses of electricity through the air with undiminished strength by setting up a longitudinal acoustic-type compression wave, rather than an electromagnetic Hertzian-type transverse wave. He could also include a stationary resonant wave within the earth-ionosphere cavity, as well as add an 8 Hz component to resonate with the Earth's Schumann cavity to determine the most efficient method of the wireless transmission of power. These preliminary experiments revealed much about the

electrical nature of Earth, from its resistivity, capacitance and inductance, and these findings convinced Tesla that his large scale construction would not only work, but would be the beginning of greater technologies:

"As soon as [the Wardenclyffe facility is] completed, it will be possible for a business man in New York to dictate instructions, and have them instantly appear in type at his office in London or elsewhere. He will be able to call up, from his desk, and talk to any telephone subscriber on the globe, without any change whatever in the existing equipment. An inexpensive instrument, not bigger than a watch, will enable its bearer to hear anywhere, on sea or land, music or song, the speech of a political leader, the address of an eminent man of science, or the sermon of an eloquent clergyman, delivered in some other place, however distant. In the same manner any picture, character, drawing, or print can be transferred from one to another place ..." – N. Tesla [6]

Unfortunately the Wardenclyffe Tower facility was never fully completed, due to Tesla's economic hardship partially resulting from the US Patent Office revoking his earlier patent for the radio and awarding it to Marconi. By 1917, the tower was dismantled, and his large scale vision of wireless power transmission was forfeited.

The viability of such a large-scale electromagnetic radiation system has yet to be demonstrated, and faces the key challenges of efficiently coupling power into and out of the earth-ionosphere cavity through its resonant modes, and in devising a small and efficient receiver [7]. Implementation concerns such as safety, susceptibility to weather and environmental impact have also limited the pursuit of this form of wireless power transmission.

Recently, a group of researchers at MIT have revisited Nikola Tesla's original idea of transporting energy over a distance without a carrier medium using electromagnetism. They identified the impracticality of radiating the energy in an Omni-directional manner, due to the large amount of energy that is wasted into free space. The focus of their research is on directional (rather than radiated) power transfer at mid-range distances (where the length of the transmission equals a few multiples of the size of the device) for autonomous mobile electronics applications such as laptops and cell phones. This is achieved by establishing near field resonant coupling between the objects, upon which energy can be transferred [8]. A demonstrator of this system has been constructed using self-resonant coils, and has achieved a transfer of 60 watts with 40 % efficiency over distances in excess of 2 meters [9]. The approximate practical transmission distance of this scheme is 8 times the radius of the coils, which would be the primary limiting factor when considering the end applications.

2.2   Microwave Power Transmission

Following the World War II development of high-power microwave emitters (called cavity magnetrons), the idea of using microwaves for wireless power transfer was researched. One of the main pioneers of this concept of microwave power transmission (MPT) was William Brown, who in 1964 on CBS News with Walter Cronkite, demonstrated a microwave-powered model helicopter that received all of its flight power from a microwave beam [10]. MPT for a proposed micro-helicopter application was later

revisited and demonstrated using a 1.3 GHz continuous wave at 1 watt of transmitted power, nearing efficiencies of 31 % [11].
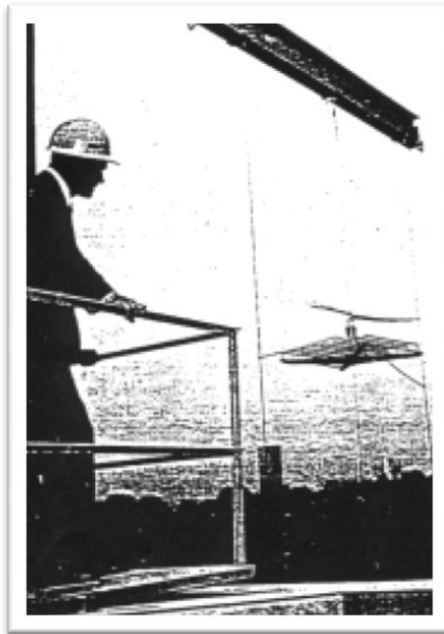
Figure 4:   W. C. Brown with MPT Helicopter [10]

Brown later served as technical director of a JPL-Raytheon program between 1969 and 1975 that beamed 30 kW over a distance of 1 mile at 84 % efficiency. Further MPT experiments in the tens of kilowatts have been conducted at the JPL Goldstone Deep Space Communications Complex in California in 1975 [12, 13 and 14] and more recently (1997) at Grand Bassin on Reunion Island [15].

Figure 5:   JPL Ground-to-Ground MPT Experiment [12]

Following the MPT research of W.C. Brown, notable field experiments have been conducted such as the Stationary High Altitude Relay Platform (SHARP) in Canada which utilized 2.45 GHz to successfully power a large scale fuel free aircraft [16]. The SHARP concept envisions a microwave powered airplane circling at a 21 km altitude for the purpose of distributing telecommunications services within a 600 km region. A 1/8 scale model of the aircraft was constructed and successfully flown.

Figure 6:   1/8 SHARP Flight Experiment Model [16]

A similar fuel-free airplane flight experiment using a MPT phased array with 2.411 GHz in 1992 was conducted in Japan [17]. The target application was another high altitude long endurance airship. A rectenna (rectifying antenna) was designed to employ a dual polarization technique to double the microwave power flux density, and this array was mounted on an airship which had a successful microwave powered flight test lasting 3 minutes and a demonstrated radio frequency to direct current conversion efficiency of 81 %.

Figure 7:   Phased Array Model Airplane Experiment [17]

One particular endoatmospheric application of MPT is to provide power to pulsed particle accelerators for an ion propulsion mode Micro-Wave Light Craft (MWLC). This type of vehicle would be able to achieve hypersonic velocities at 100 to 1000X cost reduction over conventional chemical propulsion methods.   This concept was demonstrated in 2003 by transmitting 3 kW of 5.85 Ghz microwave power to a remote rectenna [18]. The rectenna delivered 6 kV to a special 'Ion Breeze' engine, which applied a torque to the charged hull for pitch and roll maneuvers (Figure 8). This demonstrated the feasibility of using MPT for endoatmospheric ion propulsion.

Figure 8:   Microwave Transmitter (left) and Rectenna [18]

The inherent nature of the microwave propagation lends itself to dual use wireless power beaming and data telemetry applications. A communications signal could be modulated on top of the power transfer, or in the case of a multifunctional stacked patch antenna, an optimized dual mode system could be developed. A proposal has been made for antennae that operate with 10 dBi of gain and 18 % bandwidth at 5.8 GHz, and 4 dBi of gain and 3.2 % bandwidth at 2.45 GHz [19]. The ability to switch between these modes would allow for a system that could provide for a wireless power transmission at high frequencies and data telemetry at lower frequencies, thereby obtaining dual usage from a single technology.

The deployment of a MPT infrastructure in Low Earth Orbit (LEO) would have the potential to radically reduce the cost of space missions by factors of 100 to 1000 times. A space-based microwave (SBM) power station would offer operational flexibility by providing a power boost to heavy lift launch vehicles from the ground, to light-craft

ascending from LEO to Geosynchronous Orbit (GEO) (Figure 9) and other orbital vehicles & satellites within the station's power beaming range [20]. The proposed station may be up to 1 km in diameter, and use 320 MW of photovoltaic arrays as a means to operate a 20 GW microwave for a short duration of time.
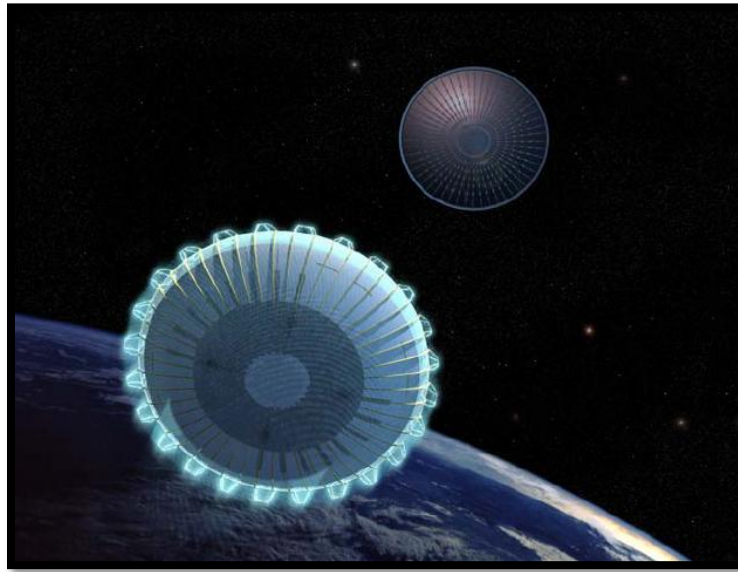
Figure 9:   Light-craft Ascending a Microwave Beam [20]

2.3   Laser Power Beaming

During the past decade, there have been many valued applications for HILPB that have been identified and assessed. The development of a practical HILPB system has been slow due to the significant non-reoccurring engineering costs of the components, but these technologies are continually being improved for applications in other fields. The benefits from these improvements can translate to the realization of a HILPB system.

One such work under development is the PowerSphere (PS) [21], which is a high efficiency Photovoltaic Cavity Converter (PVCC). The PS has a target power range of 1 kW to 100 kW, and at this time it is functioning within the 100 watt to 200 watt level using a Nd:YAG laser operating at 1.064 μm. The current PVCC prototype is constructed from 22 Si concentrator cells (limited to 500 suns), and the overall array efficiency is 14 %. This prototype needs to be optimized by perfectly matching the photovoltaic cell band gaps to the laser frequency, reducing the 15 % reflectance in the anti-reflective (AR) coating of the cells, increasing the flux density inside of the sphere (currently it is 30 % less than one sun) and increasing the cell population density within the PVCC. These limitations will need to be overcome in order for the PS to become a practical for HILPB.
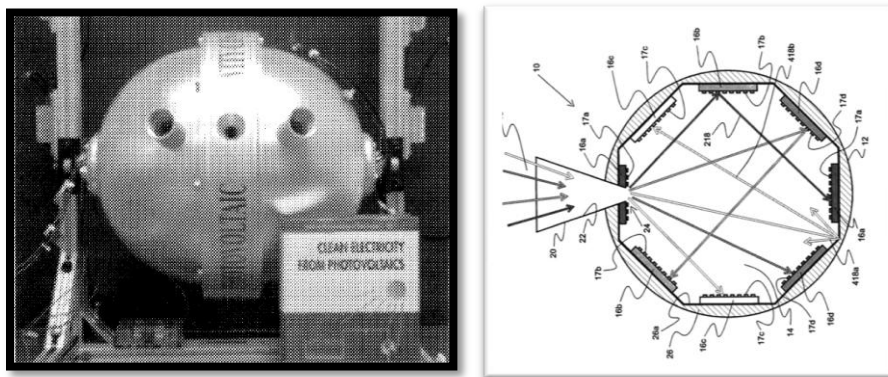
Figure 10: PVCC and its Concept Layout [21]

In the past, researchers have demonstrated a variety of model aircraft being powered using beamed microwave energy. The limitation to this technology is the energy loss caused by the microwave beam dispersion, which prohibits long-distance power transfer. The focused characteristic of a laser beam when compared to that of a

microwave beam makes it a natural choice for practical power beaming. The first successful flight demonstration of a small-scale aircraft flying under the power delivered from a laser was conducted at NASA's Marshall Space Flight Center in 2003 [22]. A lightweight, 11 ounce aircraft was fitted with a custom Spectrolab thin film photovoltaic panel, consisting of triple junction Ga:In:P2 cells. Because these cells could not individually handle the high energy densities of the laser, the beam had to be spread out over an array of 24 cells which hung from the fuselage of the aircraft, as shown in Figure 11.
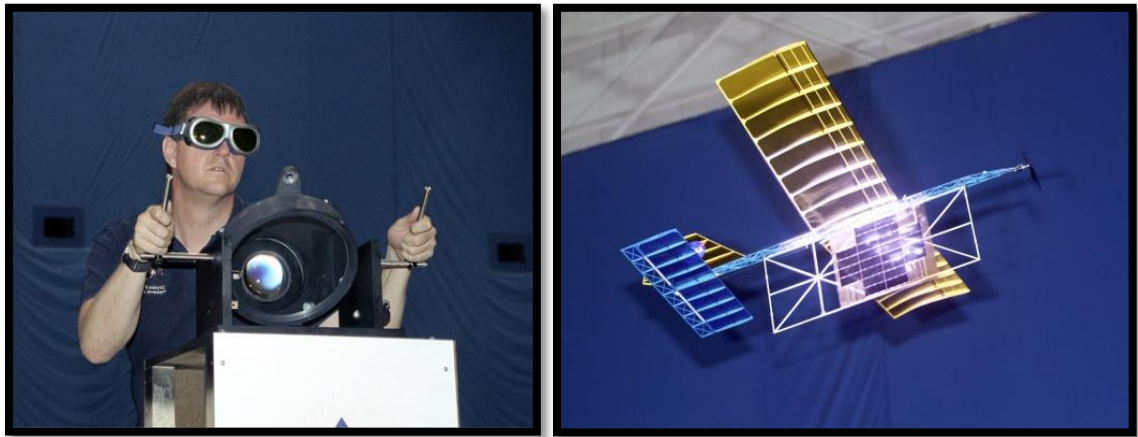
Figure 11: First Laser Powered Aircraft Flight [22]

The aircraft was flown in a continuous circle inside of a large building, and an operator manually tracked its flight path with an adjustable 1.5 kW laser at 940 nm with an approximate distance of 15 meters. At a laser intensity of 500 watts (39.56 watts irradiating the panel), the photovoltaic receiver was able to provide 7 watts of power to the motor, which was sufficient to sustain flight. This experiment demonstrated a 17.7 %

efficiency of the loaded cells. The experiment was re-attempted outdoors, but the small aircraft could not handle the wind conditions.

More recently than the NASA flight endeavor, engineers at the EADS Space Transportation facility successfully powered a mini-rover with a laser [23]. A tracking system was developed to maintain an orthogonal angle between the photovoltaic cell panel and the laser beam, and the test was conducted at a range of 250 meters.
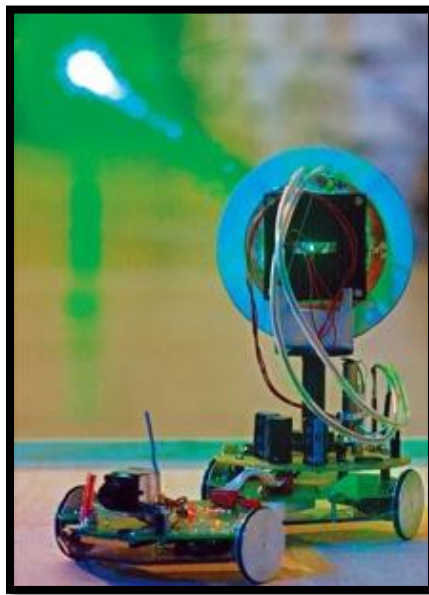
Figure 12: EADS Laser Powered Mini-rover [23]

One of the future applications for laser power beaming in space exploration may be Power With Out Wires (POWOW) [24]. The POWOW concept is a solar electric spacecraft for the purpose of running cargo to and from Mars. The spacecraft would be fitted with high efficiency solar cells and an electric propulsion system, and once in orbit of the planet, it could beam power down to the Martian surface using lasers. By delivering power in this fashion, the surface infrastructure could be reduced. Laser

power beaming is optimal for this application, because at an aero-synchronous orbit distance of 17,000 km, a laser receiver would have an aperture area of 360 meters^2 to contain the beam. This is considerably smaller than if MPT were used.

Another application for HILPB in space is with space elevators. A space elevator is simply a 100,000 km carbon nano-tube composite cable attached to Earth at one end and a space platform at the other.
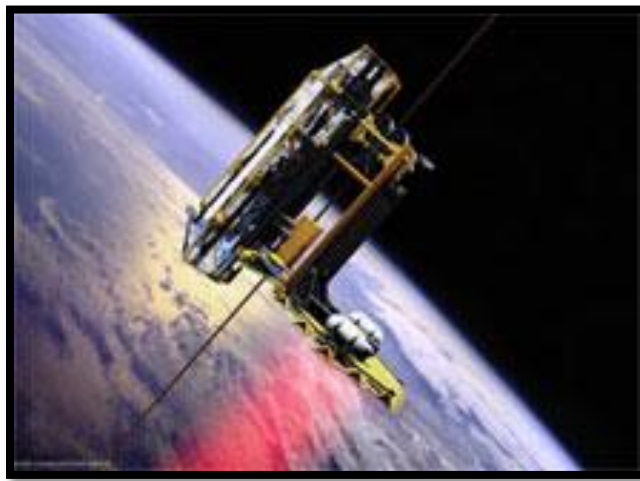
Figure 13: Spaceward Foundation Elevator

A mechanical climber ascends the cable for the purpose of carrying satellites into space, providing a cost effective alternative to conventional heavy lift space launch vehicles. With current developing technologies, a 20,000 kg capacity space elevator appears feasible at a cost of $40B [25]. Although the basic design and components of the space elevator have been worked out, the matter of delivering power to the climbers remains an issue. Ground-based HILPB is an ideal solution, since the area surrounding the cable will already be secure, and the target is stationary.

A further application of laser power beaming in space is to provide auxiliary power to satellites during periods of eclipse, to compensate for the solar panel degradation or after an electrical failure [26]. In this way, a laser-equipped satellite could take the place of the solar flux to effectively extend the mission duration of other degraded satellites.
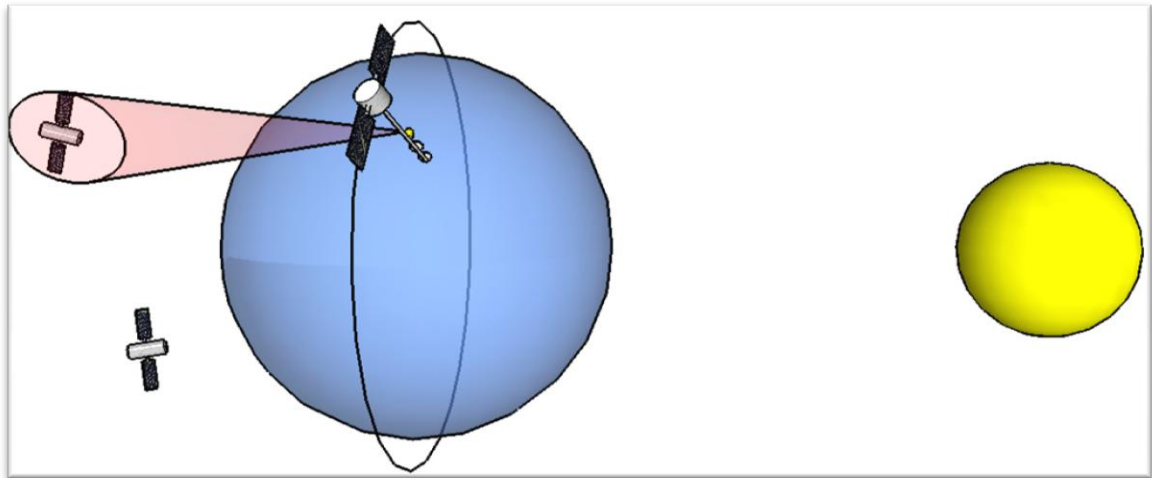
Figure 14: Beaming Power to an Obscured Satellite

CHAPTER III

ENABLING TECHNOLOGIES

The present technological maturity in PV devices, high power lasers and advanced control optics creates an opportunity to develop a HILPB system. Understanding the interaction of these technologies is fundamental to designing a successful system, in order to uncover potential problems that may require an engineering solution. This chapter describes the theory and functionality of the technologies employed for HILPB.

3.1   Photovoltaic's

The first section explains the fundamental properties of PV devices using a single-junction solar cell. These are compared and contrasted with the construction and characteristics of the vertical multi-junction (VMJ) cell in the second section.

3.1.1 Photovoltaic Theory
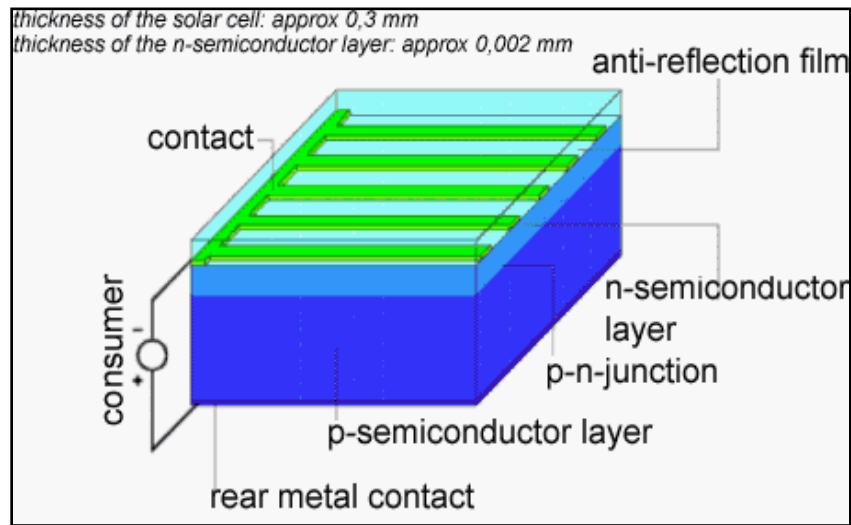
Figure 15: Cross Section of a Single-Junction Solar Cell

A solar cell is a semiconducting device that is typically made up of silicon (although other semiconducting materials may be used). During the manufacturing process boron and phosphor additives are doped into the silicon material, thus creating a p-type and an n-type material, respectively. The simplest topology of a photocell is a single p-n junction with metal contacts on either sides of the semiconductor stack. The front contacts only partially cover the n-type material to allow the impinging photonic energy to enter. These photons must have energy greater than or equal to the band-gap in the material in order for the cell to generate electricity. Photons with wavelengths greater than hc/E_g (where h is the Planck constant, c is the speed of light and E_g is the band-gap

27

energy) will promote electrons at a certain efficiency rate, and develop a photocurrent through the cell under a loaded condition. This process is referred to as the photoelectric effect, as mathematically described by Einstein [27]. Photons with energy less than the band-gap of the material will not make a contribution to the generated electricity due to the semiconductor recombination process, which results in the conversion to heat.

The band-gap of the photocell is determined by the semiconductor material used in its construction. This material is chosen to balance the design parameter tradeoff between high output voltages (high energy band-gaps) or high output currents (low energy band-gaps) [28].
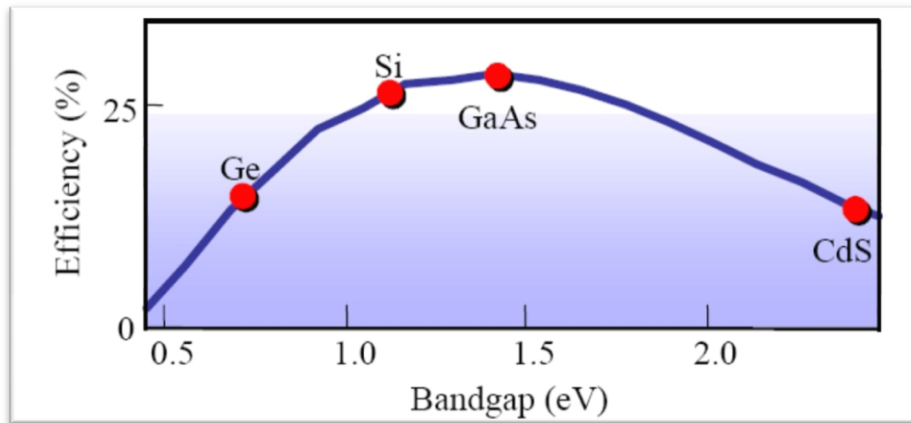
Figure 16: Optimal Band-Gaps for Semiconductors

When the photons enter the semiconducting material, they interact with the atoms in the lattice. The collision of a single photon with a single electron promotes that electron to a higher energy level, specifically the conduction band in the n-type material. The resulting hole in the valence band is swept across the junction field to the p-type material. In doing so, a field has been set up where conduction band electrons travel to

the n-type side, and valence holes travel to the p-type side, all while the photons continue to bombard the semiconductor. Once there, they cannot re-cross the junction, as this would oppose the field. This migration of the electrons in one direction and holes in the opposite direction builds up a separation of charge, which eventually overcomes the junction field to create a forward biased junction. When connected to a load the cell will discharge this potential energy across it, creating electrical power.
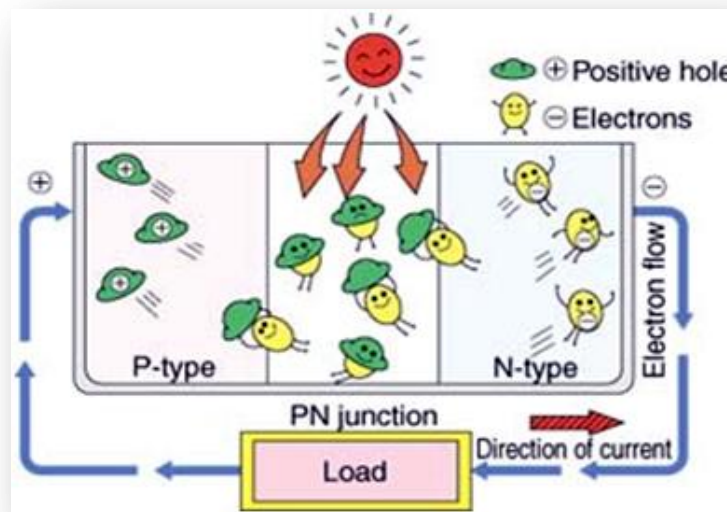
Figure 17: Illustration of Photovoltaic Theory

The performance of a solar cell can be evaluated by a few simple concepts.

a) Current-Voltage (I-V) Curves

The I-V curve describes the electrical characteristics of the solar cell across its operational range of voltages and currents. These curves are obtained by recording the voltage and current values of a cell exposed to a constant level of light and held at constant temperature while a variable resistive load is swept from open-circuit to short-

circuit states (from infinity to zero ohms). The resulting curve graphically represents typical electrical performance parameters required for characterization. I_{sc} refers to the short-circuit current when the output terminals of the cell are effectively connected together, and it intersects the vertical axis. At the opposite extreme of the curve, V_{oc} refers to the open circuit-voltage, and it intersects the horizontal axis.
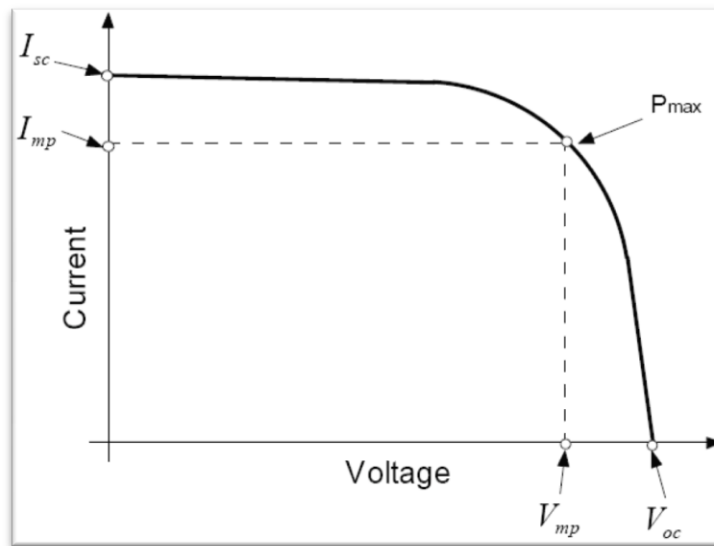
Figure 18: Typical Photovoltaic I-V Curve

b) <u>Maximum Power (P_{mp})</u>

The product of the voltage and the current at any point on the curve describes the electrical power output of the cell. The point where this is a maximum is denoted P_{max}, and the corresponding contributions are labeled V_{mp} and I_{mp}.

c) Fill Factor (FF)

Fill Factor describes the degree to which the values at V_{mp} and I_{mp} match the values at V_{oc} and I_{oc}. In other words, it describes the 'squareness' of the curve, and can be calculated by:

$$Fill\ Factor\ (FF) = \frac{V_{mp} \times I_{mp}}{V_{oc} \times I_{oc}} \times [\%] \tag{3.1}$$

d) Conversion Efficiency (η%)

The conversion efficiency of a photovoltaic cell is the percentage of the total incident energy on the device that is converted into electrical energy, as given by

$$Conversion\ Efficiency\ (\eta\%) = \frac{P_{mp}}{Incident\ Solar\ Energy} \times [\%] \tag{3.2}$$

e) Quantum Efficiency (QE)

Quantum Efficiency describes the relationship of the response of the cell to different wavelength components of incident light. It is the ratio of the number of charge carriers collected by the solar cell to the number of photons across the spectrum incident on the PV device. The Quantum Efficiency of the device is determined from its chemical makeup and its construction. This is generally optimized to best approximate the solar spectrum for maximum conversion efficiency at all frequencies, as shown in Figure 19.
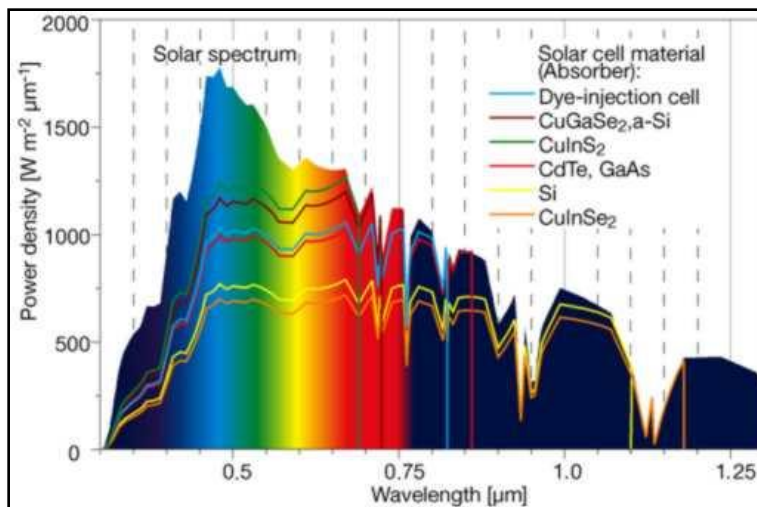
Figure 19: Hahn-Meitner Solar Radiation Spectrum

Finally, it is important to note that conversion efficiency is dependent on the angle of incidence of the photonic energy. A PV cell exhibits its highest conversion efficiency when it is orthogonal to the incoming photons. As the angle of incidence is increased, the cell efficiency tapers off. The rate at which this occurs is dependent upon the design and construction of the cell.
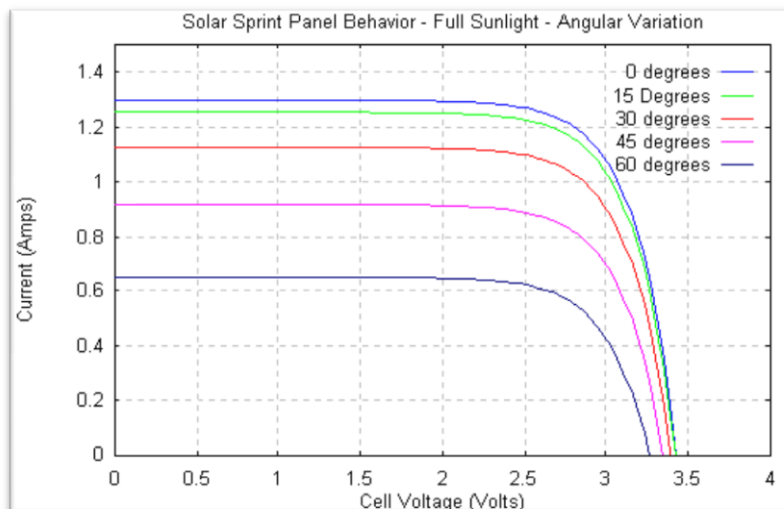
Figure 20: Solar Sprint Panel Incidence Variation

32

3.1.2 Vertical Multi-Junction Solar Cells

High voltage silicon vertical multi-junction (VMJ) solar cells have been developed by NASA-GRC scientists [29] that can provide efficient operation at solar intensities exceeding 2500 suns. These cells have a demonstrated performance of 40.4 watts per cm^2 output at 211 watts per cm^2 input with an estimated efficiency near 20 %. The remainder of the unconverted solar energy is given off into heat and/or reflected away. At these extremely high levels of solar flux, conventional planar solar cells would fail due to thermal degradation, while the VMJ cell is capable of efficient operation in this region. This makes the VMJ cell ideally suited for solar concentrator applications, where the performance advantage of the VMJ cell can lower the cost of the expensive semiconductor material required [30].

Figure 21: VMJ Cells in a 9 kW Solar Concentrator

The VMJ cell is an integrally bonded series-connected array of miniature silicon junction unit cells. The illuminated face of the cell is oriented at the side of the junctions, and so it is also referred to as an "edge illumination" multi-junction cell. Because of the series connected junctions, one small 40-junction VMJ cell (0.8 cm² area) can output a nominal 24 V under load. This eliminates the need to construct series stacks of photovoltaic cells in an array to interface with downstream electronics, resulting in a more compact receiver. The number of junctions in a VMJ cell can easily be varied during the manufacturing process to accommodate the bus voltage requirements of the end application.
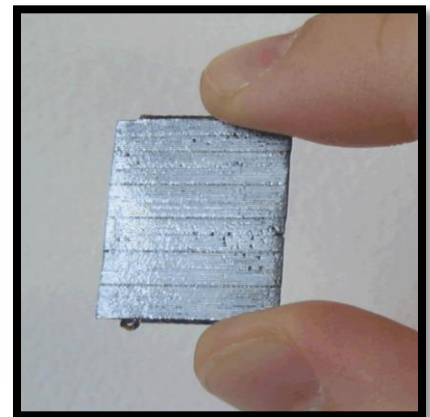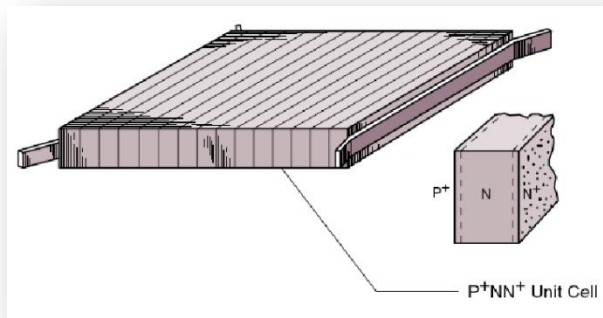
Figure 22: 40-junction VMJ Silicon Photovoltaic [29]

The unique design of the VMJ cell has several major inherent advantages. First, since the cell is edge illuminated, the need for electrical contacts on the illuminated face is eliminated. This allows for a greater convertible surface area for the photonic energy to enter the cell. Since the junctions are vertical, the cell thickness is not limited by the thickness of the silicon wafer, but can be adjusted during manufacturing to optimize

34

performance. Through the depth of each junction, there is an equal probability that an excess carrier can be generated from the impinging energy, increasing the chance for a photonic collision to occur. This produces an improved spectral response at low and high frequencies [31].
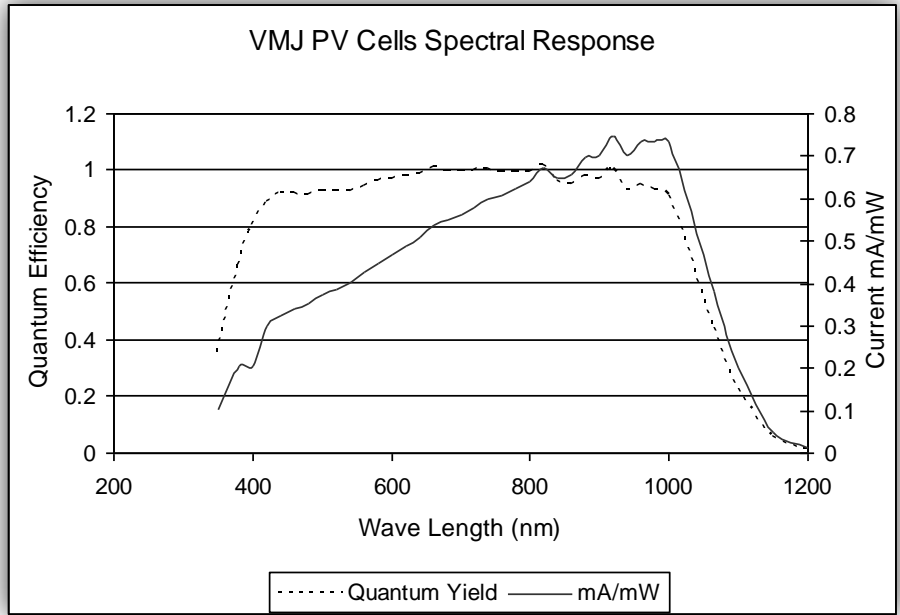
Figure 23: Spectral Response of the VMJ Cells

Second, the series connections of the junctions provide high compatibility with most loads. This also creates a very high reverse voltage breakdown immunity, which reduces the need for adding bypass protection diodes that are typical in paralleled photovoltaic arrays. In a reverse biased experiment, a 40-junction VMJ cell was able to withstand a 6 kV potential (the limit of the test equipment) with only minimal leakage current.
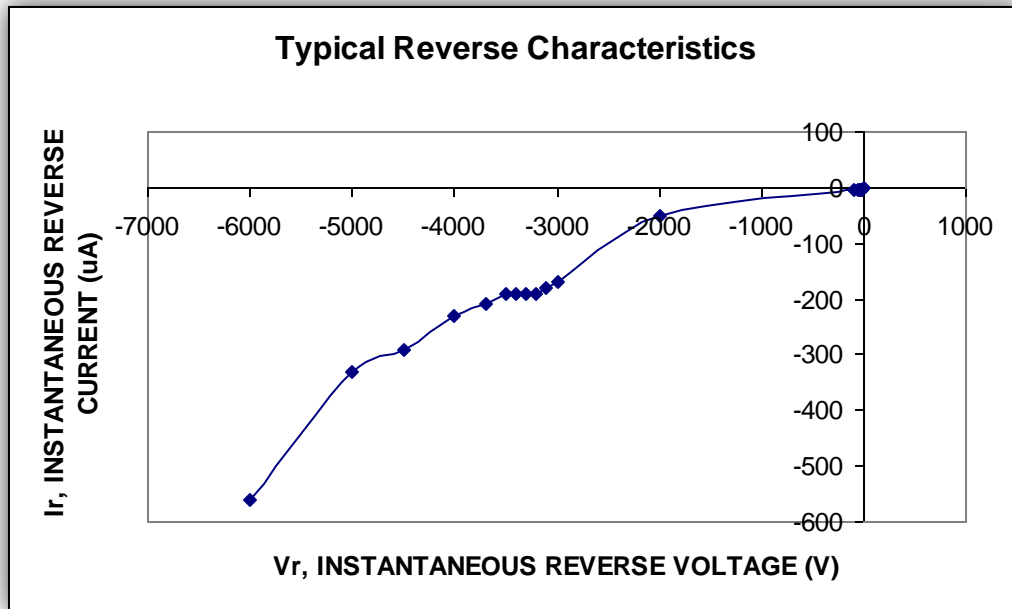
Figure 24: Reverse-Biased Test of a VMJ Cell

Most importantly, the design of the VMJ cell offers low resistance at high injection levels to decrease parasitic losses, and the edge contact interconnections allow for a higher packing density when compared with planar cells. This contributes to the VMJ cells ability to withstand high intensities while providing a low loss path for the generated electrons to flow.

The performance of the VMJ cells has been evaluated under steady state conditions in outdoor solar concentrators, as well as in NASA-GRC's Large Area Pulsed Solar Simulator (LAPSS). The characterization of a single 40-junction VMJ cell across a range of intensities can be seen in the results from the LAPSS test in Figure 25.

36
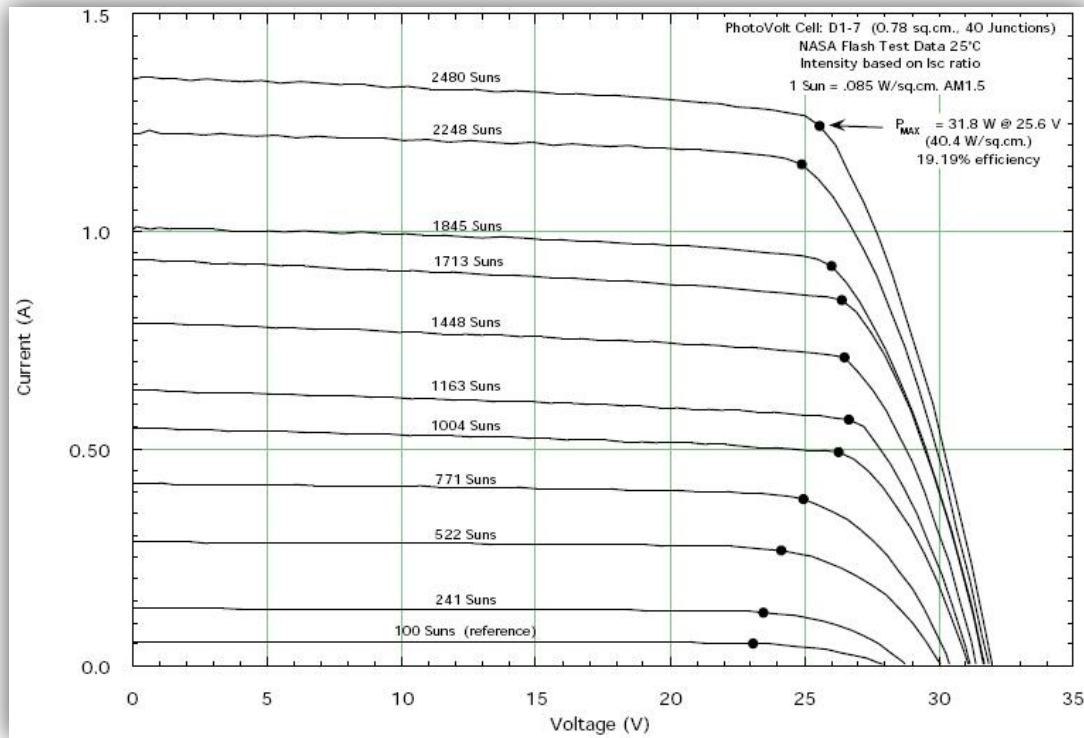
Figure 25: VMJ Cell I-V Curves from LAPSS

The nominal efficiency of the VMJ cells is at 25 ºC, above which the performance decreases steadily with increases in temperature. This is typical for all types of photovoltaic devices, and the rate of the performance degradation is dependent on the material and the construction of the particular device. Since the VMJ design does not require conduction wires which would mask large portions of the active photovoltaic area, the possibility for a freed electron to recombine with a hole in an electron-hole annihilation process is decreased. This contributes to the overall efficiency of the cell, and reduces the chance of runaway heat generation which may result in permanent damage.

There are many VMJ cells in operation with solar concentration units around the world, and the data collected from these units can be used to observe the efficiency losses due to thermal de-rating. Figure 26 shows the comparison of VMJ cells in a concentrator application when compared with triple-junction PV cells.
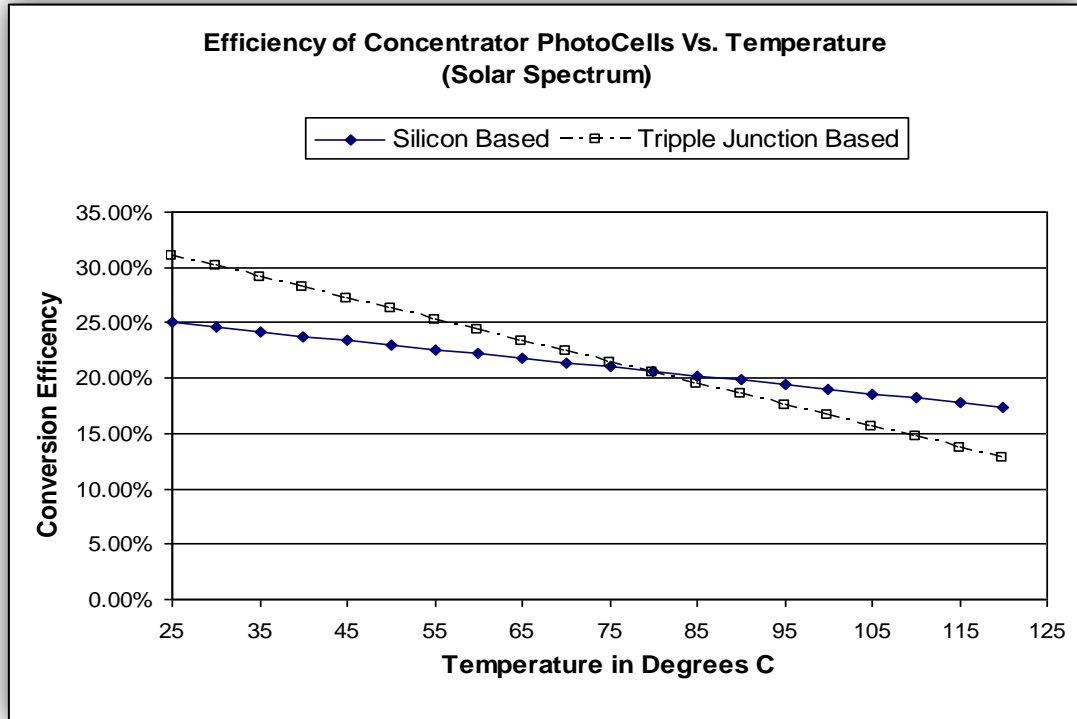
Figure 26: VMJ Cell Efficiency vs. Temperature

Since the VMJ cells are designed to operate under extremely high solar intensities, large amounts of heat will be absorbed and/or generated within the individual cells. As was previously discussed, the efficiency of solar cells degrades with increases in temperature. To obtain the maximum performance it is important that the temperature of the cells be maintained as low as possible. At high intensities this requires transferring substantial amounts of heat out of the cells and into a heat exchanger for rejection, except

in cases where operating at these reduced efficiencies is acceptable. A maximum limit must be avoided, above which catastrophic failures will occur from the delaminating of the junctions and the melting of the electrical contacts. The VMJ cells are very rugged however, and are able to withstand high temperatures up to 600 ºC.

3.1.3   Considerations with Laser Power Beaming

The demonstrated conversion efficiency of the VMJ cells is in the $20 - 25$ % range for full spectrum light, which is an average value across the frequencies of the solar spectrum. As indicated by the quantum efficiency peak in Figure 23, the conversion efficiency of the cell increases as the energy of the incident photons approaches the indirect band gap energy of silicon in the near-infrared region (around 1000 nm). The indirect band gap for silicon cells ranges from 1.125 - 1.2 eV depending on its crystalline structure. With incident laser energy in the 800 - 1000 nm range, the theoretical conversion efficiency of the cells will approach 50 - 60 %. It is also expected that the VMJ cells will maintain the same linearity for high laser power concentrations as was previously noted in the case of the solar spectrum in Figure 25.

A limiting factor in the performance of the VMJ cell under HILPB conditions is the energy profile of the incident light. Since the cell is made up of series junctions, it is ideal to have uniform illumination across the entire convertible surface. A single or group of weaker junctions (resulting from relatively less illumination) will limit the overall output from the cell. Since the cell is a series stack of many individual current

sources, the overall stack current will be limited by the weakest junction's contribution. The problem arises with HILPB, since the very nature of the propagation of a laser beam is not uniform, but fundamentally Transverse Electro-Magnetic Gaussian (TEM$_{00}$) in profile [32]. This is a primary issue that will be explored later in this paper.
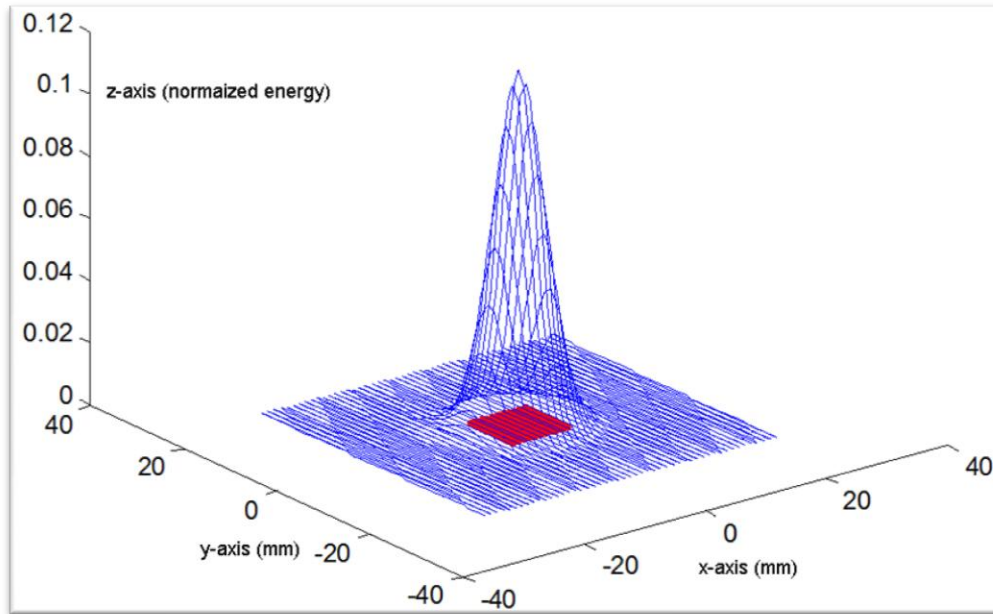
Figure 27: Gaussian Cell Illumination

The ability to exploit the dual use potential of the HILPB technology for both power transmission and communications is very substantial. Work has been done in determining the transient response of gallium arsenide and silicon solar cells using short laser pulses [33]. At laser intensities of 50 watts per cm^2 (500 suns), the GaAs cells exhibited a high frequency roll-off on the order of 1-2 GHz, and the Si cells exhibited a high frequency roll-off on the order of 5 MHz when subjected to a 840 nm and 1.06 micron, 25 nS pulse, respectively. These roll-offs set the initial bounds for practical communication bandwidth.

In the future implementation of HILPB, when the infrastructure is in the vicinity of life forms, the operational frequency of the laser can be shifted to an eye-safe region. High current density GaAs and GaSb photovoltaic materials have been developed for HILPB [34], and they are optimized for operation in the spectral range of 1300-1680 nm.

3.2   Lasers

3.2.1   State of the Art and Beyond

The recent decade has seen the rapid development of compact high energy solid state lasers, driven by the market need in the manufacturing sector for cutting and welding applications.   There is an ever increasing selection of COTS kilowatt range lasers, and the continual development and accessibility of these lasers will benefit the HILPB system.

When considering the feasibility of a HILPB system in a particular application, the end-to-end system efficiency must be considered in order to make a fair assessment. This includes the electrical to optical conversion efficiency of the laser source. Although there have been many recent advances in the field of solid state lasers contributing to compact packaging solutions, the average solid state laser efficiency is roughly 10%. In order for HILPB to become a viable option for practical wireless power transfer, each

efficiency component of the system must be improved to provide for a higher end-to-end system efficiency.

Fortunately, a new class of diode pumped alkali vapor lasers (DPALs) has been developed that can offer high electrical efficiencies of 25-30 % [35]. The DPALs are currently offered at wavelengths which couple well with the efficiencies of existing photovoltaic technologies: silicon at 895 nm (cesium), and GaAs at 795 nm (rubidium) and at 770 nm (potassium). These lasers will offer the ability to expand into the multi-kilowatt range through a single aperture by paralleling multiple laser modules. This would open up potential large-scale applications such as HILPB propulsion in order to raise satellites from LEO to GEO [36].

For the past few decades, much of the development of the High Energy Laser (HEL) has been directed towards weapons applications [37]. Much of this same technology is also directly applicable to power beaming. A typical HEL system consists of the laser device, beam control and acquisition tracking & pointing (ATP) systems.
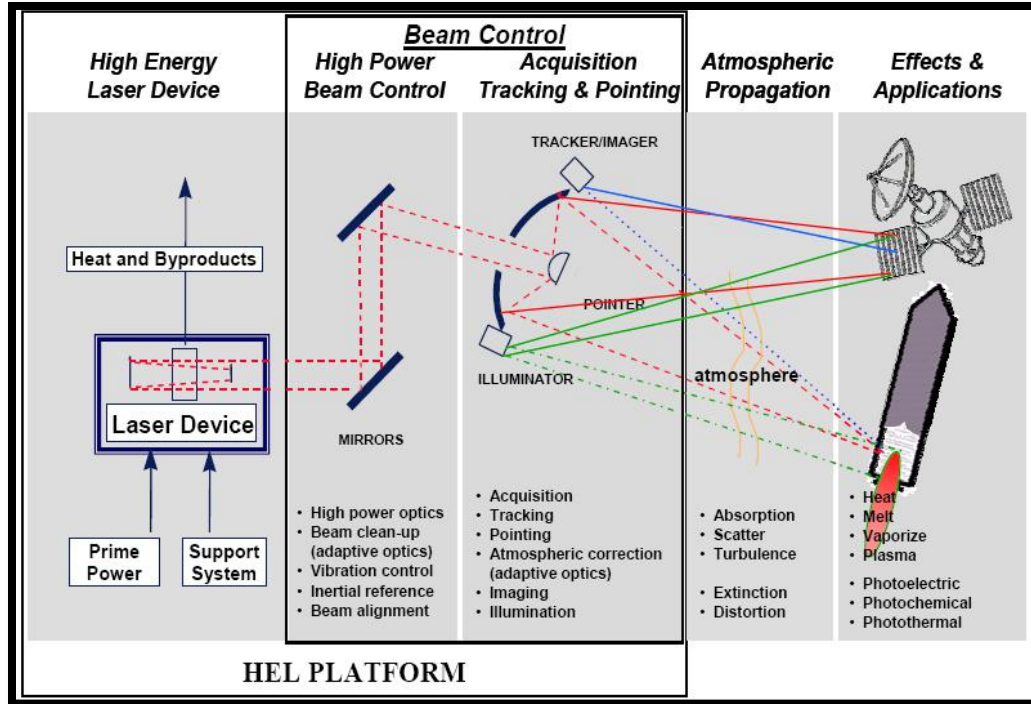
Figure 28: Elements of a HEL System [37]

In a typical HEL weapons application, the ATP sub-system is dealing with a hostile target, which may be an inbound ordinance. Technologies such as thermal imaging and pattern recognition may be employed to track the target. Techniques such as on-line sensing of the beam propagation through the atmosphere and adaptive optics have successfully been employed to insure the integrity of the beam propagation and to reduce jitter and compensate for air turbulence in the megawatt class Airborne Laser (ABL) research and development platform, whose ultimate mission is to destroy tactical ballistic missiles (TBMs) [38]. The 600 km destruction range of the ABL is a testament to the maturity of the current HEL technologies, and these military successes can be capitalized on with laser power beaming. The high-profile ABL program is an ongoing effort, and

43

new advances in laser control will be continually developed to increase the range and accuracy of the beam [39].

Figure 29: Boeing ABL with Laser Turret [38]

In a power beaming application, since the target is the power receiver, telemetry can be employed to augment the amount of information available to the ATP sub-system, thereby increasing the performance of the system.

Weapons applications for lasers have been an active pursuit since the early stages of their development. The ability to project a large amount of power onto a distant, small area makes them inherently suited for this task. Also proposed early on was an application of a high-powered laser for the civilian space program [40]. This proposal by Kantrowitz in 1972 investigated the feasibility of an earth-to-orbit launch system, in which a ground based laser provides thermal energy to a rocket propellant (such as

hydrogen), for the purpose of reducing the lift-off weight of the vehicle by eliminating the oxidizer. The technological problems unique to such a laser and the cost aspects of the system were considered. This set the stage for many similar proposals on laser power and propulsion during the 1970s. These activities identified several major themes concerning laser power transmission for space applications, and revealed that advanced space missions requiring expensive transportation applications showed a high potential for cost reduction through the use of remote laser power [41]. A comparative analysis by Holloway and Garrett [42] showed a substantial payoff for remote power beaming to orbital transfer vehicles, and particularly those employing a direct nuclear or solar pumped laser source. A preliminary analysis between such a system and a comparable 1 megawatt planar solar photovoltaic system reveals that the laser receivers were lighter and smaller than the conventional photovoltaic panels, resulting in less drag at lower altitudes and allowing for fewer Shuttle trips for construction [43].

From these studies in the 1970's, a general set of requirements began to emerge for laser power beaming in space. The remote deployment of the system demands that the laser be capable of long-term operation without significant maintenance, which suggests either solar or nuclear powered lasers. Also, since the largest payoff is in high-power applications, the laser must be capable of supplying a high amount of average power, on the order of 100 kW or greater. This requirement suggests the use of either continuous wave or rapidly pulsed lasers. Three general laser mechanisms have been identified to meet these reliability and power requirements: photodissociation lasing

driven directly by sunlight, photoexcitation lasing driven directly by sunlight and photoexcitation lasing driven by thermal radiation.

Several types of organic iodide lasants based on photodissociation have been identified and successfully solar-pumped, resulting in an emitted wavelength of 1.3 micrometers. Several reports on modeling and experimental results with IBr and C_3F_7I lasants have been published [44, 45, 46, 47 and 48], and have found that the lasant does not require resupply (unlike most chemical lasers) since the lasant molecules tend to spontaneously recombine, and that the laser remains cool enough to eliminate a thermal radiator since these lasants absorb almost no visible light. Techniques for further enhancing the recombination of the photodissociation products are being investigated, as this will contribute to an increase in laser efficiency.
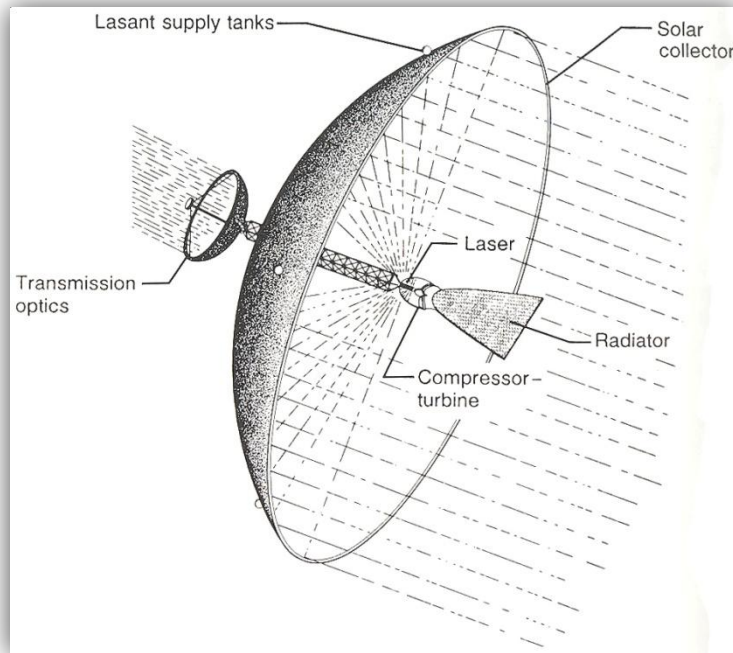
Figure 30: One-Megawatt Iodine Solar-Pumped Laser [41]

The group of direct solar-pumped photoexcitation lasers relies on the electronic-vibration excitations produced by the sunlight to power the laser action. One such system being studied is a liquid neodymium (Nd) ion laser, which emits in the near-infrared region at 1.06 um. Another system is the dye laser, which absorbs in the blue-green range and emits in the red region near 0.6 um. Although these types of lasers offer good quantum efficiency and a relatively short wavelength, they require extremely high excitation to overcome their high threshold for lasing, and are still being researched as to their feasibility.

The group of indirect photoexcitation lasers driven by thermal radiation typically has a longer wavelength emission. A blackbody-cavity-pumped laser [49] and a blackbody-pumped transfer laser [50] operate on the principle of passing preheated molecules such as CO_2 and N_2O through a laser nozzle and/or cavity. Although they offer great potential for converting solar thermal energy to laser energy in space, they can also convert thermal energy generated by chemical reactions, nuclear power, electrical power or other high temperature sources.

Although the laser power requirements for space applications are very different from those of the military, the basic research conducted by these other agencies is applicable. Future space transportation applications show a high potential for cost reduction using laser power beaming, and this is driving the research toward higher laser conversion efficiencies. The development of laser power transmission in space is a revolutionary technology that will enable exploration missions that were previously not possible.
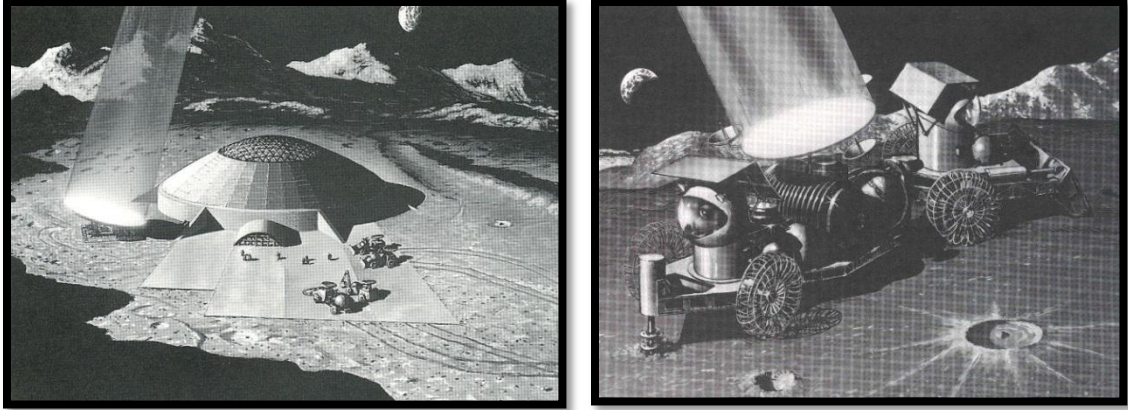
Figure 31: Laser Power to a Lunar Base and Vehicle [41]

3.2.2 Atmospheric Considerations

The atmosphere has a wide region where it is least susceptible to ionization (least absorbance) by the longest wavelengths of the light spectrum, as described by Beer-Lambert's Law. For this reason, a laser in the infra-red (IR) region (the region of interest for this HILPB system) would be optimal for long distance power beaming within the atmosphere.
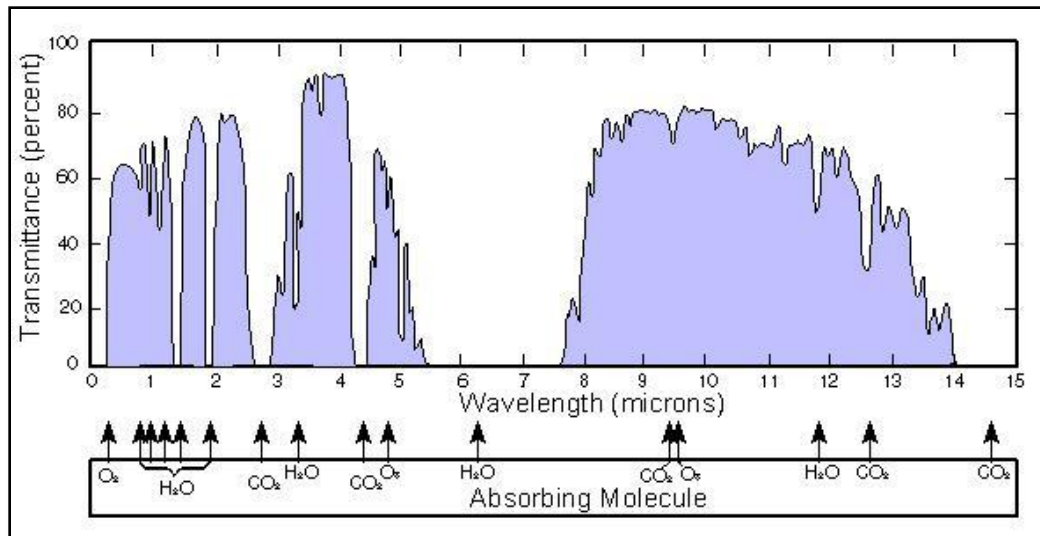
Figure 32: Atmospheric Optical Window - *Wikipedia*

Safety is a major consideration in the design and implementation of a HILPB system. Spurred by the recent developments in weapons-grade ultra-high power pulsed lasers, beam conditioning and control optics have also been developed. Information regarding the manipulation and transmission of high powered lasers is generally classified due to the nature of their application. It is widely known however, that successful high power laser systems are currently operational, and it follows that the conditioning and control optics are in place to handle such a system [51]. For many of the laser weapons systems, a secondary laser is used to test the integrity of the primary beam between pulses. Many of these systems also rely on optical recognition to track their targets. This technology could be easily adapted to suit the needs of the laser power beaming application.

The condition of the atmospheric medium must be considered as an operational issue for the optimum and safe transmission of power. Various circumstances will have

an influence on the nature of the optical propagation. Moisture in the form of rain droplets will cause a minimal amount of Raleigh and Mie Scattering, as well as absorption of the laser energy as seen in Figure 33. Fog will have a much larger attenuation effect, since the aerosol particles are closer in size to the wavelength of the laser. A denser fog will cause an increase in the scattering and absorption of the laser energy. Scintillation will also result from the small-scale fluctuations in the index of refraction of the atmosphere, as depicted by the energy fluctuations at the right edge of Figure 33. This will cause small variations in the temperature of the atmosphere, leading to inconsistencies within the laser beam. As the result, the system will be able to function predictably during rainstorms, but will change its operating characteristics during periods of heavy fog.
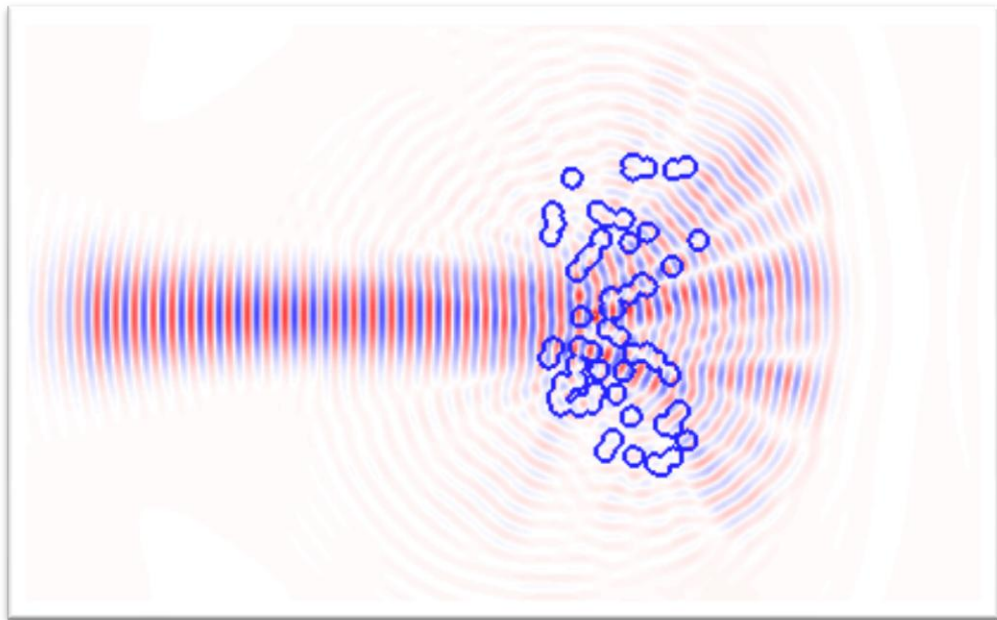
Figure 33: Mie Scattering, Scintillation and Absorption

Larger airborne solids, such as particles of sand, will have a dramatic attenuation effect on the laser energy. To a lesser degree, atmospheric turbulence will also disrupt the integrity of the beam. Natural events such as sandstorms would hinder the proper operation of the system.

CHAPTER IV

EXPERIMENTAL SETUP

As previously discussed, the HILPB receiver is the part of the system which converts the optical energy to electrical energy (desirable) and dissipates the (undesirable) thermal energy. This conversion is accomplished through the vertical multi-junction (VMJ) cells originally developed by scientists at NASA-GRC and currently supplied by Photovolt.

Support to develop this system was provided by the Air Force Research Laboratory (AFRL) Munitions Directorate at Eglin Air Force Base in Florida. The tests were conducted at Northrop Grumman Space Technology (NGST) Park in Los Angeles, California and at Lissotschenko Mikrooptik GmbH (LIMO) Laser Applications Laboratory in Dortmund, Germany. The large distance from these locations to the Industrial Space Systems Laboratory (ISSL) in Cleveland, Ohio facilitated the need to develop portable hardware to conduct the experiments.

The receiver was designed to maximize the conversion potential of the VMJ cells for laser applications, by tailoring the geometry of the receiver to the beam and by providing sufficient cooling and electrical connections. These prototype receivers are supported by data collection electronics, which were developed specifically for this application to automatically track the voltages, currents and temperatures during the experiments.

4.1   HILPB Receiver Design and Construction

The design and construction of the HILPB receiver addresses four main issues. First, the receiver needs to provide sufficient thermal dissipation in order to handle the excess unconverted energy. Second, the materials in the power receiver must have similar coefficients of thermal expansion to avoid stress fracturing during thermal cycling. Third, the electrical paths and connections in the receiver must be of low resistance in order to minimize electrical losses. Lastly, the receiver must provide electrical isolation for the junctions in the VMJ cells as well as for the electrical routing and connections.

A standard COTS heat-sink was selected and modified for the receiver to permit rapid prototyping of the design. Figure 34 shows the Zalman unit, which is typically used to dissipate approximately 100 watts of thermal energy while maintaining a 60 ℃ temperature for a computer processor inside of a forced-air enclosure. The initial phase

of laser testing was to be at 100-200 watt intensities, and so the expected operating temperature of 60 ºC by the Zalman unit made it an appropriate choice. The unit is constructed from plated copper to resist tarnishing, and features three heat pipe re-circulators that are partially filled with a phase transition fluid [52]. The heat pipes traverse through a radial array of fins, where airflow is induced by a small fan. For the HILPB application the fan has been replaced by a more powerful motor and propeller arrangement supplied by the AFRL, in order to increase the cooling capacity beyond the manufacturer's specifications. The front mating surface of the heat-sink is polished to provide maximum contact area to aid in heat transfer, and it is upon this surface that the power receiver is constructed.

Figure 34: Zalman 9500 Heat-sink

A cross-sectional illustration of the receiver design is shown in Figure 35. The VMJ cell is mounted on a substrate using boron nitride filled epoxy resin [53]. This resin has good thermal conductivity (1.5 watts per meter ºK), and a relatively high maximum operating temperature (approximately 200 ºC) which is sufficiently far away from the

normal operating range of the receiver. In the center of the stack-up is the polished

aluminum nitride substrate [54]. Aluminum nitride has very good thermal performance

characteristics (175 watts per meter °K) and low thermal expansion (4.6E-6 from 20-400

°C) to match the silicon VMJ cells, and good dielectric strength (10E14 ohm-cm) to

provide electrical insulation. It is commonly used as a substitute for the standard FR4

fiberglass in printed circuit board (PCB) construction for better thermal conductivity.

These characteristics make it ideal for the HILPB receiver application. The substrate is

mounted to the heat-sink using another layer of the boron nitride epoxy resin.
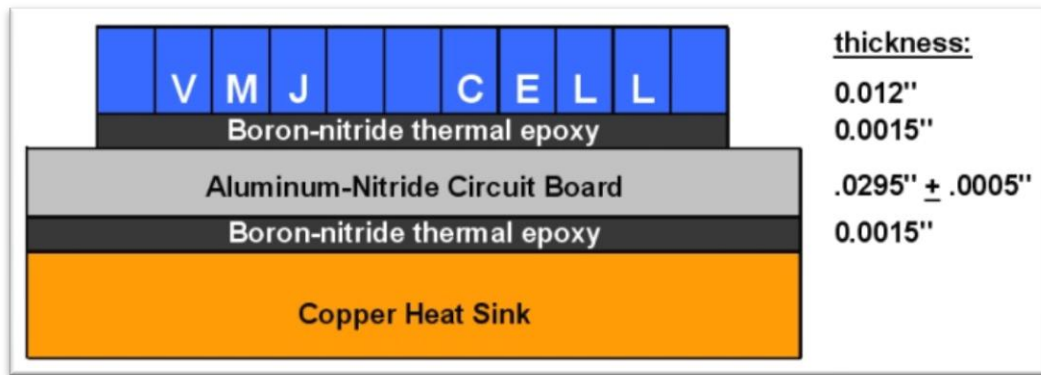
Figure 35: Receiver Cross-Sectional Stack-up

The electrical paths were routed using a ferrite-nickel-cobalt alloy wire known as

Kovar™ [55]. Kovar™ is a material commonly used for bond wires within

semiconductor construction, since its coefficient of thermal expansion (3.3E-6 from 20-

100 °C) is similar to that of silicon, which makes it an appropriate material to use with the

VMJ cells. 6 % silver plating was applied to the Kovar™ wire, resulting in a low

electrical resistance of 31.9 Ω per 1000 ft. The routing wires are attached to the outer

two junctions of the VMJ cell with an electrically conductive silver-filled adhesive paste

[56]. The paste has a high melting temperature (962 ℃) and a low electrical resistivity (3.0E-5 Ω-cm).

Basic thermal analysis was performed to determine the approximate maximum theoretical temperature of the receiver during HILPB operation. This was accomplished by considering the thermal conductivity and the dimensions, then calculating the thermal resistance for each material in the stack. For the purpose of this calculation the complete receiver is interpreted as a bulk resistance, and so the tabulated values are combined with the ambient temperature and the optical input power to determine the average steady-state temperature of the receiver [57].

TABLE I: THERMAL ANALYSIS OF THE LASER POWER BEAMING RECEIVER

Material (stack top-to-bottom)	Thermal Resistance $\Theta i = (\Delta ℃ / W)$
VMJ Cells	$\Theta 1 = 0.02$
Boron-Nitride Epoxy	$\Theta 2 = 0.1905$
Aluminum-Nitride Substrate	$\Theta 3 = 0.0027$
Boron-Nitride Epoxy	$\Theta 4 = 0.0119$
Heat Sink (stock fan at 2,600 RPM)	$\Theta 5 = 0.12$
Heat Sink (stock fan at 1,350 RPM)	$\Theta 5 = 0.16$
Surface Temperature Equals: Ambient Temp + Input Power * ($\Theta 1 + \Theta 2 + \Theta 3 + \Theta 4 + \Theta 5$)	

With an ambient temperature of 20 ℃, the manufacture's cooling fan running at 2,600 RPM, 30 % conversion efficiency for the VMJ cells and an input power of 130 optical watts, Table 1 yields an average theoretical receiver temperature of 51.4 ℃. With an input power equal to a value of 220 optical watts, the average theoretical receiver temperature is 73.15 ℃. Although in practice there will be a temperature delta at each of the junctions, as well as a gradient across each of the materials, the calculated results give

56

a good indication as to the expected performance of the receiver. By upgrading the stock fan, these temperatures can be decreased, thus increasing the upper limit of the maximum thermal load the system can dissipate.

The published airflow data for the original cooling fan are 20.6 cubic feet per minute (CFM) at 1,350 revolutions per minute (RPM) and 36.5 CFM at 2,600 RPM. In replacing the original cooling fan with a new motor and propeller, a rough estimate was made to determine an approximate operating speed needed to achieve the original airflow specification. The new motor has a 1 inch diameter hub, and an 8 inch diameter propeller with two blades at a 4.3 inch pitch. These dimensions are used to calculate the amount of air displaced from the new propeller advancing by one revolution, as illustrated in Figure 36.
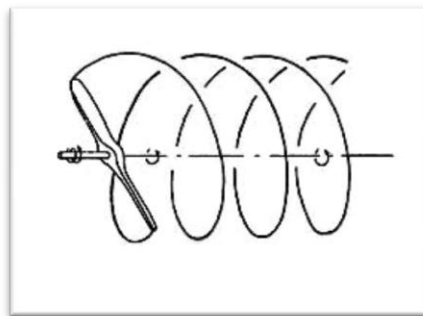

Figure 36: Propeller Path Representing Displacement

The volume of air displaced by one revolution of the propeller is determined by calculating the volume of air created from one revolution of the advancing propeller, and subtracting the volume occupied by the center hub, as shown in the following calculations. A bulk aerodynamic efficiency of 60 % is selected to account for the

slippage of the propeller, the compression of the air, the efficiency of the airfoil and the use of a two blade propeller:

$$Displacement_{prop} \ = \ \pi \times radius_{prop}{}^2 \times pitch \qquad\qquad (4.1)$$

$$Displacement_{prop} \ = 0.125\ feet^3 \qquad\qquad (4.2)$$

$$Displacement_{hub} \ = \ \pi \times radius_{hub}{}^2 \times pitch \qquad\qquad (4.3)$$

$$Displacement_{hub} \ = 0.00195\ feet^3 \qquad\qquad (4.4)$$

$$Displacement_{total} \ = \ 0.6 \times \left(Disp_{prop} - Disp_{hub}\right) \qquad\qquad (4.5)$$

$$Displacement_{total} \ = \ 0.074\ feet^3 \qquad\qquad (4.6)$$

In order to match the original 36.5 CFM of airflow, the new motor must turn at the following speed:

$$speed = \frac{airflow\ _{desired}}{Displacement\ _{total}} \qquad\qquad (4.7)$$

$$speed = 494.4\ RPM \qquad\qquad (4.8)$$

The new propeller allows the new motor to turn at a much slower rate than with the original fan. At higher speeds the new propeller provides cooling capability to the heat sink well beyond the manufacture's original design, which will allow for higher power tests to be conducted.

The temperatures at various points in the receiver are monitored by five type-K thermocouples. Two miniature 0.020 inch square channels have been machined into the front face of the heat-sink, as illustrated by the cross pattern in Figure 37. Four transition

junction thermocouple probes are embedded into these channels with the boron-nitride epoxy, thereby residing between the face of the copper heat-sink and the aluminum-nitride substrate. Each thermocouple probe extends toward the center of the face by a different distance in order to depict the temperature profile across the face of the heat-sink. The fifth thermocouple is mounted on the top surface of the aluminum-nitride substrate next to the VMJ cell, in order to monitor the temperature difference between the surface and the center of the receiver directly underneath the VMJ cell array.
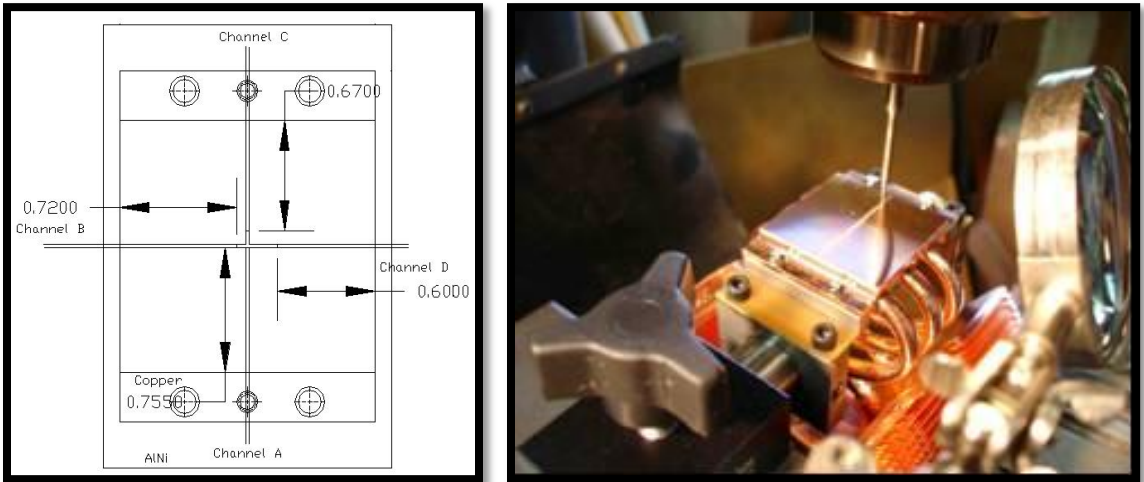
Figure 37: Probe Channels Machined into the Face

The electrical routing and connections are physically supported by GPO-3 high temperature electrical grade glass polyester laminate material. This material can withstand 120 ºC, and provides a rigid insulating surface for the electrical connection points. Aluminum mounting brackets were designed and machined to bolt the remaining structural components of the receiver together, and to serve as a mounting point for the clamps used on the optical bench.

The mounting and routing arrangement for a completed four cell receiver is shown in Figure 38. On this particular receiver, the wiring allows each cell to either be used individually or together in a parallel configuration. Single, double, nine and eleven cell arrays have also been designed and constructed to accommodate a variety of experiments to be covered in the next chapter.

Figure 38: Instrumented Four Cell HILPB Receiver

In order to obtain some preliminary data points, and to empirically verify the thermal dissipation capabilities of the HILPB receivers, a solar concentration apparatus was designed and constructed from steel and stainless tubing (Figure 39). A 30 inch by 40 inch acrylic Fresnel lens was selected to focus the solar energy down to the size of the
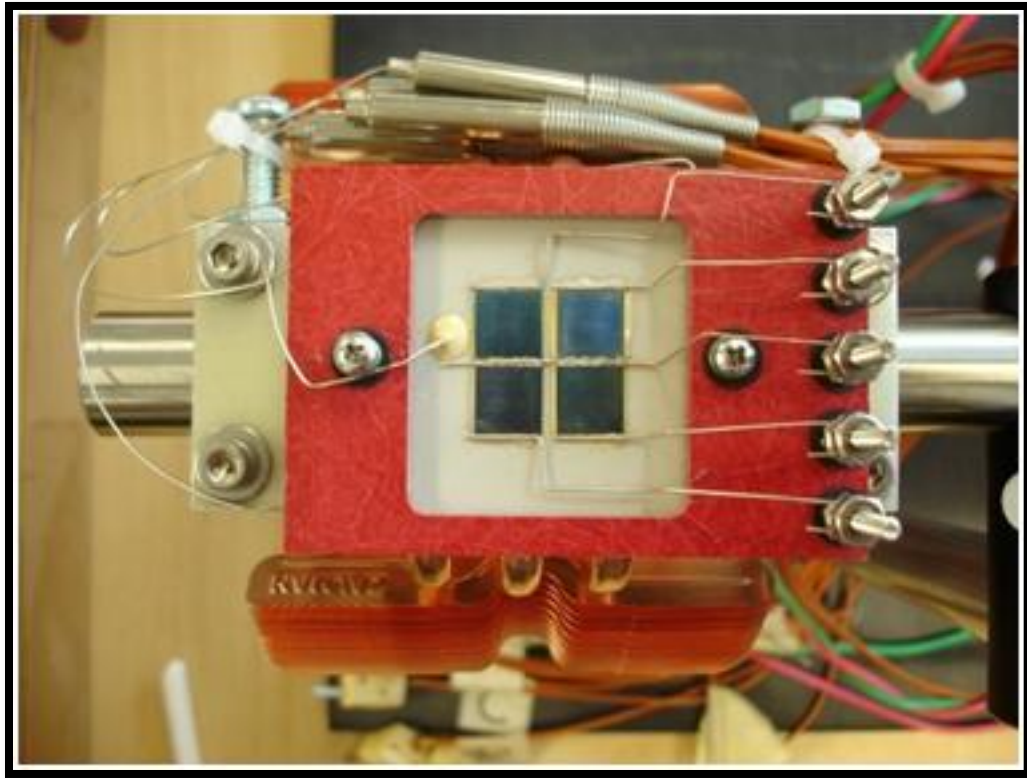
receiver. Various apertures were used to regulate the amount of light entering the lens, thus providing a way to control the energy being delivered to the receiver. The concentrator is manipulated with a pivoting indexer, so it can be manually adjusted to follow the arc of the sun moving across the sky. The receiver is mounted at the focal point of the lens, and is electrically connected to multi-meters and a variable load. Provisions were made to record the thermal, electrical and optical data during the experiments.

Figure 39: HILPB Receiver in the Solar Concentrator

Translational and rotational micro-positioning stages were assembled together to provide positional control of the receiver beneath the Fresnel lens. The stages allow for six degrees of freedom to enable alignment with the focal point.

During the day of the experiment the solar energy reaching the lens was measured to be 800 watts per meter^2. A mask was used to limit the input to a circular area with a radius of 25.4 cm. The lens transmission efficiency was 90 % and the focusing efficiency was approximately 80 % (due to the difficulty in obtaining precise optical alignment)

[58]. The total resulting solar energy illuminated the receiver was approximately 116 watts. This energy was extremely Gaussian due to the concentration stage [59], which for these purposes approximates the profile of a laser beam.

Figure 40 shows the temperature trend from the embedded thermocouples while the test was conducted. At the start and near 1200 seconds the propeller was turned off, as illustrated by the peaks nearing 50-60 ºC in the graph. The steady-state temperature resides at 40 ºC. The results of the experiment surpass the theoretical predictions, and this confirms the thermal dissipation capabilities of the receiver.
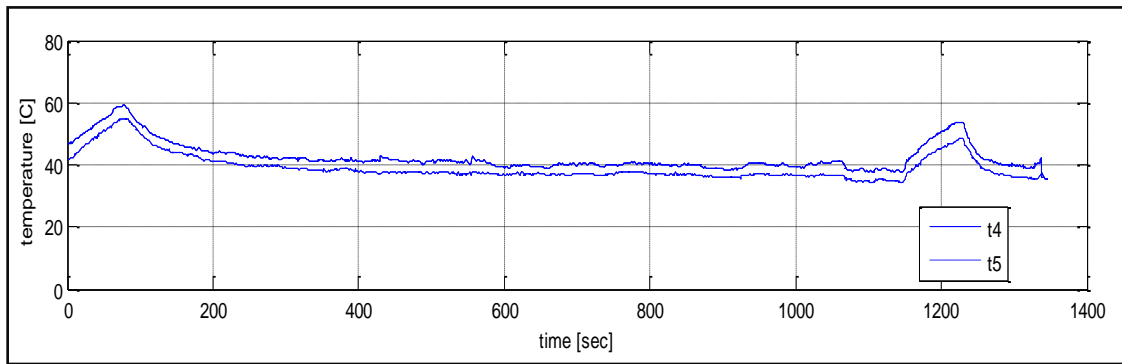
Figure 40: Thermal Validation of the Receiver

Although the primary purpose of this experiment was to evaluate the thermal management of the receiver, electrical data was also recorded during the experiment to verify that it was operational following its construction. This data is shown in Figure 41. Of the total solar energy, approximately 23 watts were illuminating the VMJ cells. The sensitive optical alignment issues and the cosine losses from the Fresnel lens limited the peak output power of the VMJ cells to approximately 3 watts, for a conversion efficiency of approximately 13 %.

62
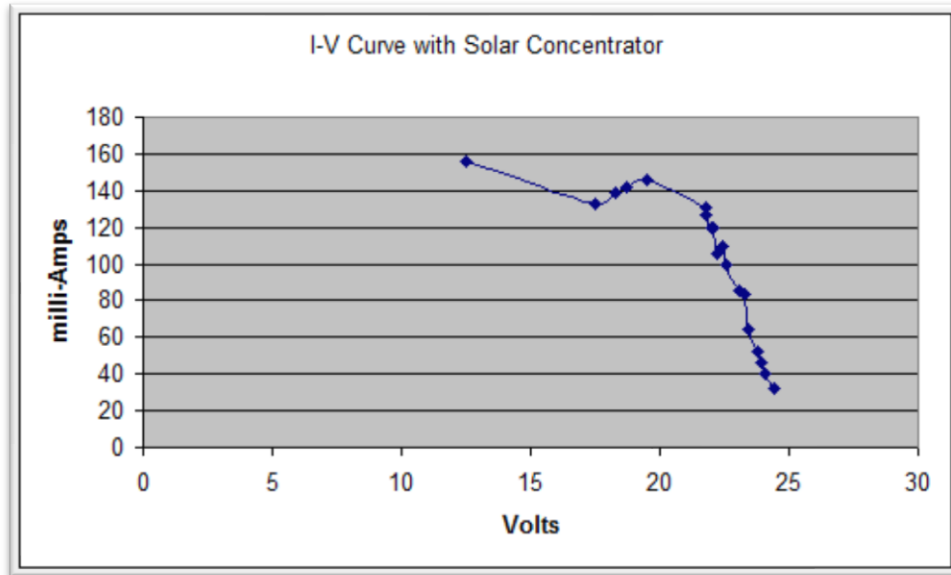
Figure 41: Electrical Validation of the Receiver

4.2   Data Acquisition

In order to characterize the performance of the receiver, a variable load may be used in conjunction with a current meter and a volt meter, as illustrated in Figure 42. By varying the value of the load from open-circuit to short-circuit for a given optical input and recording the data, an I-V curve for the receiver may be constructed.

Figure 42: Schematic for Characterizing the Receivers

63

This characterization process was automated by developing a data acquisition (DATAQ) system that records the voltage, current, and temperature information across multiple channels. The system is comprised of three subsystems: an active variable load, the sensing circuitry, and the data logging and processing. Care was taken in the design of the buffering, gain and sampling circuitry to provide the cleanest possible analog signals with highly accurate digital representations. For exam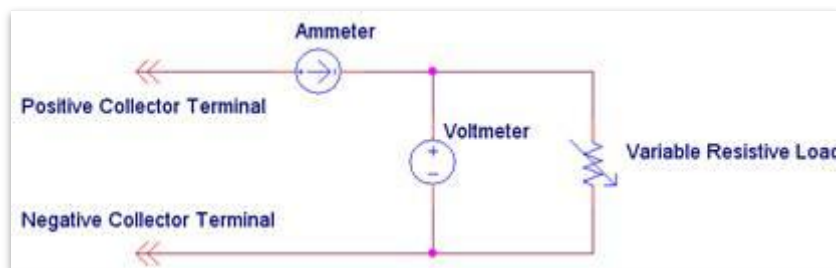ple, the current sensors employ an open-loop/Hall Effect configuration, thus minimizing noise interference and current draw. Also, in terms of accuracy, the data is represented by 16-bit words, and these values are sent to the computer at an update rate across all channels at 6 Hz. There is extra filtering in the power conversion circuitry to minimize ripple. The functional block diagram of the DATAQ system is illustrated in Figure 43.
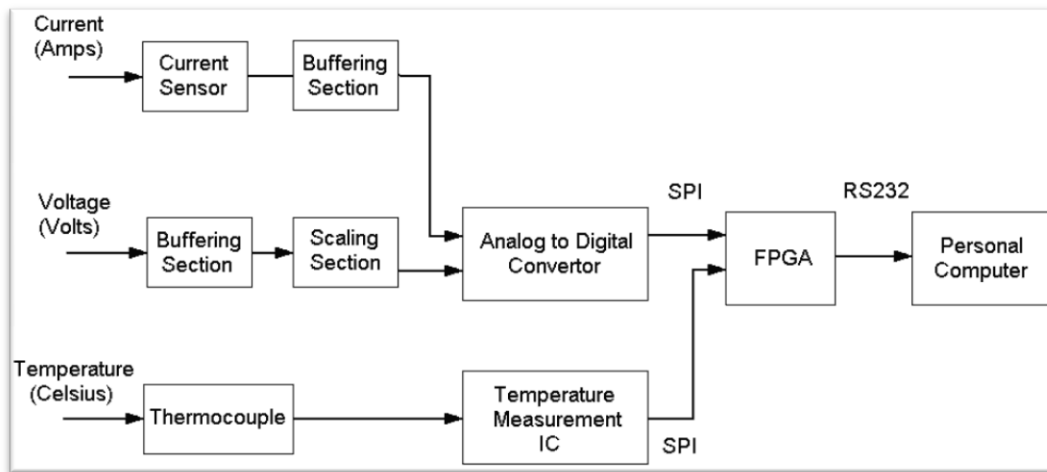

Figure 43: DATAQ Functional Block Diagram

For reliability and modularity, the DATAQ system is divided into two PCBs, as shown in Figure 44. The Xilinx Spartan-3 development board serves as the mother board, where a 200k gate field programmable gate array (FPGA) is utilized for

processing and sending the data to a personal computer through a RS-232 interface for logging and analysis. The power, channel sensing and analog to digital conversion circuitry has been integrated together within a separate daughter board, which interfaces to the main development board through multiple headers. This board was carefully designed to provide separation between the analog and digital signals and power planes to provide for noise immunity.
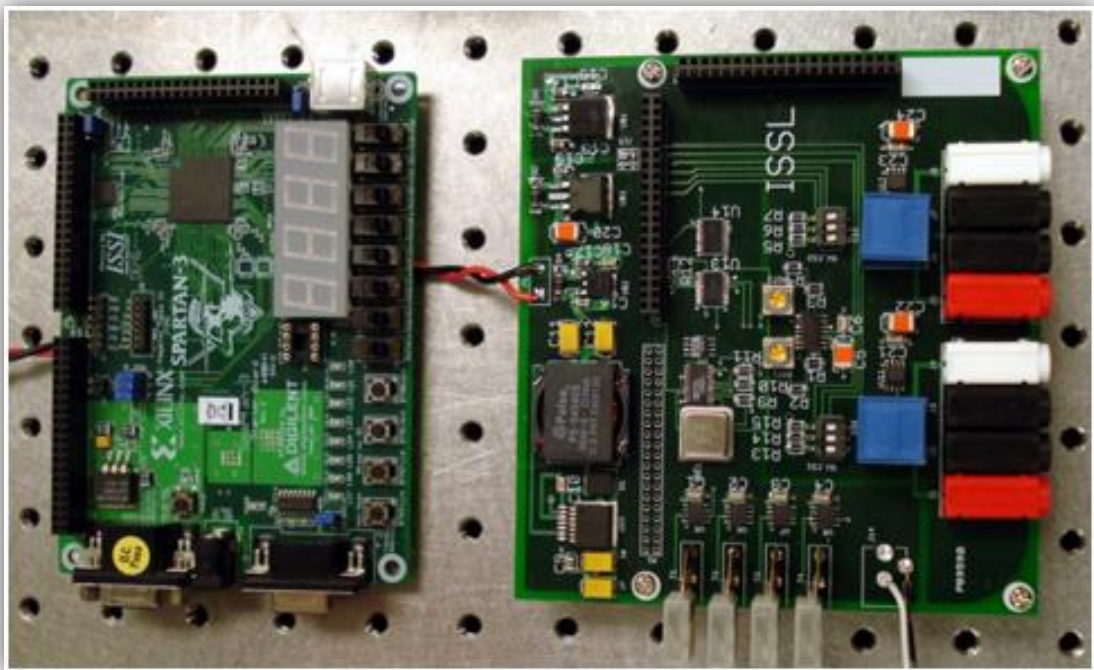
Figure 44: DATAQ Hardware

After the data from the electronics is sent to the computer, it is displayed on a Graphical User Interface (GUI) (Figure 45). The real-time plotting of the I-V data, and the continuous recalculation of the power output during the experiments allow for an

efficient use of the time in the laser laboratory, by automating the data collection process as much as possible.
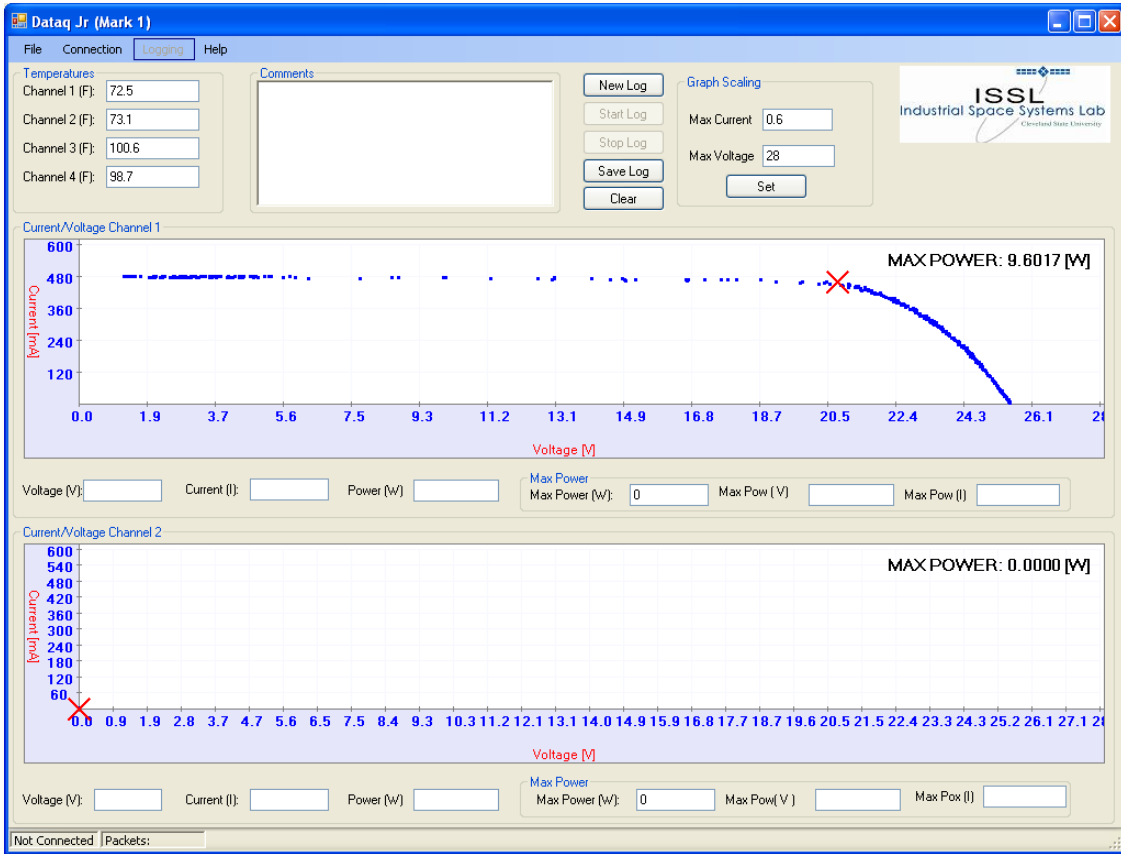
Figure 45: DATAQ GUI Plotting a Typical I-V Curve

4.3   Lasers and Optics

There were a total of four different continuous-wave fiber-coupled lasers available to conduct the experiments. Three of the lasers were 70 watt capacity units with 200 um diameter fibers, and had wavelengths of 808 nm, 940 nm and 976 nm

(LIMO70-F200-DL808, LIMO70-F200-DL940, LIMO70-F200-DL976). These three lasers were used for determining the best wavelength for receiver efficiency. The fourth laser was a 200 watt capacity 980 nm unit (HLU200-F400-980P2-M2), and this was used for all of the high power tests.

The lasers are complete systems including the power, control, water chiller and diode module. They are controlled by limiting the current delivered by the power supply, to regulate the amount of generated optical energy. A calibration curve describes the relationship between electrical input and optical output of the laser, and this is verified regularly with a power meter.

Figure 46: LIMO Turnkey Laser System

The wavelength of the laser deviates slightly, as can be seen in Figure 47. Here a 980 nm laser is measured to be operating at 977.2 nm, with a spectral bandwidth of 2.9 nm. For the purposes of HILPB, these variances are negligible.
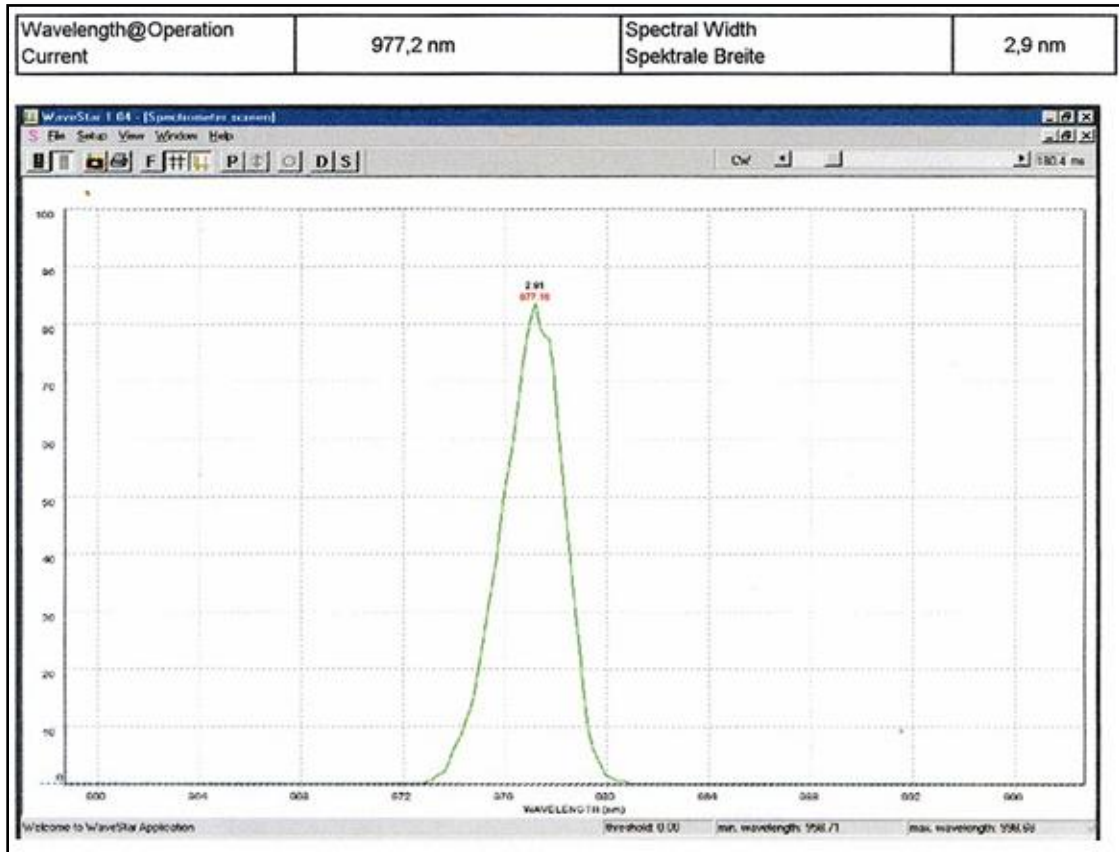
Figure 47: LIMO Laser Spectral Measurement

As was previously discussed, the energy profile across laser beam is Gaussian in nature. This can be measured and imaged, as shown in Figure 48. The graph shows the very tip of the Gaussian distribution, and the picture show the entire profile, as captured by a thermal imaging camera.
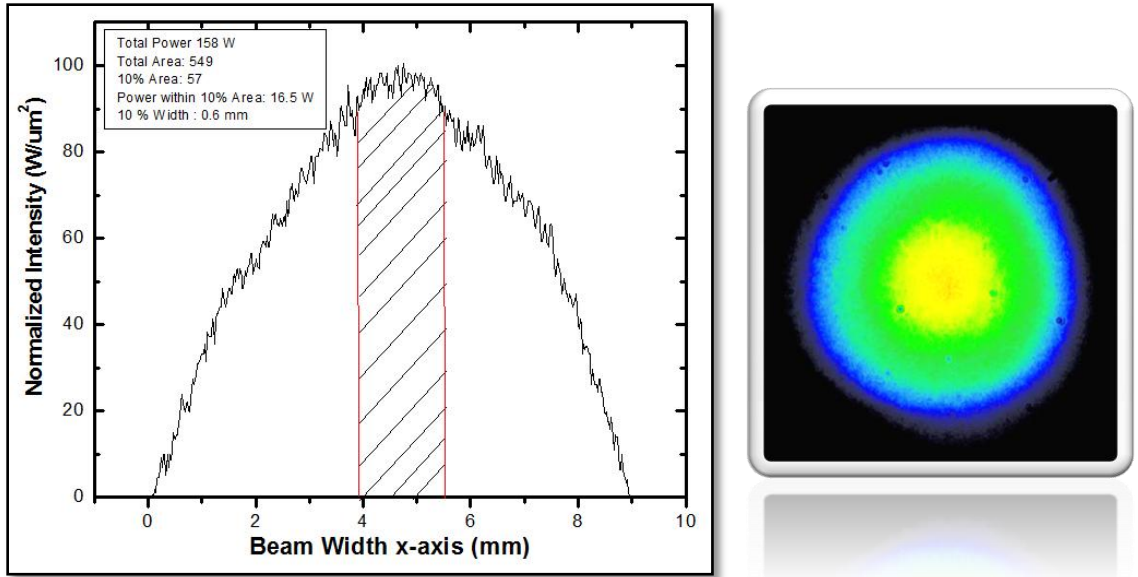
Figure 48: LIMO Laser Energy Profile Measurements

In order to protect the end of the optical fiber from dust and disturbance, a shroud was placed over it with an optical window. This is a common practice for laser welding applications in dirty environments, and it increases the life expectancy of the fiber. The window is a Melles Griot part 02WBK044 with anti-reflective (AR) coating /077. There is a minor efficiency loss in using the optical window, and this is taken into account in the analysis of the results.
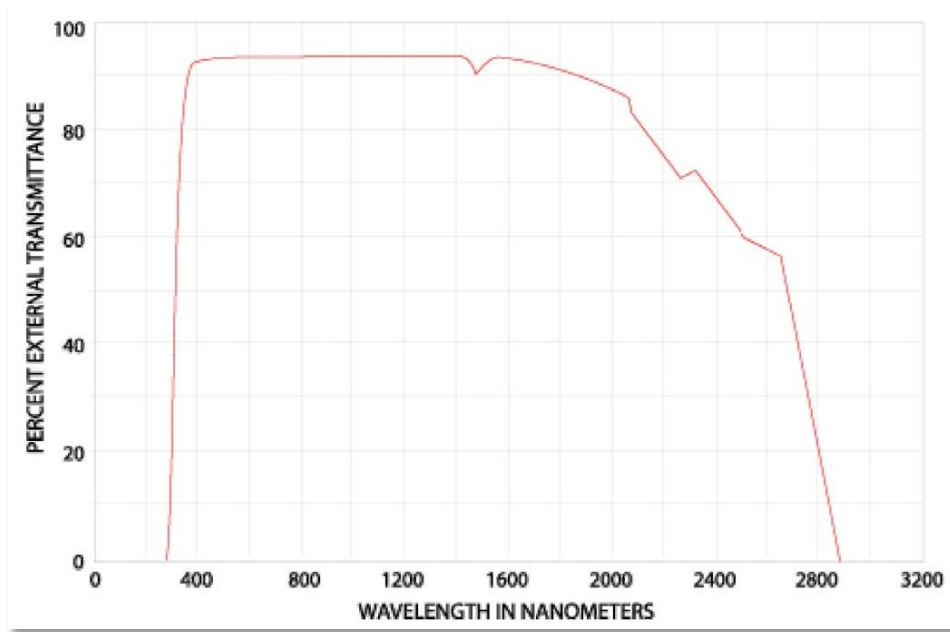
Figure 49: Melles Griot Transmittance Curve
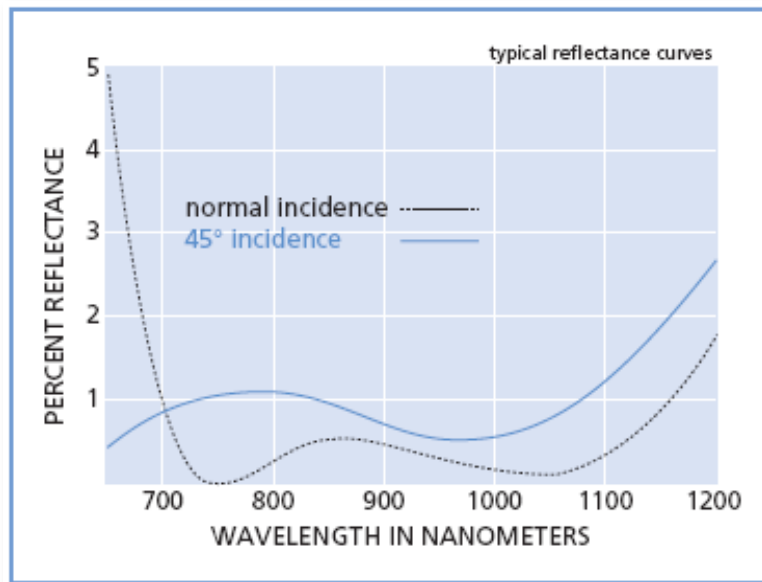
Figure 50: HEBBAR Coating for Near-Infrared /077

In order to observe the effects of the Gaussian laser beam versus a flat profile on

the performance of the VMJ cells, a LIMO flat-top optics stage was used to condition the

beam. This optics stage can provide for a profile variation within 1 % at efficiencies of
around 80 %.
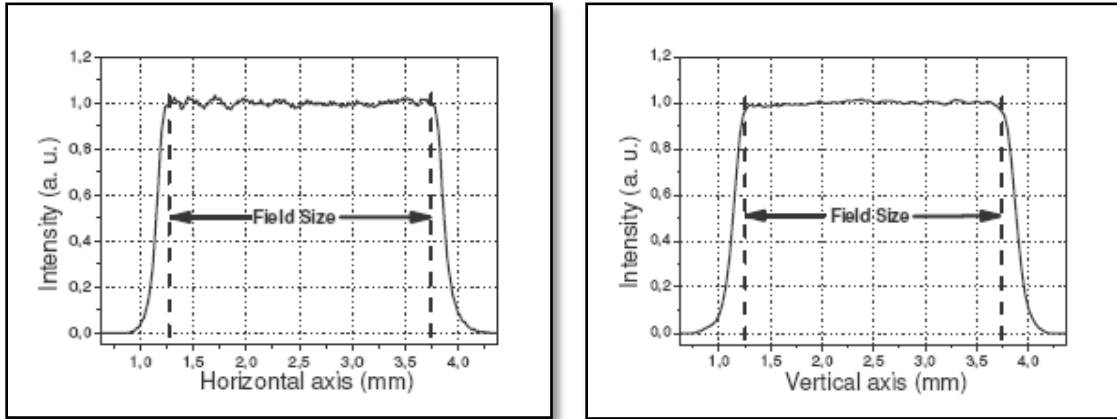
Figure 51: Typical Beam Profiles with the Flat-top Optics
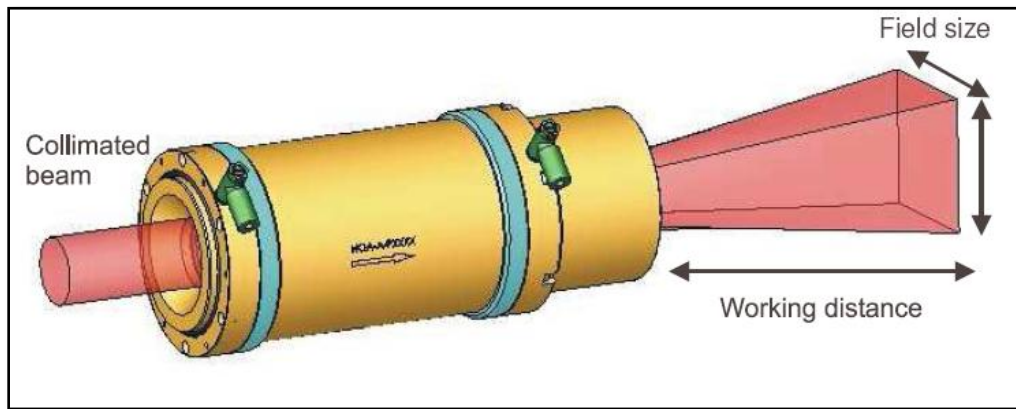
Figure 52: Illustration of the Flat-top Optics

4.4 Complete Apparatus and Methodology

To date, there have been over 10 HILPB receivers designed and constructed. Each one served a different purpose, either to investigate a particular issue or demonstrate a certain performance. A few of the receivers that were used to obtain predominantly significant results are shown here.
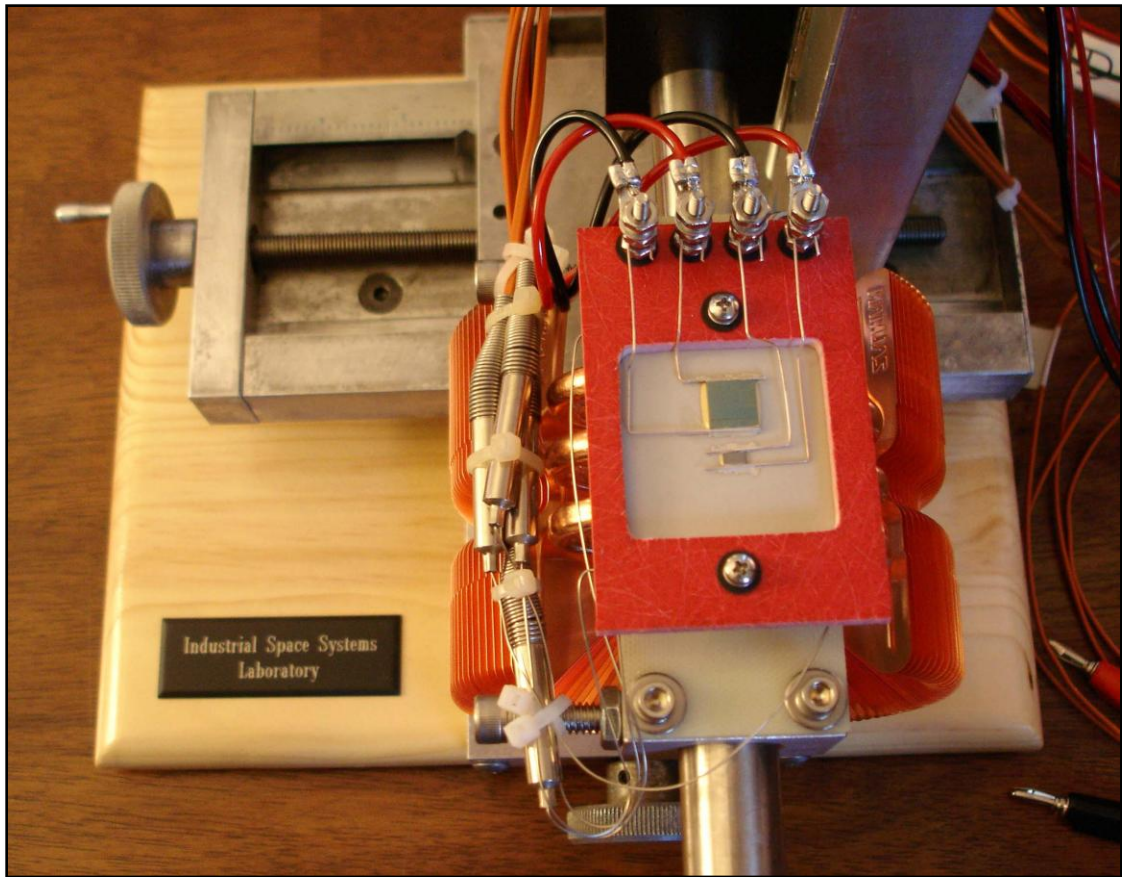
Figure 53: 9 and 40-junction Receiver
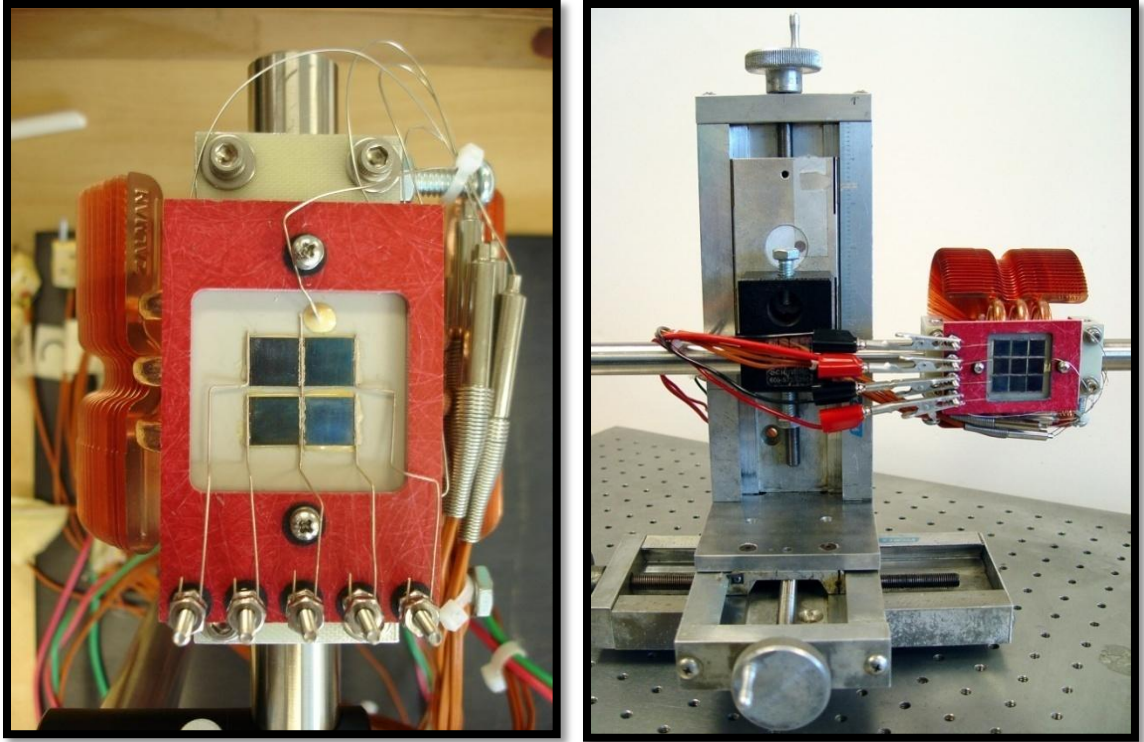
Figure 54: Four and Nine-Cell Square Array Receivers
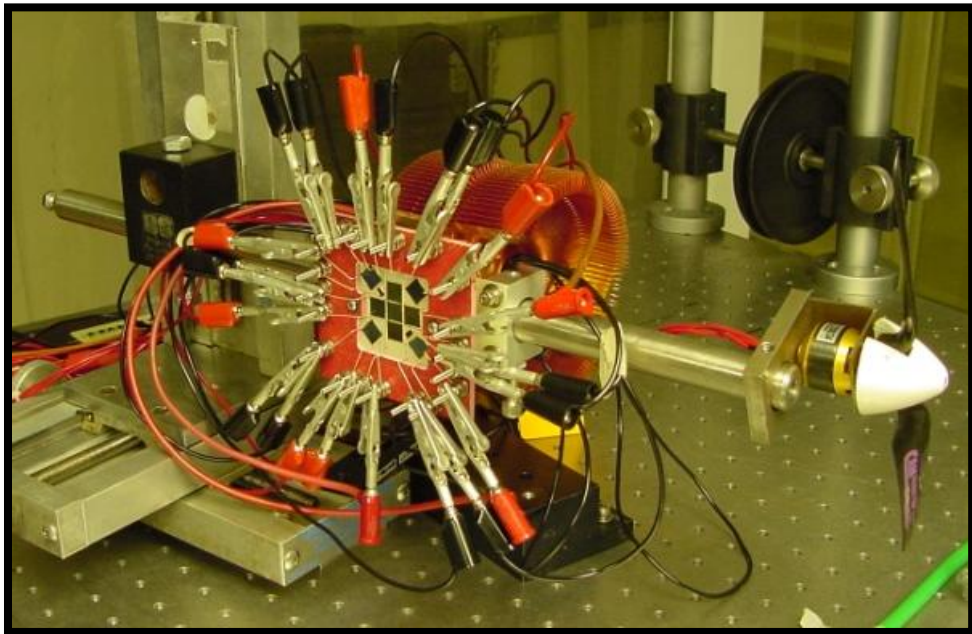
Figure 55: Eleven-Cell Radial Orientation Receiver

A typical HILPB test consists of the laser source, a mount for the optical fiber, a receiver mounted to a 3-axis translational stage, the cooling fan, the DATAQ electronics and a logging computer (Figure 56). Depending on the test requirements, additional optics stages or beam trimmers may be required. Supporting equipment such as beam guards and dumps, IR viewfinders & cameras and laser pyrometers were also used for safety as well as for calibration and alignment.
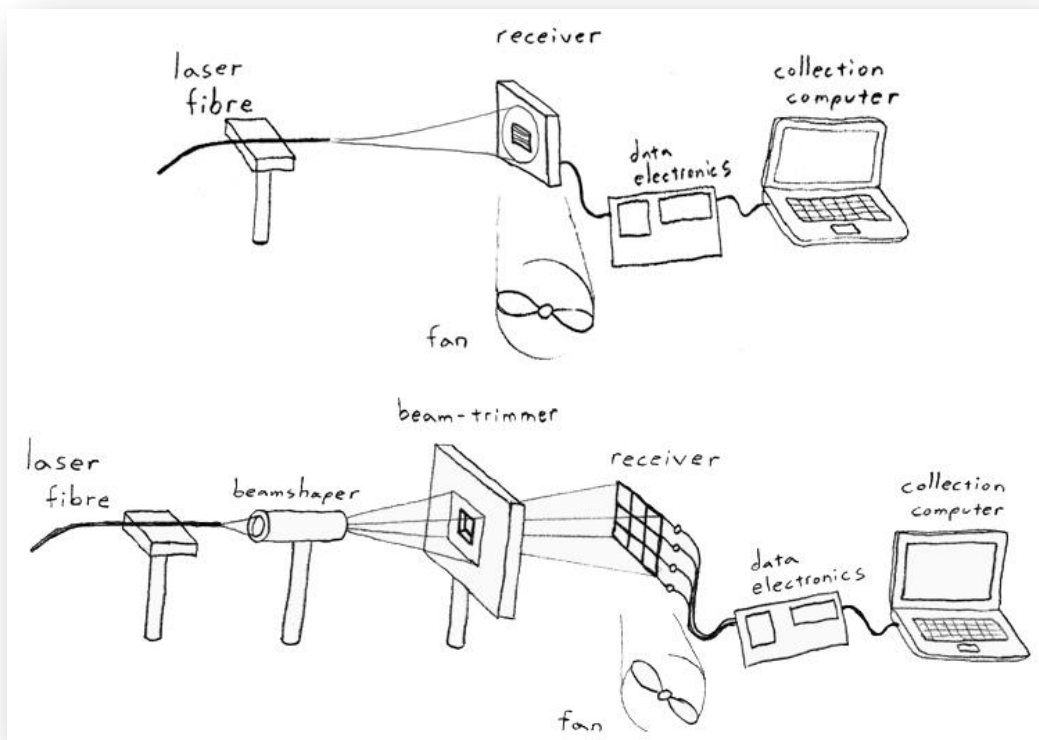
Figure 56: Illustration of the HILPB Test Rig

When conducting a test, the first thing was to check the laser calibration with a meter to insure that it was operating to its full potential. Next, all of the hardware for the experiment was fastened down to the optical bench and aligned as eyesight permits. At

this point the appropriate electrical connections were made, and the DATAQ was brought online. The laser was then operated at a relatively low intensity while the receiver position was adjusted in three axes, until the maximum output power was generated. This was accomplished by continually sweeping the load to trace new I-V curves at each new location of the receiver, until the output power of the receiver was observed to 'peak'. Performing this initial alignment was usually the most involved step in the process. The laser power was then increased to the levels required by the test plan, and the receiver was once again 'peaked', typically requiring only minor adjustment. This final adjustment was necessary due to wave-front variations over the operational range of fiber coupled lasers, and with extended tests it was a good practice to periodically recheck the alignment. At this point, the test plan was executed, while the cooling fan was controlled to regulate the receiver temperature. Devices such as IR viewfinders and cameras were used to image the beam and make notes about the size, distance, amount and alignment of the illumination. These observations would later be used to calculate efficiencies.

The amount of power developed by the receiver is automatically reported by the DATAQ system, but the efficiencies must be manually calculated. For the purposes of this research, the efficiency calculations describe the amount of photonic energy illuminating the cells with respect to the amount of generated power of the receiver. The focus is on developing the greatest amount of power at high efficiencies, and as such the performance of the HILPB receiver refers to the isolated unit that receives photonic energy and converts it into electric energy while dissipating the excess thermal energy.

This performance is dependent on the response of the VMJ cells to laser energy at a given frequency, intensity and profile, the geometric packing efficiency of the VMJ cells on the surface of the receiver, the capacity of the thermal system to reject the excess heat, and the efficiency of the electronics to maximize and measure the power output. It does not include the factors associated with the generation and transmission of the laser energy, and it takes into account the over-fill of the beam beyond the convertible surface of the VMJ cells.

CHAPTER V

EXPERIMENTAL RESULTS

Various apparatus was designed and constructed to first evaluate the feasibility of using the VMJ cells in a HILPB application, and then to start to answer some of the more complex issues through experimentation. The performance of a parallel array of cells was observed with different geometries, under different intensities, wavelengths and wave fronts. The tests were conducted at the NGST and LIMO laser laboratory. The limited availability of these laser testing facilities facilitated the need to conduct efficient test plans, and a great emphasis was placed on safety due to the weapons-grade nature of the lasers.

Figure 57: AFRL and CSU Personnel in the NGST Lab

5.1   Parallel Cell Back-Feeding

The purpose of this test was to investigate the back-feeding phenomenon of VMJ cells wired in parallel. This effect is encountered in a conventional solar array under conditions where they are subjected to non-uniform illumination (such as from partial shading or debris on the panel), and this is commonly solved by inserting blocking diodes between the cells to prevent the current flow from back-feeding into a weaker cell. The

downside of doing this is that a voltage drop will occur across the diodes during normal operation of the array, resulting in a slightly lower output power.

Since the beam profile of the laser is non-uniform, this phenomenon could be encountered when using a parallel array of VMJ cells for HILPB. To investigate this, an experiment was conducted on a multi-cell receiver, using two of the available VMJ cells (referred to as the top and the top-right cell) connected in parallel. These particular cells were chosen because they represent two different grades of VMJ cells, with one offering consistently better performance than the other. This would establish the conditions for the imbalance to occur. Low-loss diodes were selected for the blocking application, and these could be introduced into the circuit to observe their effects. Ammeters were used to measure the amount and polarity of the individual branch current contributions.

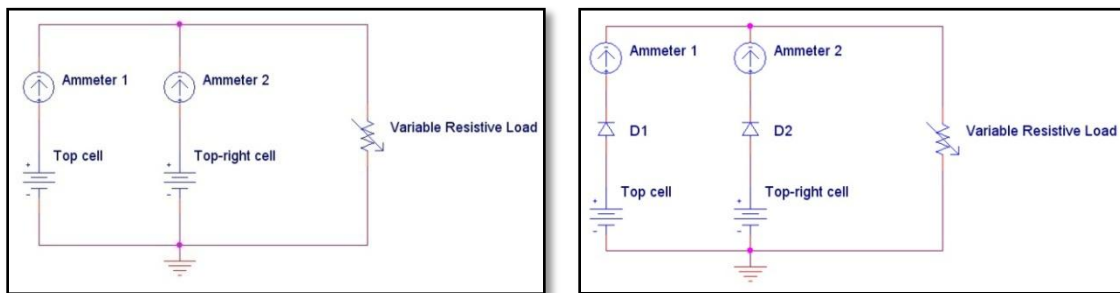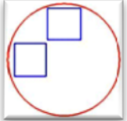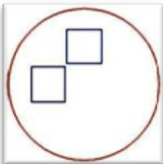Figure 58: Connections With and Without Blocking Diodes

The test was conducted using a 200 watt 980 nm laser, with the beam directed in proximity of the two cells as to allow for each to receive the similar profile. The test was conducted with three different amounts of beam overfill to vary the profile illuminating the cells, and was repeated both with and without the blocking diodes in the circuit. The

79

receiver temperature was maintained within 50–60 °C. The results of these tests are
shown below, and the relative diameter and placement of the beam overfill is illustrated.
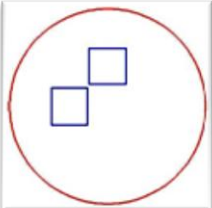
	Without Diodes Current (amps)	With Diodes Current (amps)
Top cell	0.233 A	0.147 A
Corner cell	-0.097A	0.0 A

Figure 59: Cell Back-feeding with Small Overfill

	Without Diodes Current (amps)	With Diodes Current (amps)
Top cell	0.151 A	0.129 A
Corner cell	-0.003A	0.0 A

Figure 60: Cell Back-feeding with Medium Overfill

	Without Diodes Current (amps)	With Diodes Current (amps)
Top cell	0.189 A	0.122 A
Corner cell	-0.087A	0.004 A

Figure 61: Cell Back-feeding with Large Overfill

The negative currents can be seen in Figures 59-61 when the blocking diodes are
not present, and represent the back-feeding of the current from the strong cell into the
weak cell. The addition of the blocking diodes does correct the flow, but at the expense
of the inherent power loss through the diodes, to the extent that the diodes did not
improve the overall output power for any of the experimental results, and it was observed

in these instances that their presence was more detrimental than beneficial. This is due to the voltage drop losses exceeding the branch current gains, leading to a decrease in output power.

5.2   Radial versus Square Geometry

The purpose of this test was to determine an effective orientation of the cells with respect to the non-uniform laser illumination. Since the junctions within a VMJ cell are all oriented in the same direction, each one will not receive equal intensities of laser light. This permits the possible scenario where the VMJ cell may be limited by the performance of its weakest junction, and the excess energy of the other junctions would then be wasted.

To explore this premise and quantify the degree of its severity, two receiver geometries are considered, a 9-cell square array and a 9-cell radial orientation array. The 9-cell square array simply orients all of the p-n junctions in the same direction, which enables for the maximum junction to junction delta when illuminated with a Gaussian beam. The receiver is hard-wired for three stacks of three parallel cells, and for this test each stack is patched together to produce nine parallel cells.
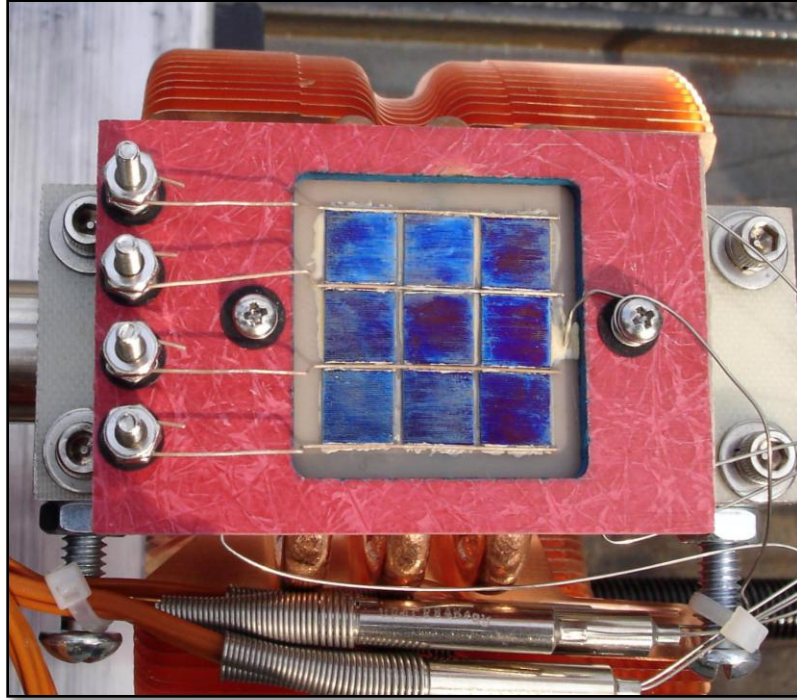
Figure 62: Nine-Cell Square Receiver

The 9-cell radial orientation array places all of the junctions in eight of the cells on a radial to the center-point of the receiver. When centered with the laser beam, the Gaussian profile will extend down the length of each p-n junction, rather than across the junctions. In this way, the junction-to-junction delta is minimized, resulting in an equal average illumination. A compromise to this rule is made by placing a single cell at the center of the array, for the purpose of maximizing packing density. Each cell has its own dedicated pair of leads. This receiver also has two additional miniature cells mounted in the corners, which were not used for this test.
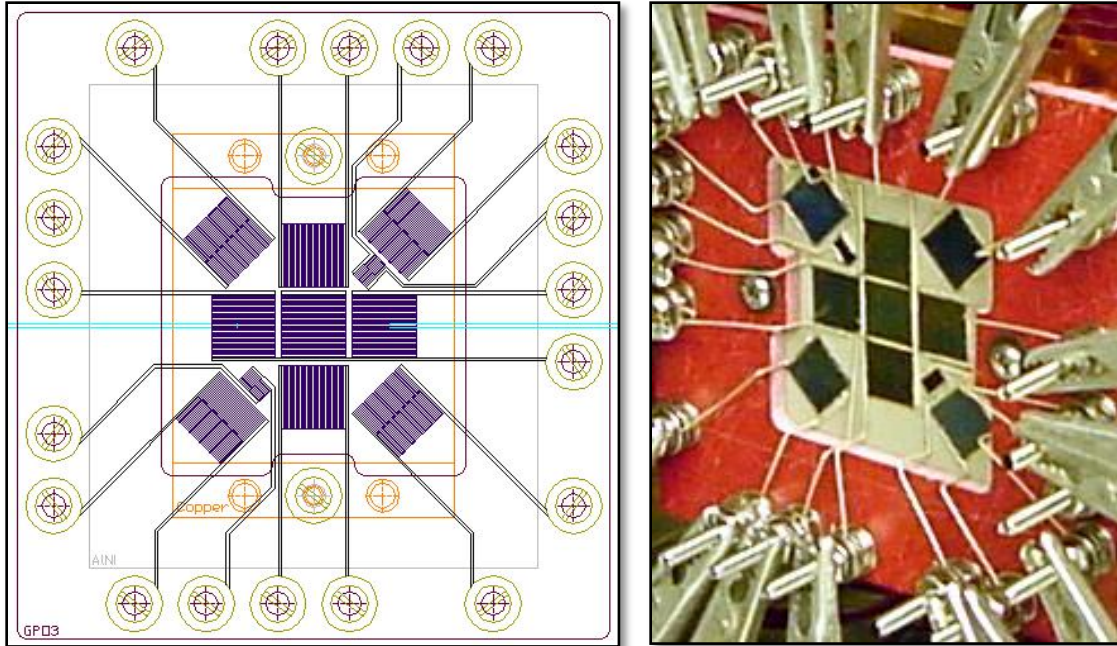
Figure 63: Radial Orientation Receiver Layout

The first objective of this test was to establish a baseline maximum power measurement for the subsequent tests. The nine-cell square receiver was illuminated with a 980 nm laser. The receiver position was adjusted in three axes to obtain the maximum output power with the laser intensity set to 200 watts, resulting in a 30 % illumination as depicted in Figure 64. The output of the receiver was measured to be 23 watts, and the temperature was regulated within 50–60 °C.
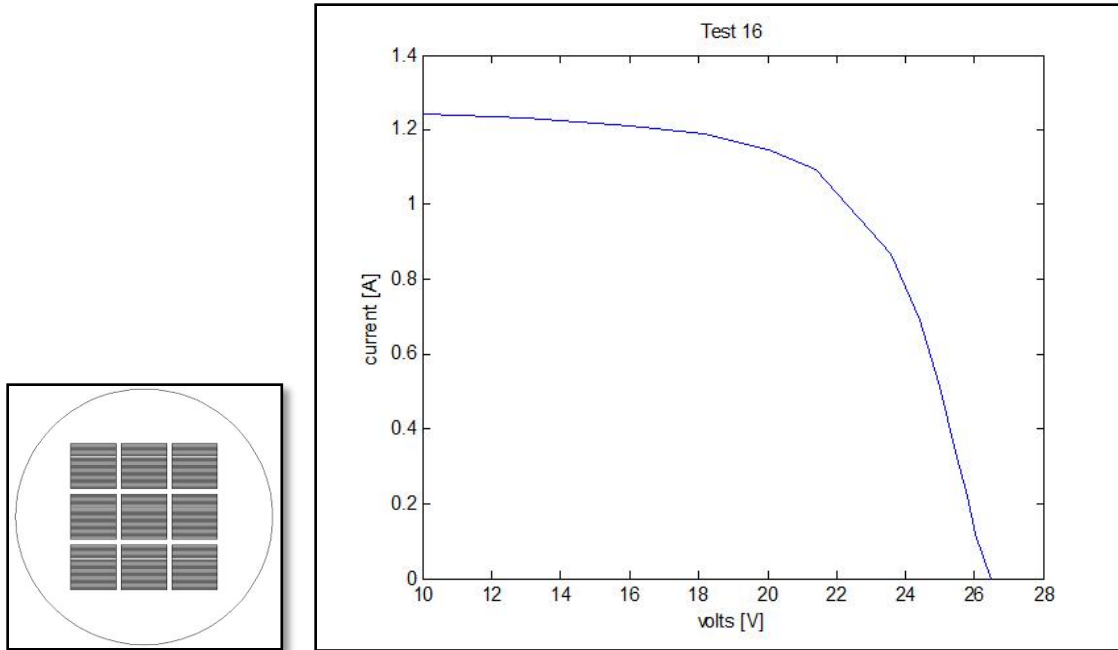
Figure 64: Square Receiver at 30 % Fill, 23 Watts P_{mp}

For the next part of the test, the radial orientation receiver was used. First, the same conditions were used as with the previous test to align the receiver at full laser intensity, starting with the inner grouping of five cells. Next the individual cells in the array were characterized in order to determine their contribution to the overall output of the receiver. The resulting output I-V curves are shown below, and the relative diameter and placement of the beam overfill is illustrated.
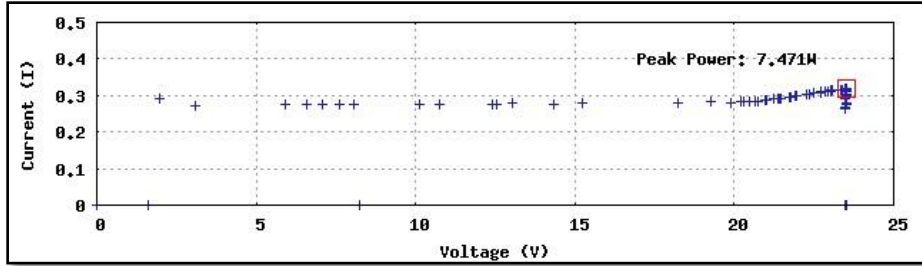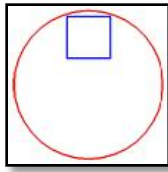
Figure 65: Top Cell I-V Curve, 7.471 Watts P_{mp}
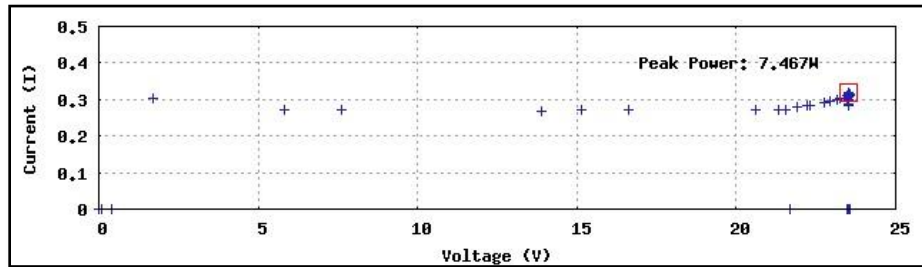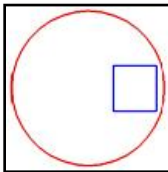
Figure 66: Right Cell I-V Curve, 7.467 Watts P_{mp}
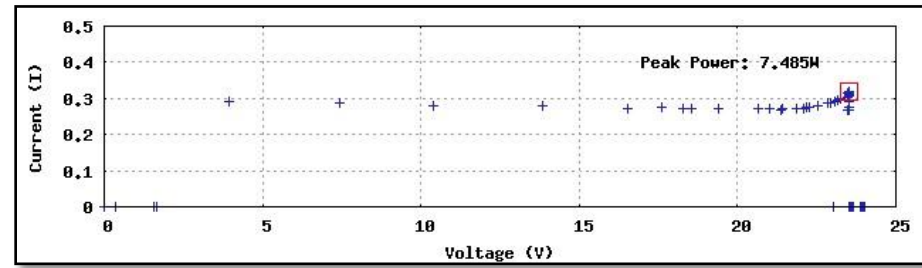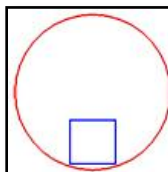
Figure 67: Bottom Cell I-V Curve, 7.485 Watts P_{mp}
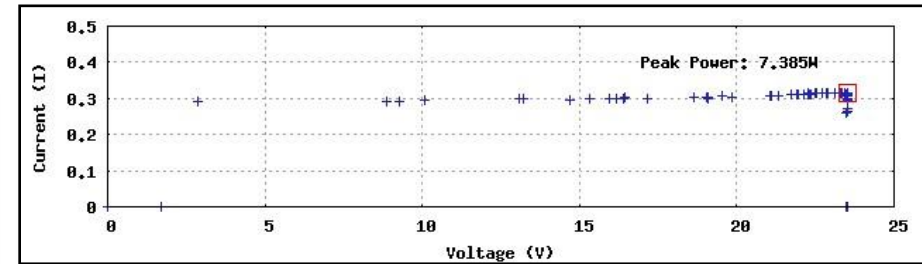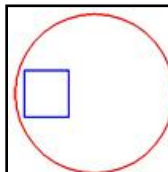
Figure 68: Left Cell I-V Curve, 7.385 Watts P_{mp}
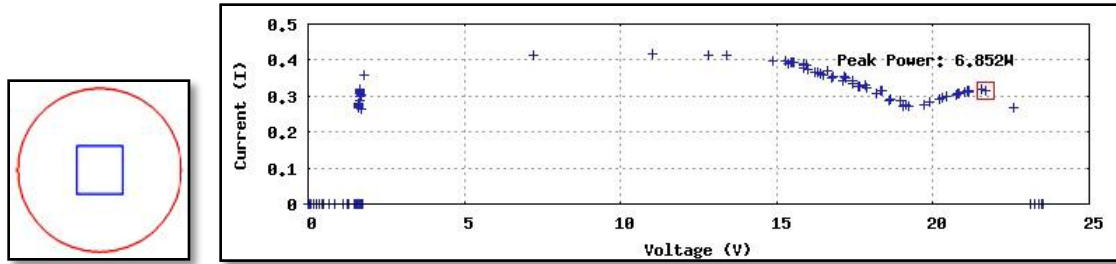
Figure 69: Center Cell I-V Curve, 6.852 Watts P_{mp}

It is interesting to note that the center cell, where the beam energy is the strongest, did not have a higher output power than the four immediately surrounding cells. This may be attributed to the fact that unlike the surrounding cells, the center cell does not comply with the radial configuration, and even though it is receiving the highest intensity portion of the laser beam, it is unable to convert the energy efficiently since it is seeing an uneven power distribution across its p-n junctions. This is an indication into the magnitude of the detrimental effect of uneven power distribution across the p-n junctions, and is also a first glimpse into the validity of the radial arrangement of the surrounding cells.

For the next part of the test, data was collected from both the inner four and five cell arrangements wired in parallel. These tests were performed with the same optical alignment as before and at the 200W laser power level. The resulting output I-V curves are shown below, and the relative diameter and placement of the beam overfill is illustrated.
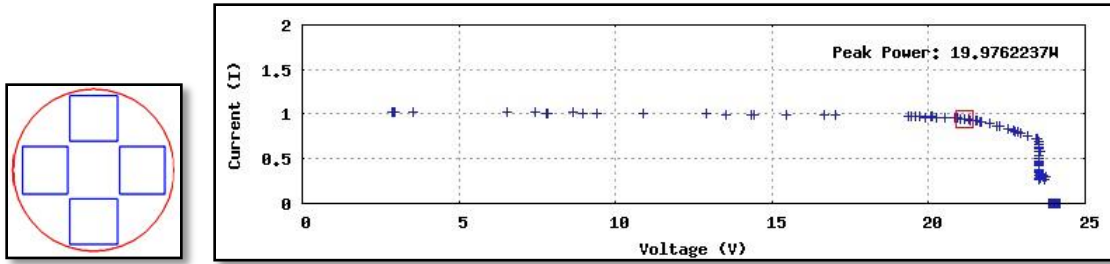
Figure 70: Four-Cell I-V Curve, 19.976 Watts P_{mp}
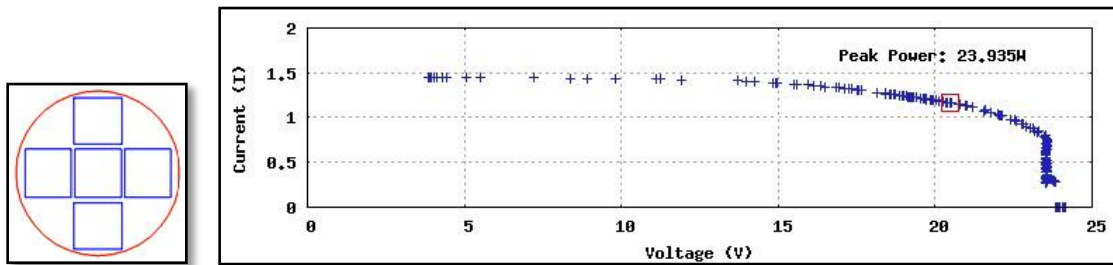
Figure 71: Five-Cell I-V Curve, 23.935 Watts P_{mp}

A comparison of the results obtained in Figures 70 and 71 with those in Figures 65-69 shows that the four inner cells are contributing the majority of the radial receiver's total output. Although the center cell is illuminated by the most intense part of the laser beam, it is converting less energy than its four neighboring cells. As stated earlier, this may be attributed to the center cell not complying with the radial configuration.

The five-cell output power of 23.935 watts (Figure 71) was calculated to be a conversion efficiency of 22.75 %. Comparing these results with those in Figure 64 demonstrates that five cells in the radial orientation can outperform nine cells in the square orientation, providing further validation of the radial concept.

For the final portion of the test, the over-fill of the receiver was increased to involve more of the corner cells in the overall output. As with all of the previous parts of

87

this test the laser was operated at 200 watts, and the receiver temperature was regulated within 50–60 °C.
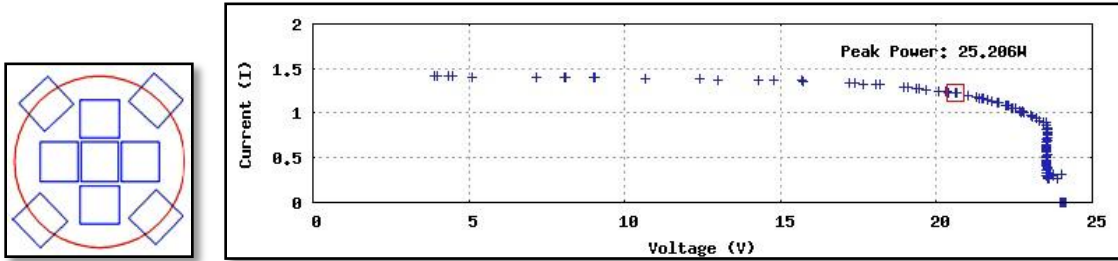
Figure 72: 48.09 % Illum., 25.286 Watts P_{mp} at 26.2 % ŋ
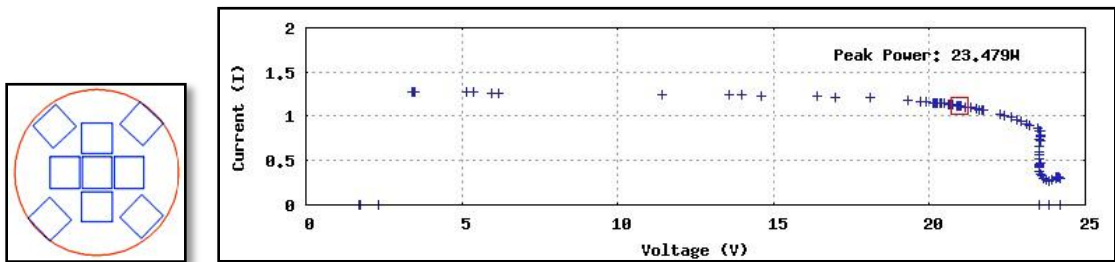
Figure 73: 37.72 % Illum., 23.479 Watts P_{mp} at 31.12 % ŋ
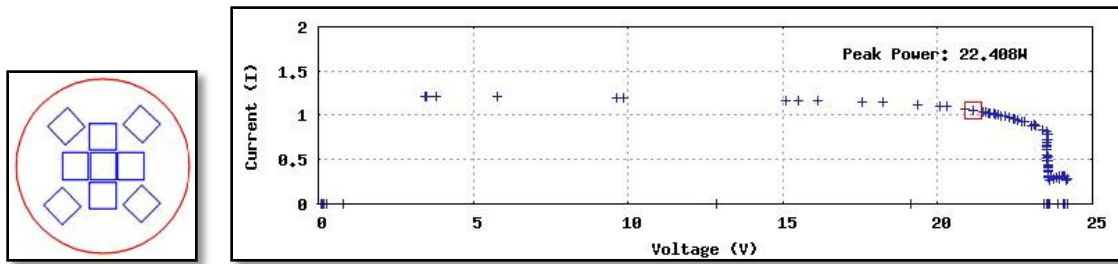
Figure 74: 25.24 % Illum., 22.488 Watts $P_{mp,}$ at 44.39 % ŋ

The smallest beam over-fill yielded the highest output power collected during the test, at 25.206 watts. At this level of overfill, the conversion efficiency was calculated to

be 26.2 %. The highest conversion efficiency was found to be with the largest beam over-fill, at 44.39 %.

These results show that a radial orientation of the p-n junctions on the receiver face will outperform a uniform orientation, and even with less VMJ cells. This demonstrated the impact of the cell geometry in the receiver design.

5.3   Output Linearity

The objective of this test was to establish an input-output relationship across different illumination intensities.   The nine-cell radial orientation receiver was illuminated with a 980 nm laser. The receiver position was adjusted in three axes to obtain the maximum output power with the laser intensity set to 58.2 watts, with an over-fill as shown in Figure 75.
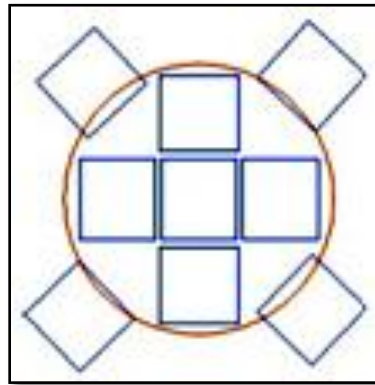
Figure 75: Linearity Test Over-fill

At the 58.2 watt intensity, the load was varied to obtain the characteristic I-V curve of the receiver. This was repeated at laser intensities of 118, 146 and 200 watts, without readjusting the amount of beam overfill, while the temperature of the receiver was controlled between 50-60 °C. The resulting output data is shown below.
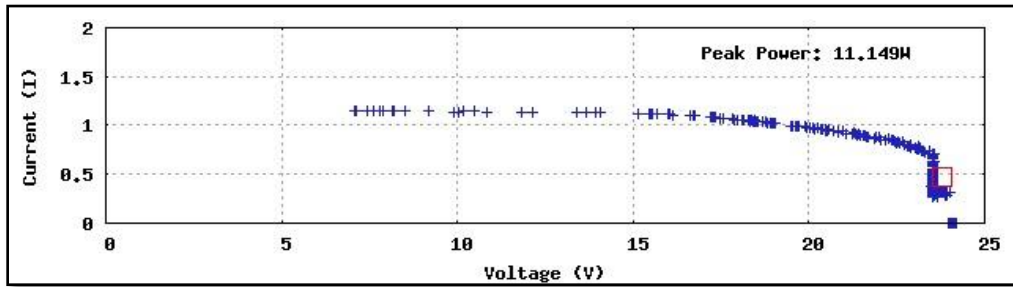
Figure 76: Linearity Test at 58 Watts
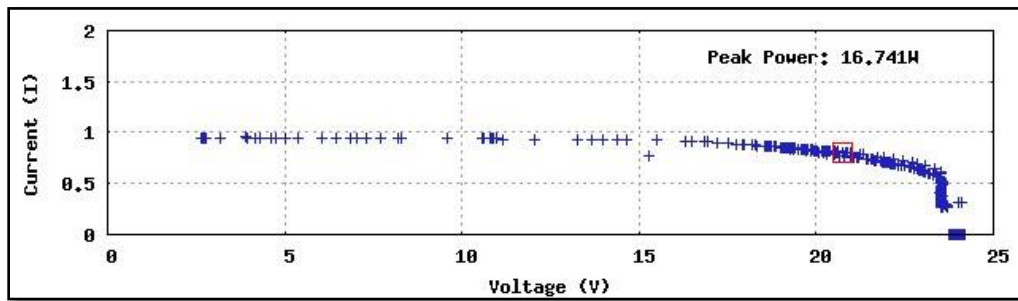
Figure 77: Linearity Test at 118 Watts
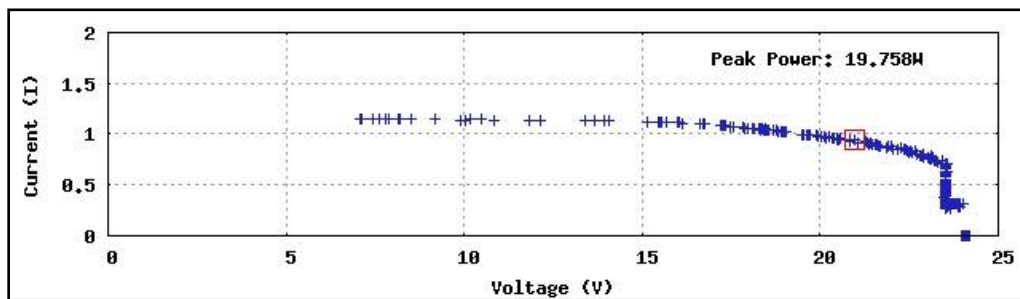
Figure 78: Linearity Test at 146 Watts

90
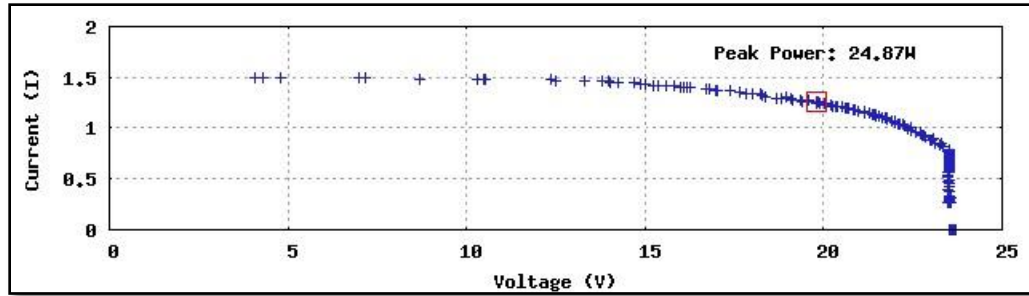
Figure 79: Linearity Test at 200 Watts

A comparison graph of the laser input power versus converted electrical output power is shown in Figure 80. It can be seen that the response of the receiver for this range of optical power is fairly linear, within the 200 watts of available laser energy.
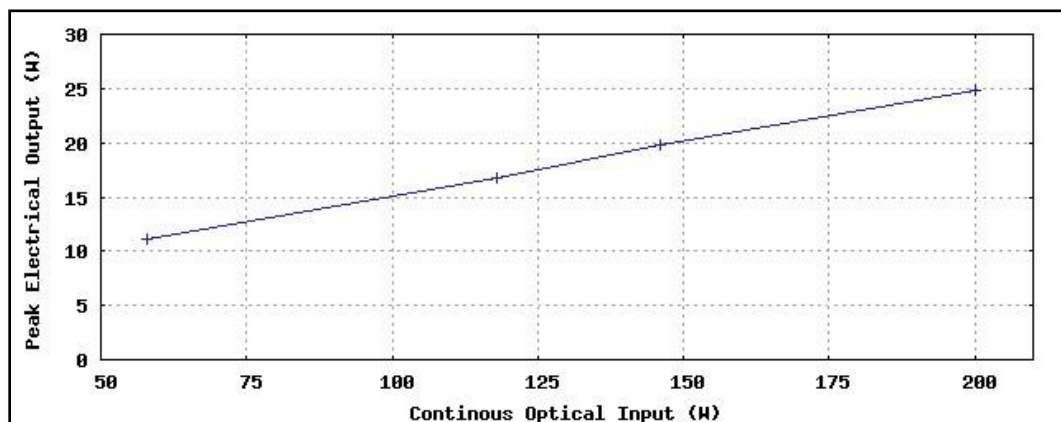
Figure 80: Linear Input-Output Power Relationship

5.4   Determining the Optimal Laser Wavelength

At low injection levels, Shockley equations are adequate for describing the current-voltage relationship of p-n junction semiconductor devices. High injection levels

cause a change in the carrier generation and recombination process, resulting in a narrowing of the band gap [60]. If the conversion efficiency is to be maintained at high intensities, the energy wavelength must adhere to this non-linear constraint. In semiconductor material, beyond the cutoff wavelength the absorption coefficient decreases rapidly [61], as illustrated by the knee in the silicon curve in Figure 81. In the case of the band-gap narrowing, the curve would shift, and depending on the thickness of the semiconductor material there may not be sufficient depth of penetration for efficient photoelectric conversion, resulting in saturation. Another possible phenomenon is the increase in the wavelength of light as it penetrates through the silicon, due to oblique collisions in the capture cross section, until the energy is beyond the band-gap of the material. Either scenario would lead to an increase in heating and a decrease in efficiency.
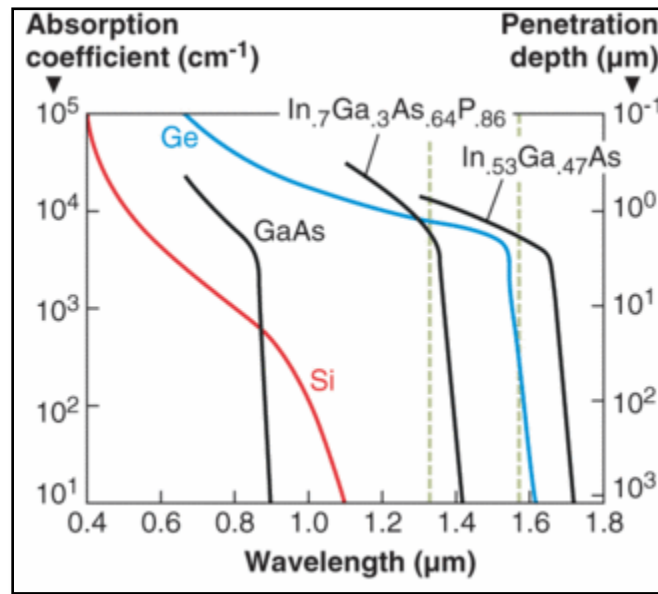
Figure 81: Semiconductor Optical Absorption Coefficients

Although the original quantum efficiency information for the VMJ cells can be used to initially determine the best range for narrowband illumination, this needs to be verified at continuous high intensities to verify that saturation is not occurring. An experiment utilizing similar lasers at different operational frequencies will verify this, and reveal the optimal operating frequency for maximum efficiency. Unfortunately, current technology does not provide for an infinitely tunable high power laser, but there are standardized frequencies that can be selected.

Three standard frequencies within the range of interest were available to conduct this experiment, and three corresponding lasers at 808, 940 and 976 nm were provided by LIMO laser. A single cell receiver was used, and to maintain a control during the experiment the same laser fiber was left in alignment, leaving only the laser diode module to be replaced between trials. These three lasers had a maximum output of 70 watts, and were identical in all ways except for their frequencies.

The tests were conducted across the full power range of the laser, and the receiver was aligned in three axes until the maximum output power was achieved. This occurred at an over-fill amount where 26 watts of laser energy was illuminating the cell, and these results are tabulated in Tables II, III and IV, with the maximum output power of each test indicated.

TABLE II: 976 NM WAVELENGTH RESULTS

LIMO70-F200-DL976				LIMO70-F200-DL976			
Current Setpoint Amps (A)	Rated Optical Power Watts (W)	Operating Optical Power Watts (W)	Adj. Optical Window Transmittance Watts (W)	Impinging Optical Power Watts (W)	VMJ Peak Power Watts (W)	Conversion Efficiency (%)	Receiver Temp. (°C)
10	9.8	9.114	8.52159	3.6217	1.5481	42.74	24.1
20	25.4	23.622	22.08657	9.3868	3.5402	37.71	24.7
30	40.9	38.037	35.564595	15.1150	5.1722	34.22	27.5
40	56	52.08	48.6948	20.6953	6.4459	31.15	30.1
50	70	65.1	60.8685	25.8691	7.2430	28.00	32.6

TABLE III: 940 NM WAVELENGTH RESULTS

LIMO70-F200-DL940				LIMO70-F200-DL940			
Current Setpoint Amps (A)	Rated Optical Power Watts (W)	Operating Optical Power Watts (W)	Adj. Optical Window Transmittance Watts (W)	Impinging Optical Power Watts (W)	VMJ Peak Power Watts (W)	Conversion Efficiency (%)	Receiver Temp. (°C)
10	9.9	9.207	8.608545	3.6586	1.5198	41.54	24.4
20	25.7	23.901	22.347435	9.4977	3.5398	37.27	25
30	40.9	38.037	35.564595	15.1150	5.0675	33.53	27.6
40	55.1	51.243	47.912205	20.3627	6.1611	30.26	30.1
50.8	70	65.1	60.8685	25.8691	6.8263	26.39	32

TABLE IV: 808 NM WAVELENGTH RESULTS

LIMO70-F200-DL808				LIMO70-F200-DL808			
Current Setpoint Amps (A)	Rated Optical Power Watts (W)	Operating Optical Power Watts (W)	Adj. Optical Window Transmittance Watts (W)	Impinging Optical Power Watts (W)	VMJ Peak Power Watts (W)	Conversion Efficiency (%)	Receiver Temp. (°C)
10	1.7	1.581	1.478235	0.6282	0.3131	49.83	22.5
20	20.3	18.879	17.651865	7.5020	1.8050	24.06	28.7
30	38.9	36.177	33.825495	14.3758	3.0695	21.35	35.4
40	56.4	52.452	49.04262	20.8431	3.9837	19.11	41.8
49.4	70	65.1	60.8685	25.8691	4.6798	18.09	47.2

The output power, I-V curves and efficiency data are plotted in Figures 82, 83 and 84, along with images of the experiment. Although the laser beams are observed as three different colors, they are all in the IR region that is invisible to the human eye. The coloring effects are artifacts of the digital camera used to image the laser beam.
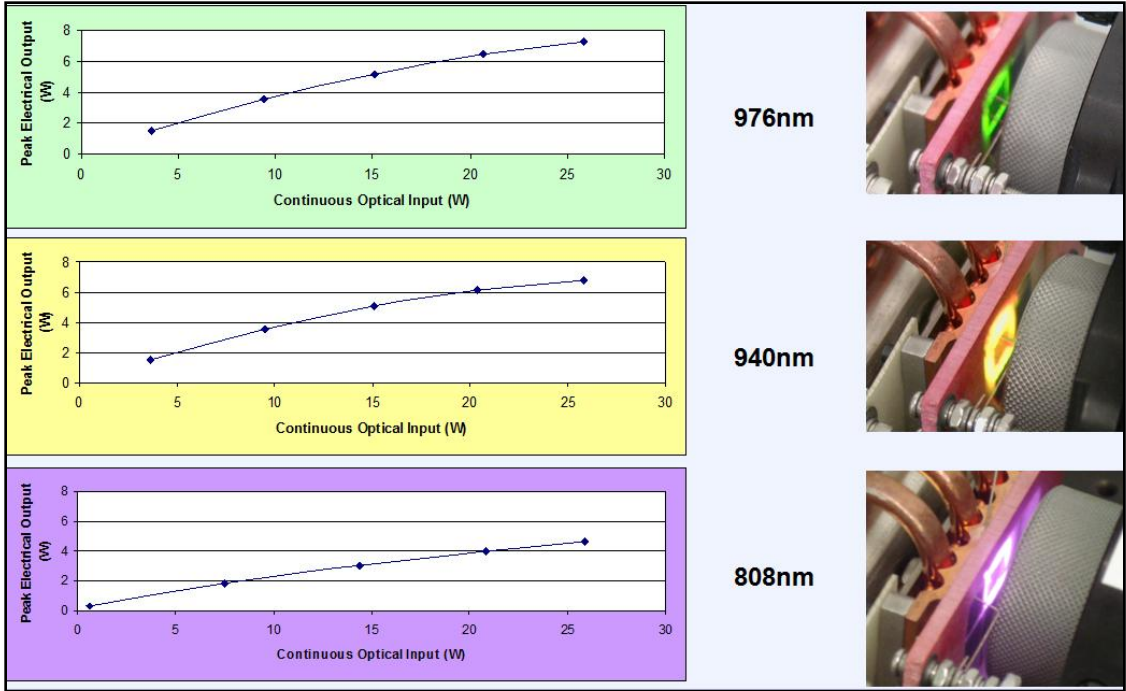
Figure 82: Wavelength Input versus Output
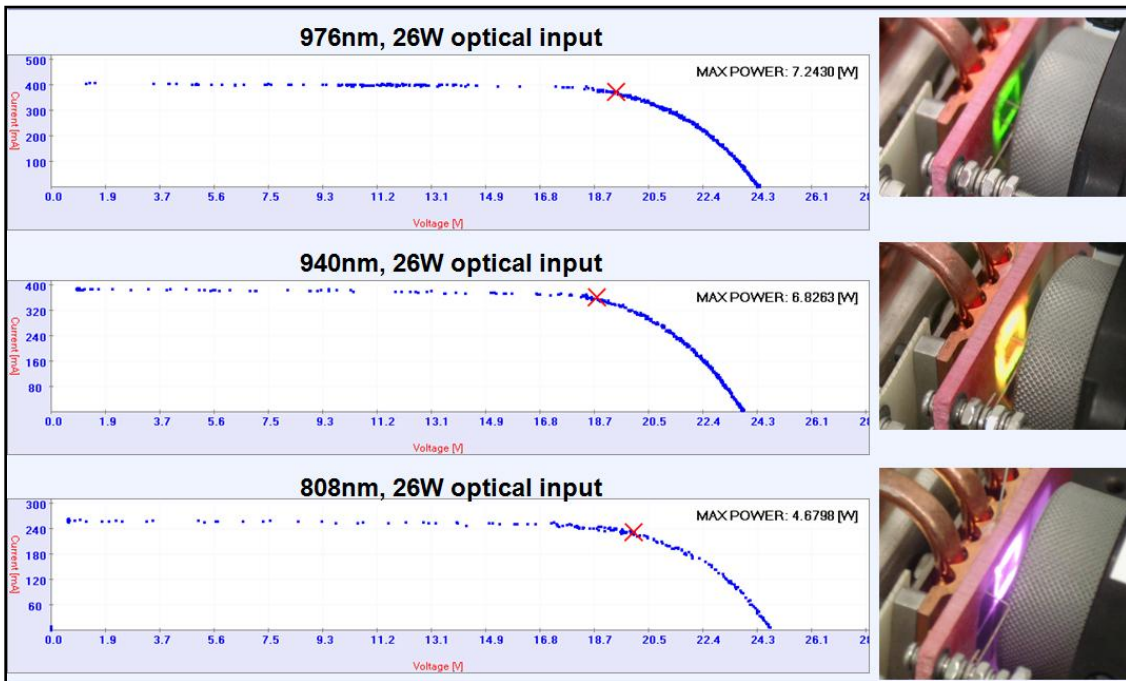
Figure 83: Wavelength Maximum Power I-V Curves

95
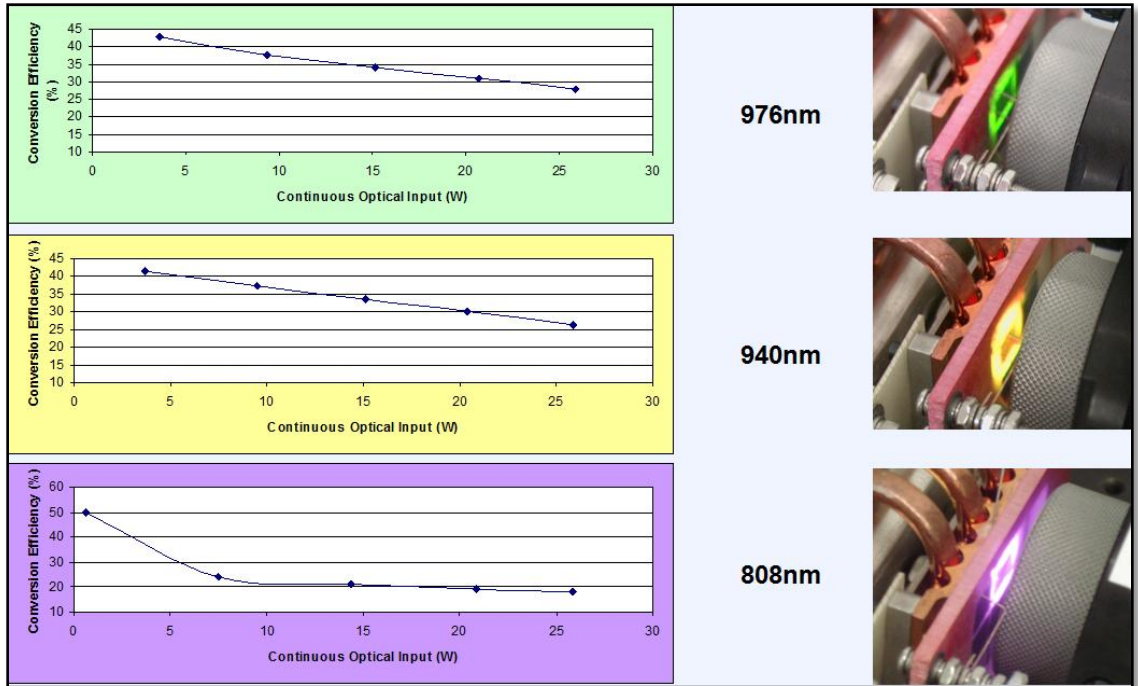
Figure 84: Wavelength Conversion Efficiencies

The results from these tests clearly indicate that the 976 nm wavelength offers the best high intensity performance with these receivers. Comparison graphs are shown in Figures 85 and 86 to further illustrate this point. It is interesting to note that at the lowest intensity the 808 nm wavelength offered an efficiency of almost 50 %, but this quickly dropped at higher intensities. Although this may be indicative of saturation, it may also be that a large amount of this energy is being reflected back from the surface of the cells at these intensities. This was noted in the pictures by the amount of visible scattering around the cell at the 808 nm frequency, and warrants further investigation in the future.
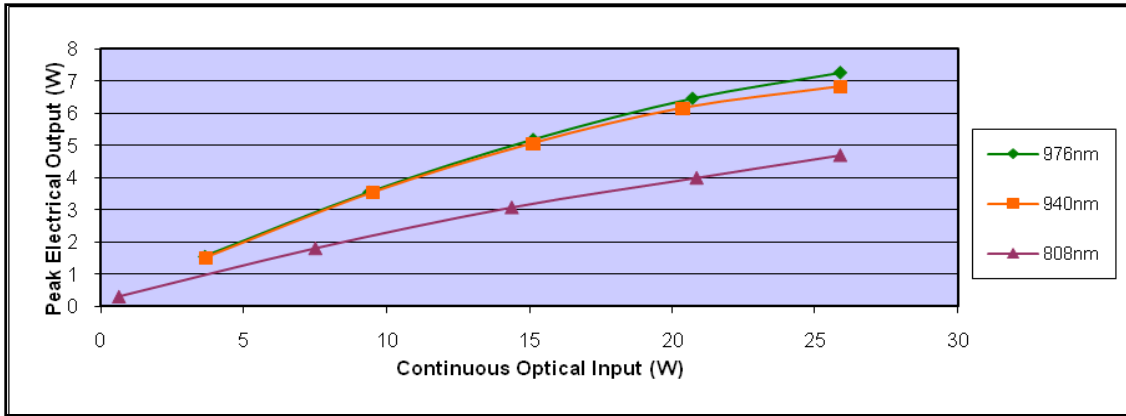
Figure 85: Wavelength Output Comparison
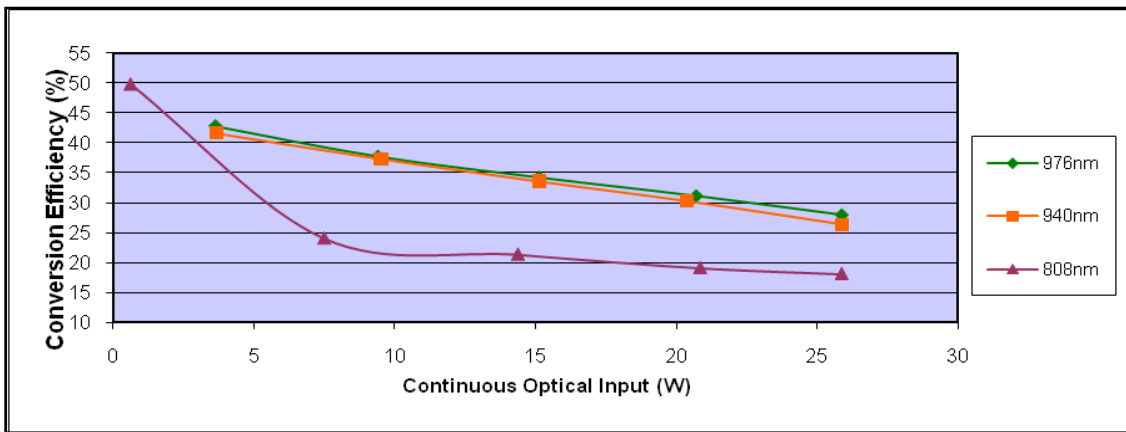
Figure 86: Wavelength Efficiency Comparison

5.5   Uniform versus Gaussian Beam Profiles

Although the typically encountered operation of a laser is in a TEM_{00} resonator mode (Gaussian), the previously discussed concern over uniform illumination of the junctions in the VMJ cell warrants an investigation into the effects. The prior experiment

97

in 5.2 successfully compensated for the non-uniform beam by considering the geometry of the receiver. In this experiment the laser beam is conditioned to a uniform state using optics stages from LIMO. The beam shaping optics delivers a 44.5 x 44.5 mm square laser beam within a 1 % variation of intensity.

The first part of the test establishes a baseline for the comparison with and without the conditioning optics. The nine-cell square receiver was selected for the test, and was illuminated with a 980 nm laser. The receiver position was adjusted in three axes to obtain the maximum output power with the laser intensity set to for different intensities, while the receiver temperature was regulated within 50–60 °C.
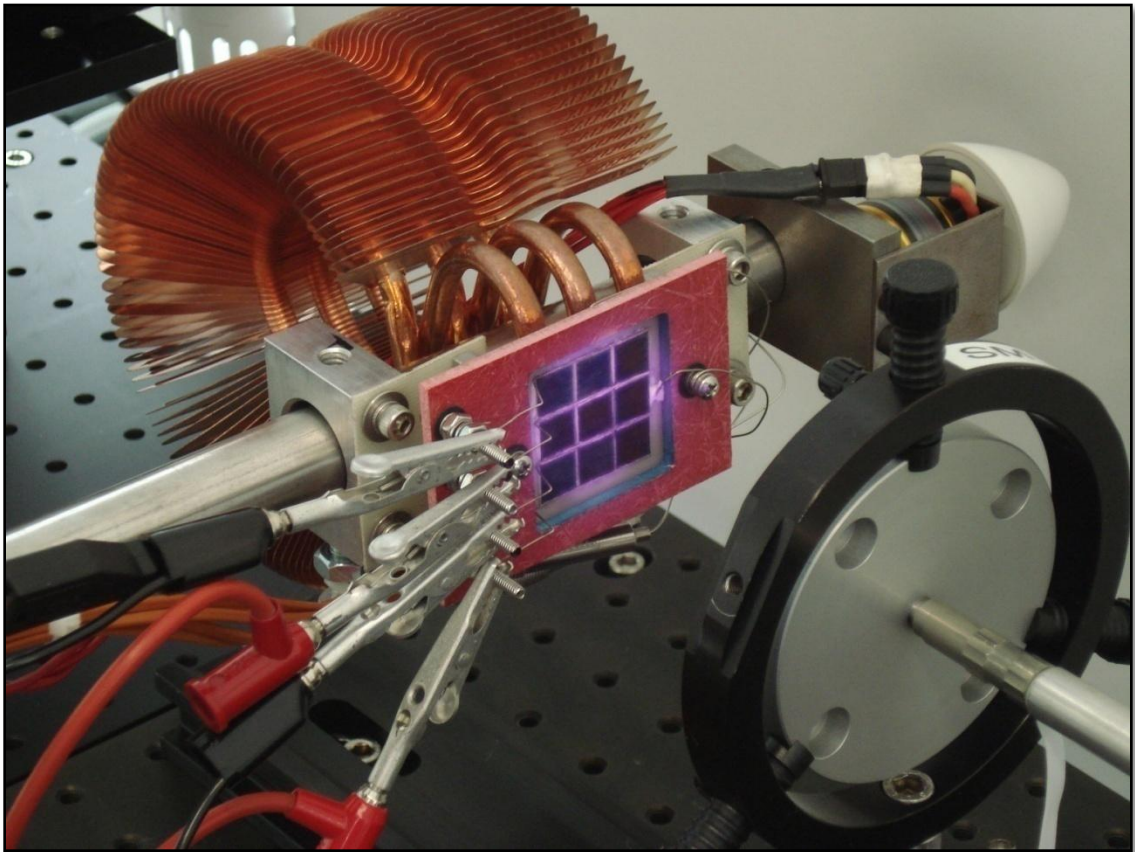
Figure 87: Nine-Cell Receiver with Gaussian Beam

98

TABLE V: GAUSSIAN BEAM RESULTS

HLU200-F400-980P2-M2			After Optical Window Transmittance Watts (W)	After Flat-Top Optics Transmittance Watts (W)	9-cell Gaussian			
Current Setpoint Amps (A)	Rated Optical Power Watts (W)	Operating Optical Power Watts (W)			Impinging Optical Power Watts (W)	VMJ Peak Power Watts (W)	Conversion Efficiency (%)	Receiver Temp. (°C)
10	30.2	28.086	26.26041	22.18794	13.8918	4.3895	31.60	29
20	91.2	84.816	79.30296	67.00464	41.9513	12.2321	29.16	37
30	150	139.5	130.4325	110.205	68.9988	18.2832	26.50	47.2
39.5	201.9	187.767	175.562145	148.33593	92.8724	23.7778	25.60	47
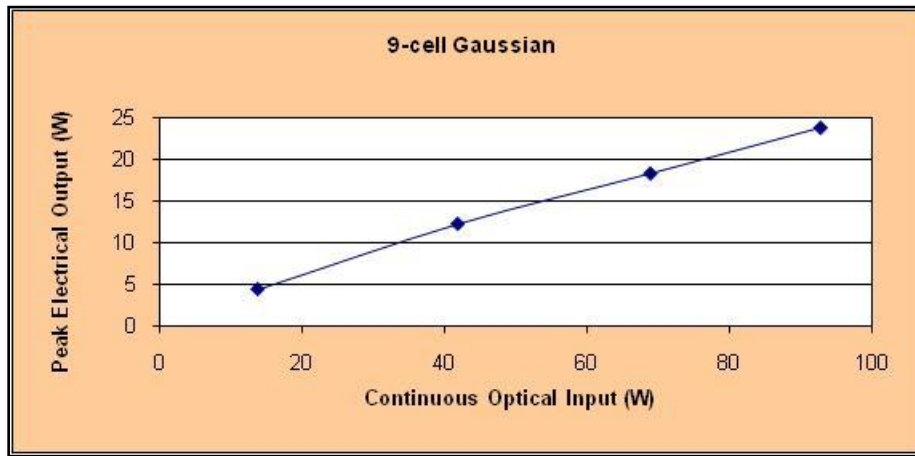
Figure 88: Gaussian Receiver Output
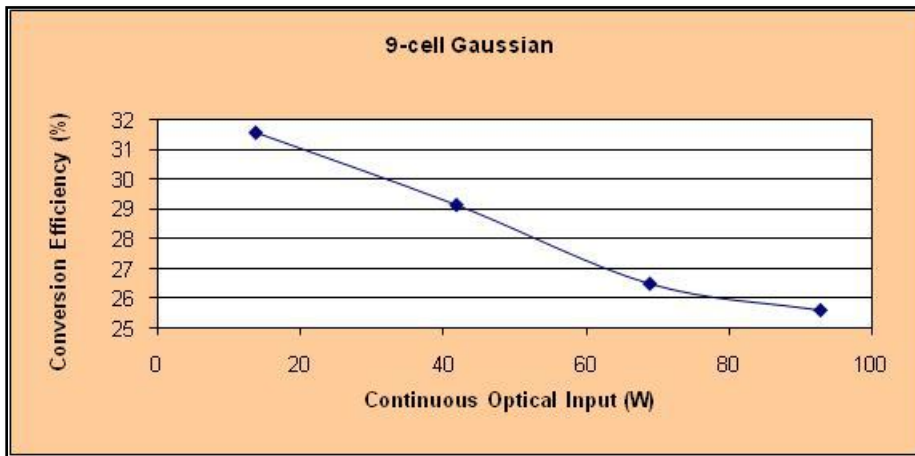
Figure 89: Gaussian Receiver Efficiencies

99

In the next stage of the experiment, the flat-top optics stage was inserted. The receiver position was re-adjusted in three axes to obtain the maximum output power with the laser intensity set to for different intensities, while the receiver temperature was regulated within 50–60 °C.
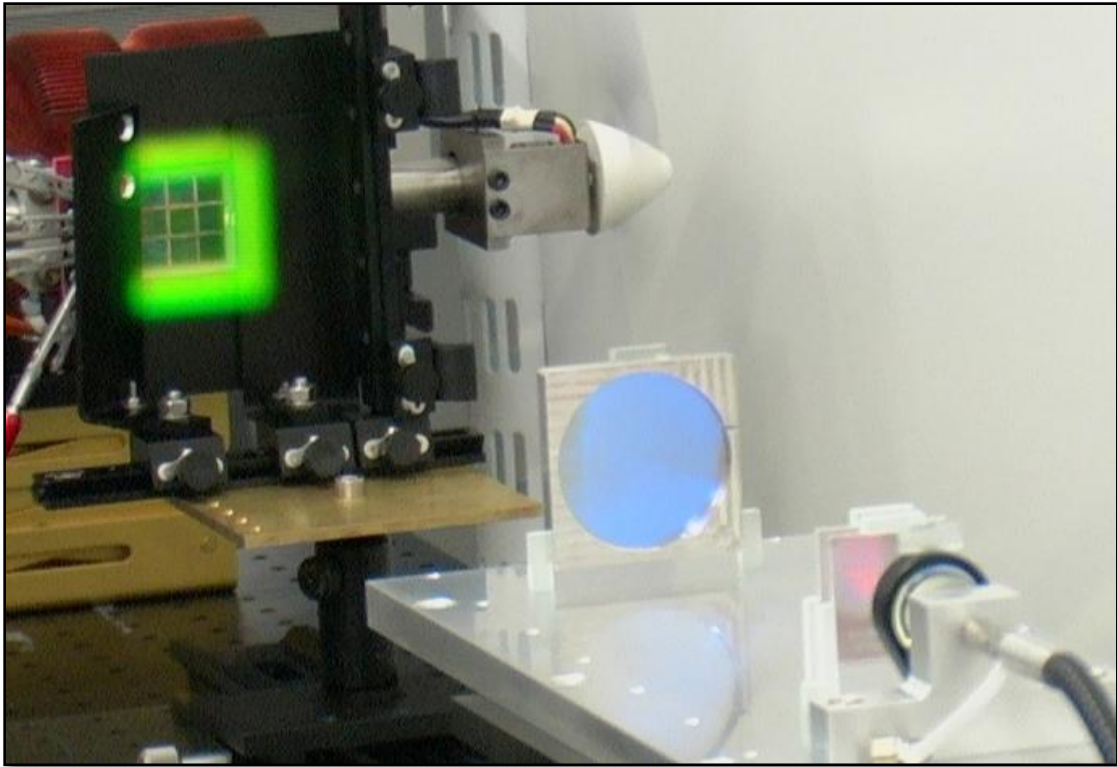
Figure 90: Nine-Cell Receiver with Flat-Top Beam

TABLE VI: FLAT-TOP RESULTS

HLU200-F400-980P2-M2			After	After	9-cell Flat-Top Optics			
Current Setpoint Amps (A)	Rated Optical Power Watts (W)	Operating Optical Power Watts (W)	Optical Window Transmittance Watts (W)	Flat-Top Optics Transmittance Watts (W)	Impinging Optical Power Watts (W)	VMJ Peak Power Watts (W)	Conversion Efficiency (%)	Receiver Temp. (°C)
10	30.2	28.086	26.26041	22.18794	7.0780	2.2668	32.03	23
20	91.2	84.816	79.30296	67.00464	21.3745	6.7194	31.44	27.2
30	150	139.5	130.4325	110.205	35.1554	10.6178	30.20	31.7
39.5	201.9	187.767	175.562145	148.33593	47.3192	13.8387	29.25	35.7
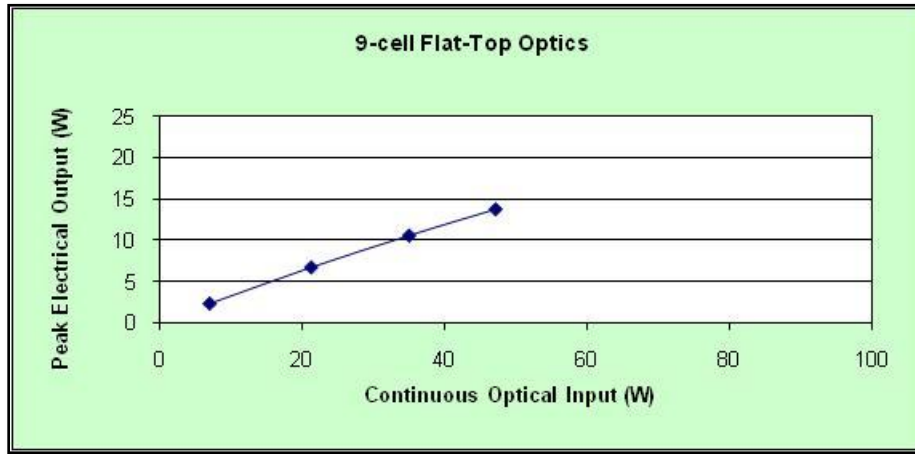
Figure 91: Flat-Top Receiver Output
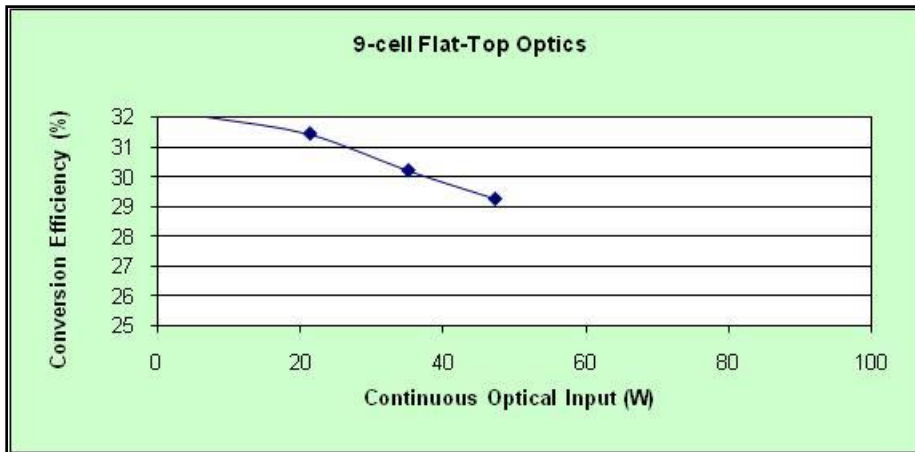
Figure 92: Flat-Top Receiver Efficiencies

The results from the two setups are compared in Figures 93 and 94. Because the size of the flat-top beam is much larger than the aperture of the receiver, a considerable amount of laser energy is not being utilized. Therefore, the data for the flat-top portion of the test does not extend as high as with the Gaussian test. At the lower intensities, the uniform illumination provided by the flat-top optics demonstrates a performance increase, which will have to be quantified at the higher intensities in the future with either a higher power laser or a receiver whose aperture matches the size of the flat-top beam.
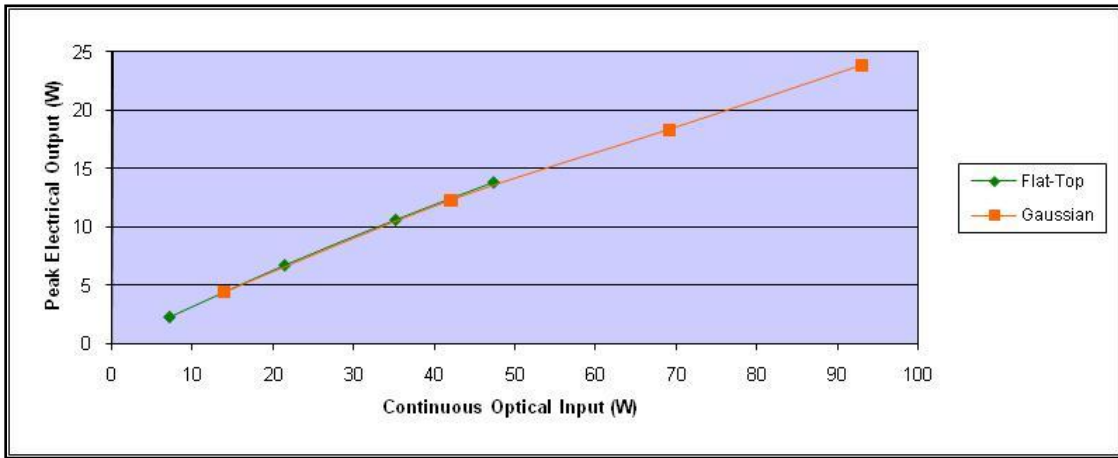
Figure 93: Gaussian vs. Flat Top Output Comparison
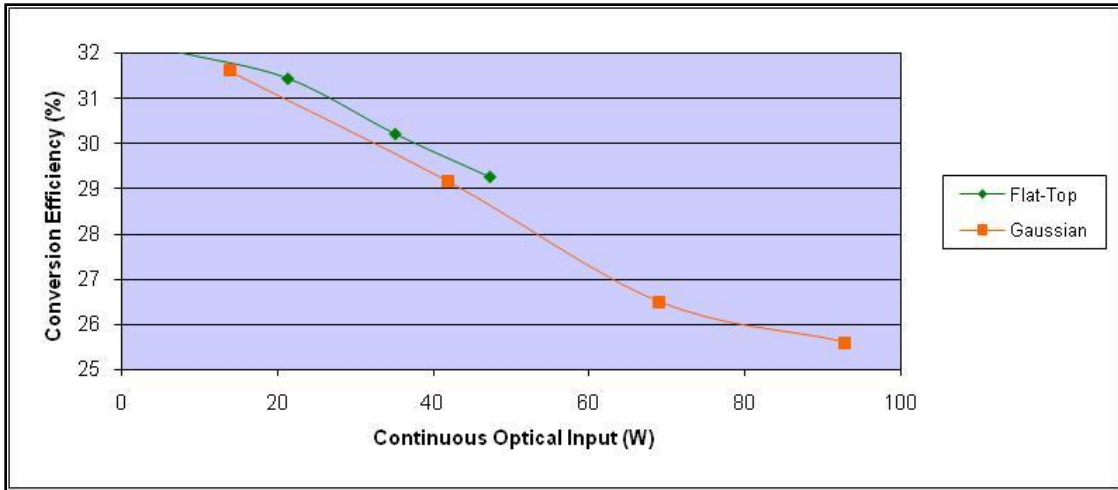
Figure 94: Gaussian vs. Flat Top Efficiency Comparison

5.6 Maximum Power Density

The objective of this test is to obtain the maximum power density performance with the available equipment. The 200 watt 980 nm laser was selected with a single cell receiver, so that the beam could be focused down to a smallest diameter possible while still illuminating the cell. As with the previous tests, the receiver position was re-adjusted in three axes to obtain the maximum output power while the laser intensity was set to for different intensities. The final alignment of the apparatus can be seen in Figure 95. It is important to note that for this test, the nominal receiver temperature was exceeded, as the concentrated amount of laser energy exceeded the capabilities of the thermal system. Despite this, the results of the test successfully exceeded all of the power density numbers thus far.
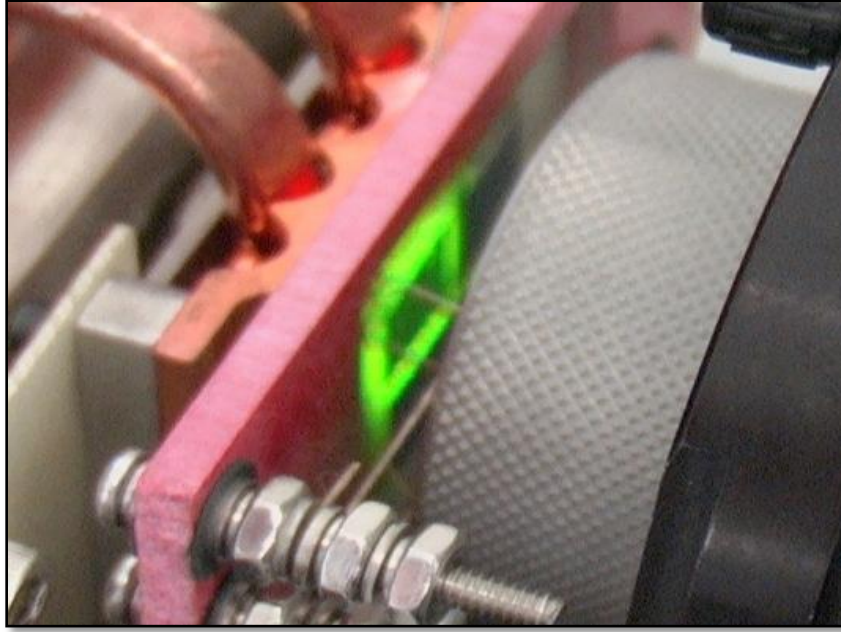
Figure 95: Maximum Power Density Alignment

TABLE VII: MAXIMUM POWER DENSITY DATA

HLU200-F400-980P2-M2			After Optical Window Transmittance Watts (W)	After Flat-Top Optics Transmittance Watts (W)	1-cell Gaussian			
Current Setpoint Amps (A)	Rated Optical Power Watts (W)	Operating Optical Power Watts (W)			Impinging Optical Power Watts (W)	VMJ Peak Power Watts (W)	Conversion Efficiency (%)	Receiver Temp. (°C)
10	30.2	28.086	26.26041	22.18794	11.1607	4.0751	36.51	31.1
20	91.2	84.816	79.30296	67.00464	33.7038	9.6017	28.49	49.4
25	121	112.53	105.21555	88.8987	44.7166	10.7461	24.03	60.5
30	150	139.5	130.4325	110.205	55.4338	7.9400	14.32	67.5
35	177	164.61	153.91035	130.0419	65.4119	2.7001	4.13	75
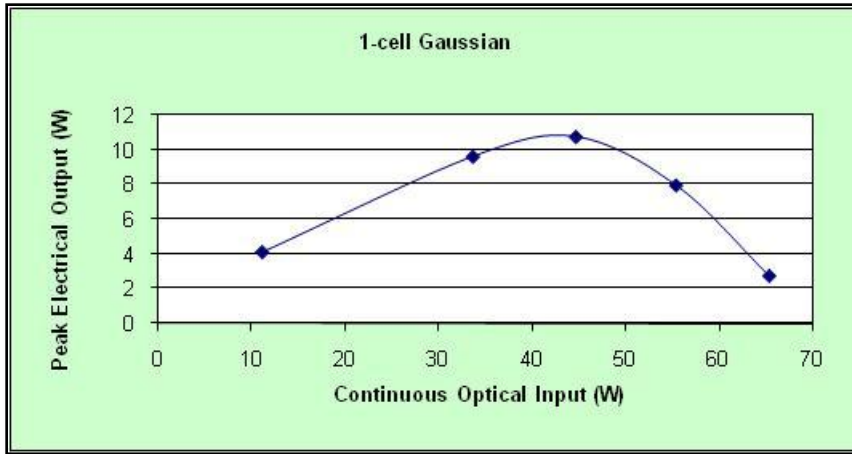
Figure 96: Maximum Power Density Output
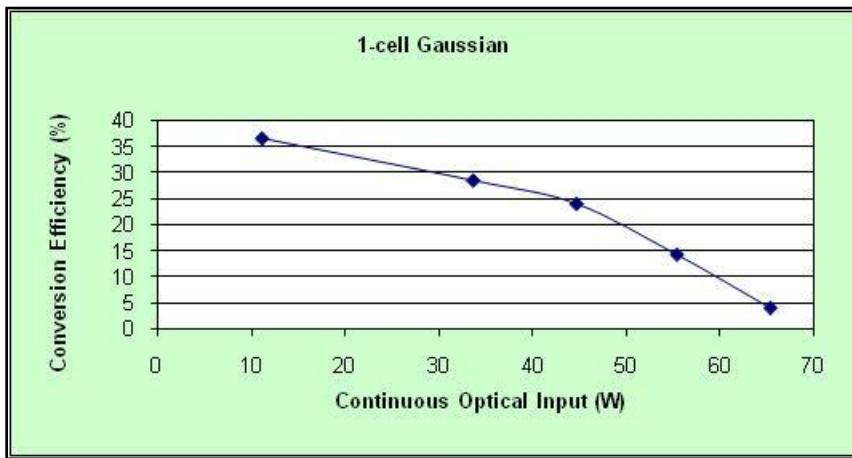
Figure 97: Maximum Power Density Efficiency

Figure 96 shows that the output of receiver peaked at 44.72 watts of laser energy, above which the performance degraded. At this peak, the optical power density was 56.6 watts per cm^2, and the single VMJ cell was able to produce 10.7461 watts (equivalent to 13.6 watts per cm^2) for a conversion efficiency of 24 %. The I-V curve for this operating point is shown in Figure 98.
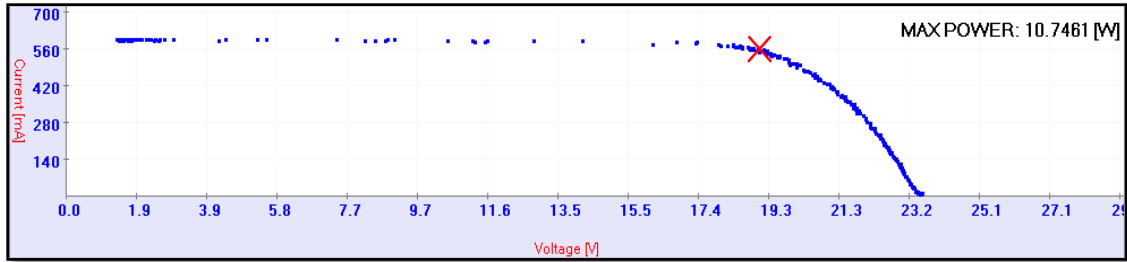
Figure 98: Maximum Power Density I-V Curve

Beyond this operating point, the performance of the cell degraded. Table VIII shows the output power and efficiency data, and the corresponding measured receiver temperatures. As the thermal system reached saturation, the receiver temperature exceeded its nominal temperature, and the conversion efficiency was consequently degraded.

TABLE VIII: RECEIVER TEMPERATURE LOG

Impinging Optical Power Watts (W)	VMJ Peak Power Watts (W)	Conversion Efficiency (%)	Receiver Temp. (°C)
11.1607	4.0751	36.51	31.1
33.7038	9.6017	28.49	49.4
44.7166	10.7461	24.03	60.5
55.4338	7.9400	14.32	67.5
65.4119	2.7001	4.13	75

The receiver temperature values are recorded by thermocouples embedded behind the mounting substrate, and so the actual temperatures at the VMJ semiconductor material are much higher than those in the table due to the delta differences between the materials in the receiver stack-up. Also, the Gaussian distribution of the beam set up an extremely intense thermal field at the center of the cell. Unfortunately, the proper

equipment was not available at the time of the experiment to image the surface temperature profile across the receiver.

Although the increasing receiver temperatures contribute to the decrease in conversion efficiency, there may be more to the explanation. Revisiting the earlier experiment with the Gaussian beam and the flat top optics gives some further insight. By plotting the efficiency of the receiver against its measured temperatures (Figure 99), an interesting trend can be observed. Up to approximately 60 °C, the efficiency degrades linearly at a slope of around 8 % per 10 °C. Above 60 °C, the efficiency drops substantially at a slope of 13 % per 10 °C. This does not match the expected thermal degradation representative of a silicon photocell (Figure 100), which is shown to be linear out to nearly 125 °C.
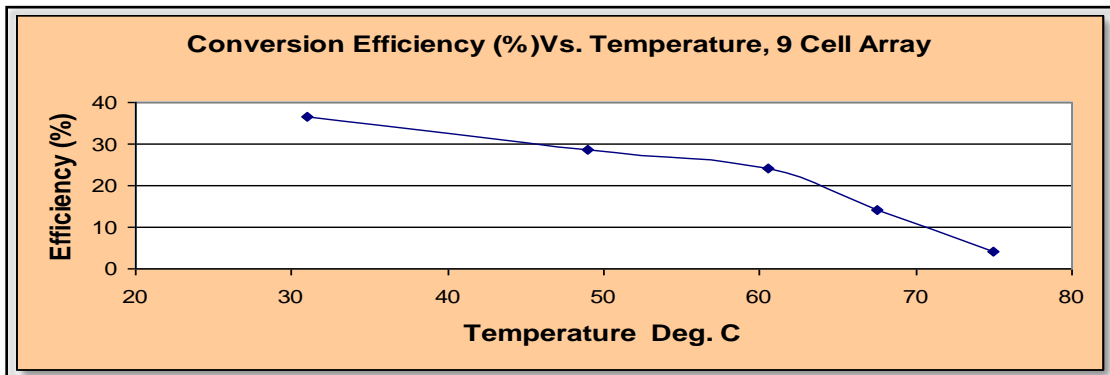
Figure 99: Efficiency Drop-off Beyond 60 °C
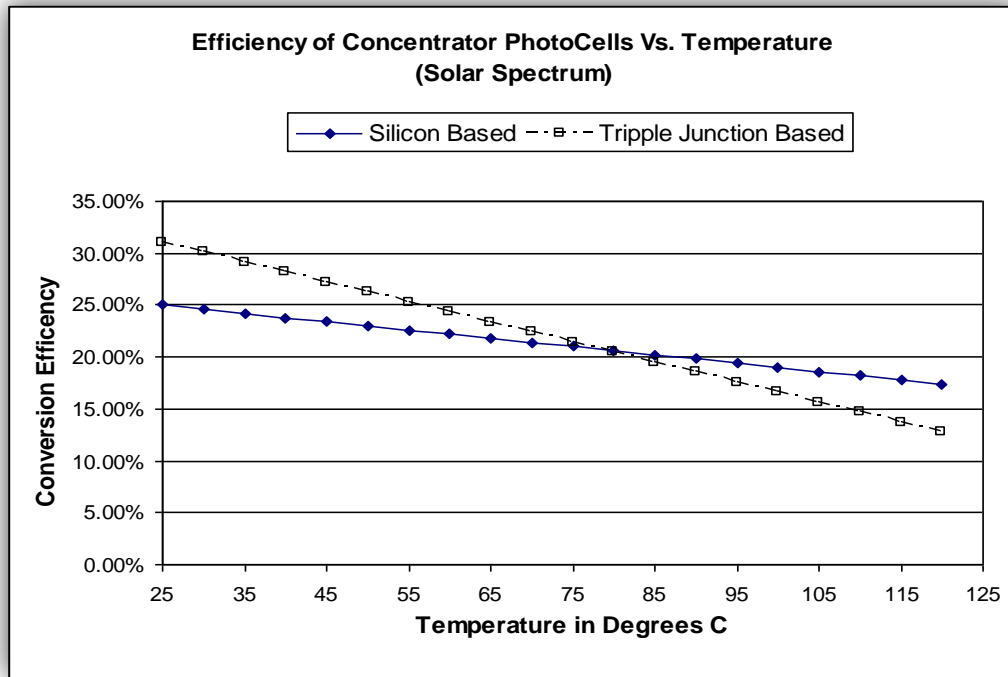
Figure 100:   Photocell Thermal Efficiency Degradation

An explanation of this phenomenon may be optical scattering & reflection off the surface of the cell, due to this hot field rejecting the energy. Evidence of this resides during the high-energy portions of the experiments, where it was observed that the laser optics were heating up due to back reflection off the receivers. The VMJ cells feature an anti-reflective (AR) coating to reduce this, and the substrate material in the receiver is a non-reflective dull surface.   Furthermore, the heating at the optics stage was only observed at high intensities, corresponding with the knee in the efficiency curve. Up to this temperature, the standard temperature de-rating applies to the receiver efficiency. Above this point some of the laser energy is reflected back away from the surface of the receiver.   Detailed pictures taken during one of the experiments may reveal this

reflection, as shown in Figures 101-104. In viewing the trend of these pictures, as the laser energy is increased a series of dark patterns are seen to develop in the center of each of the nine VMJ cells. At the high power setting in Figure 104, the patterns have grown in size to fully shroud the cells, and this may represent the refection of the laser energy. This energy reflection would explain why the efficiencies dropped significantly, as the photons were no longer able to enter the photovoltaic material. Fortunately, there are several ways to solve this problem, which are addressed in the summary.
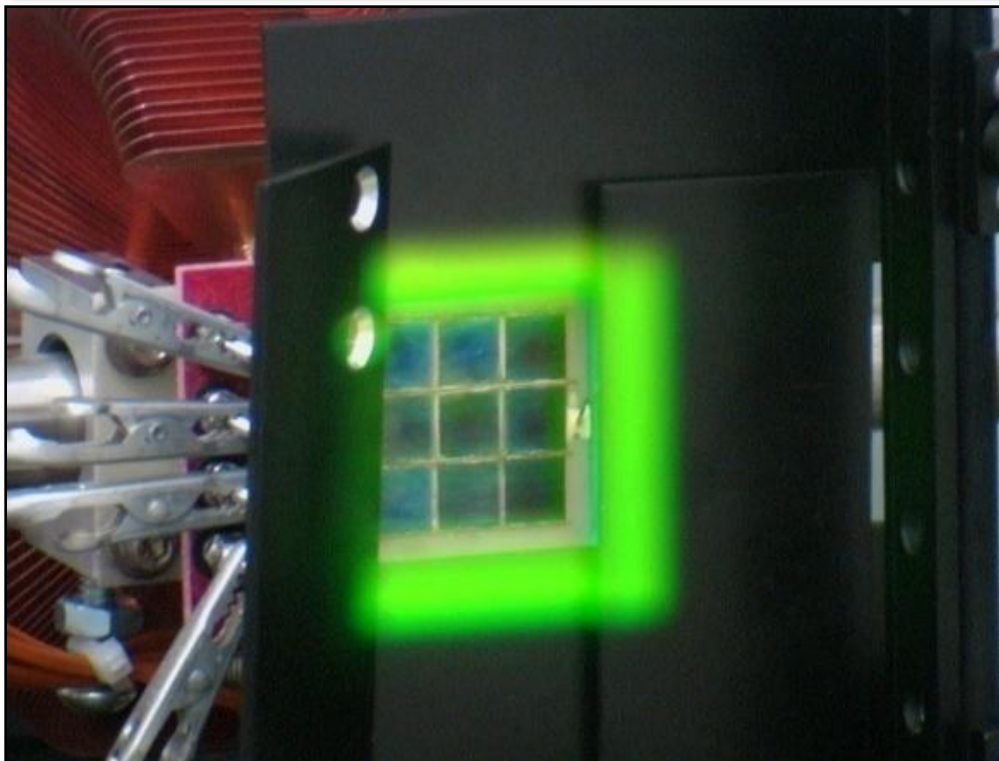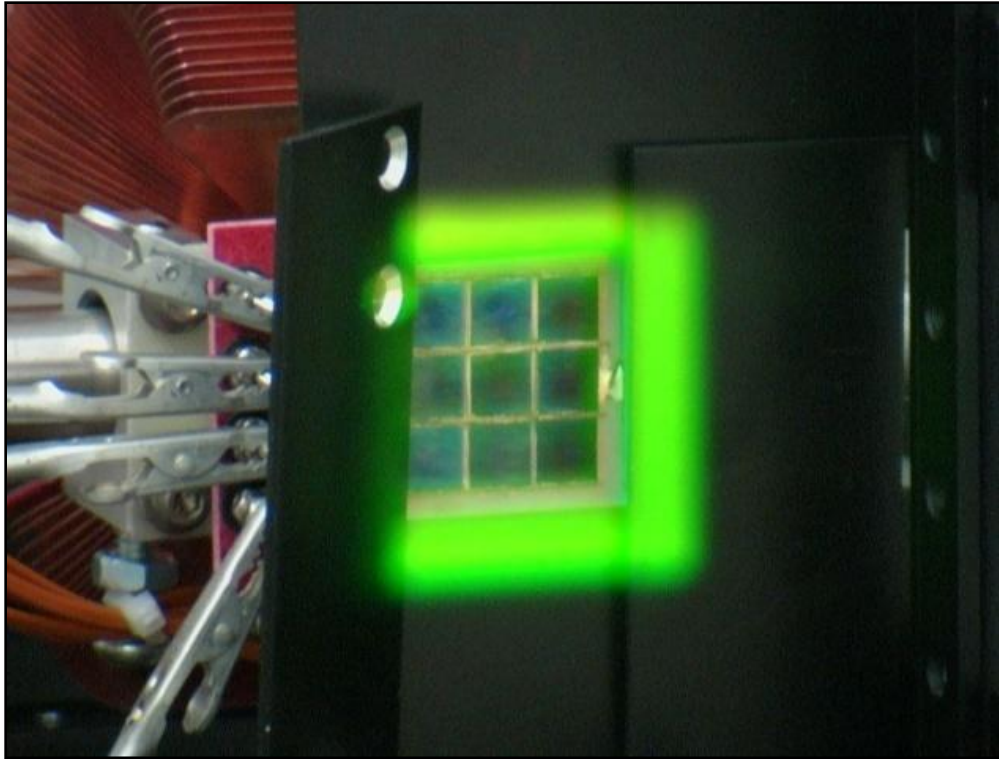
Figure 101:   Surface Reflections at 30 Watt Intensity
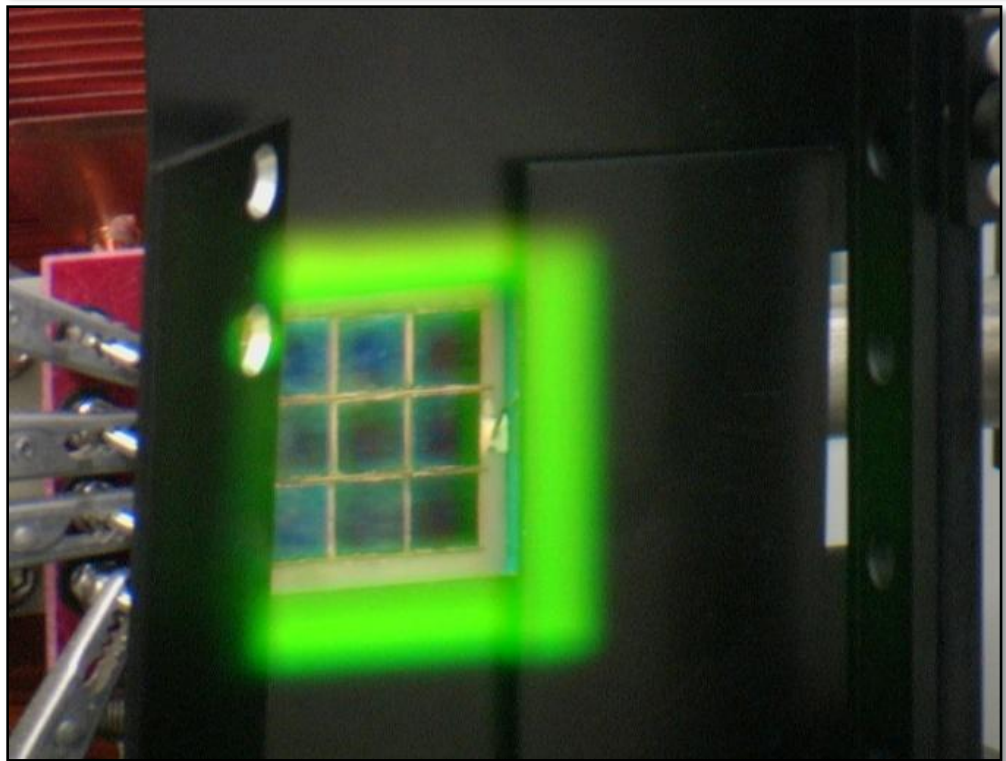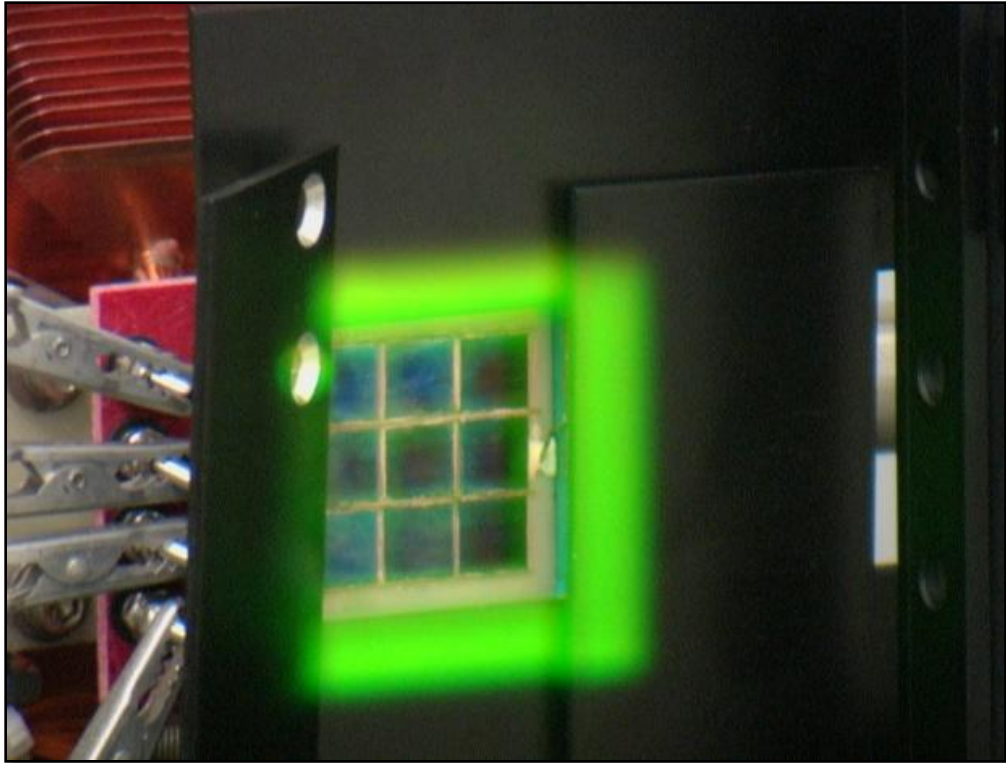
Figure 102:   Surface Reflections at 91 Watt Intensity
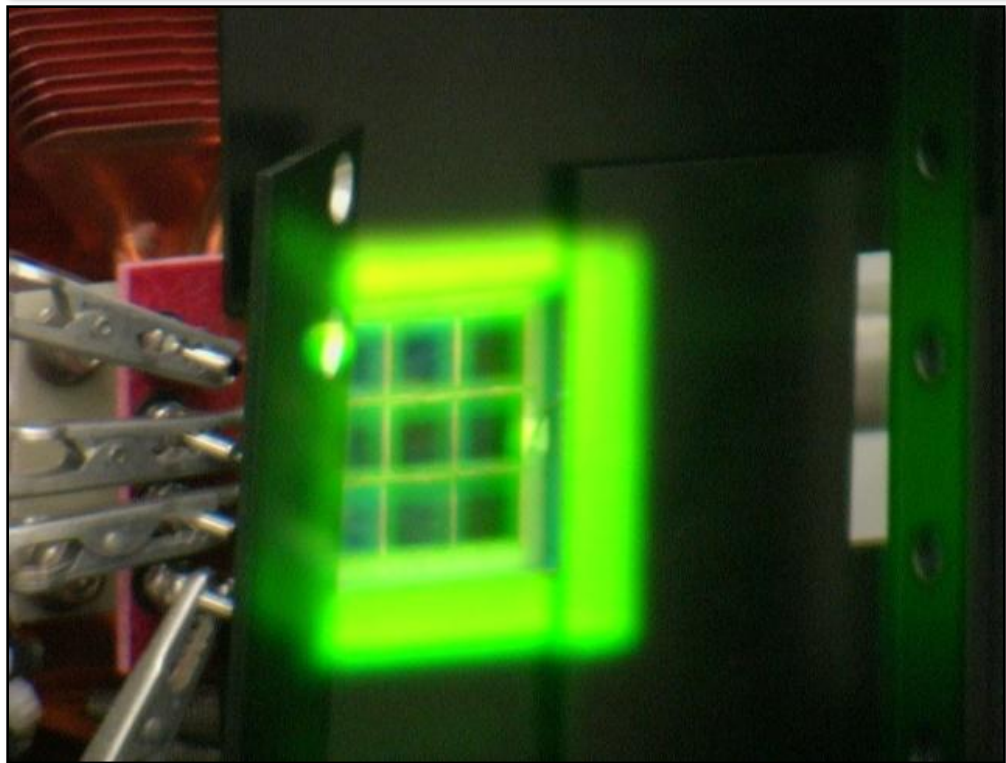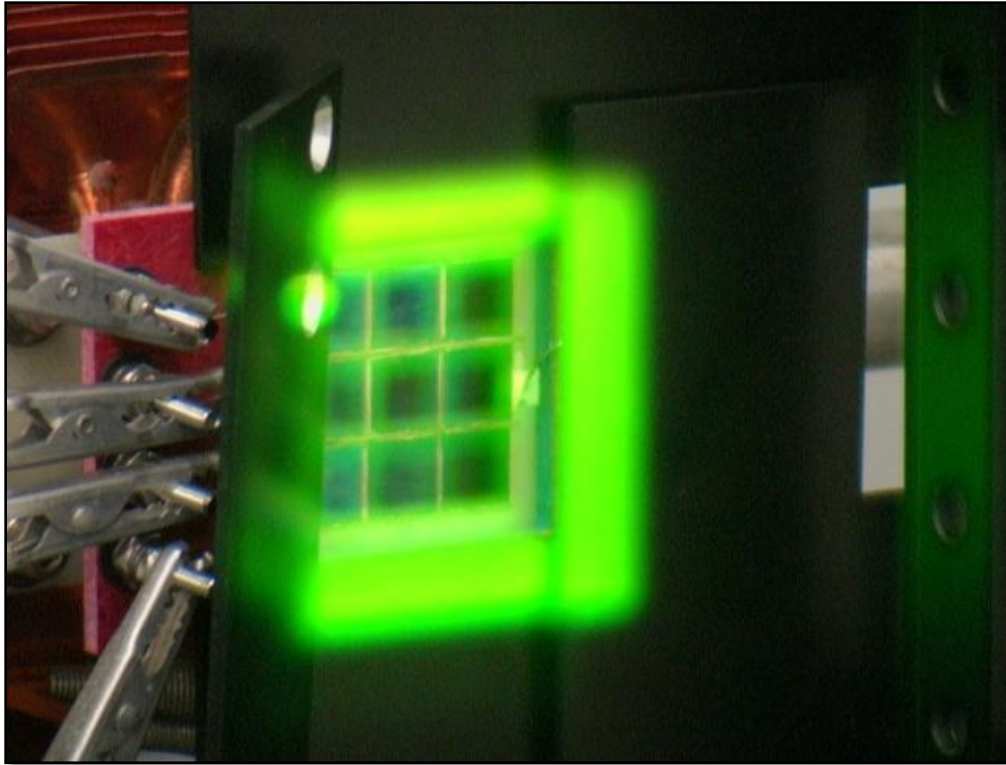
Figure 103:   Surface Reflections at 150 Watt Intensity
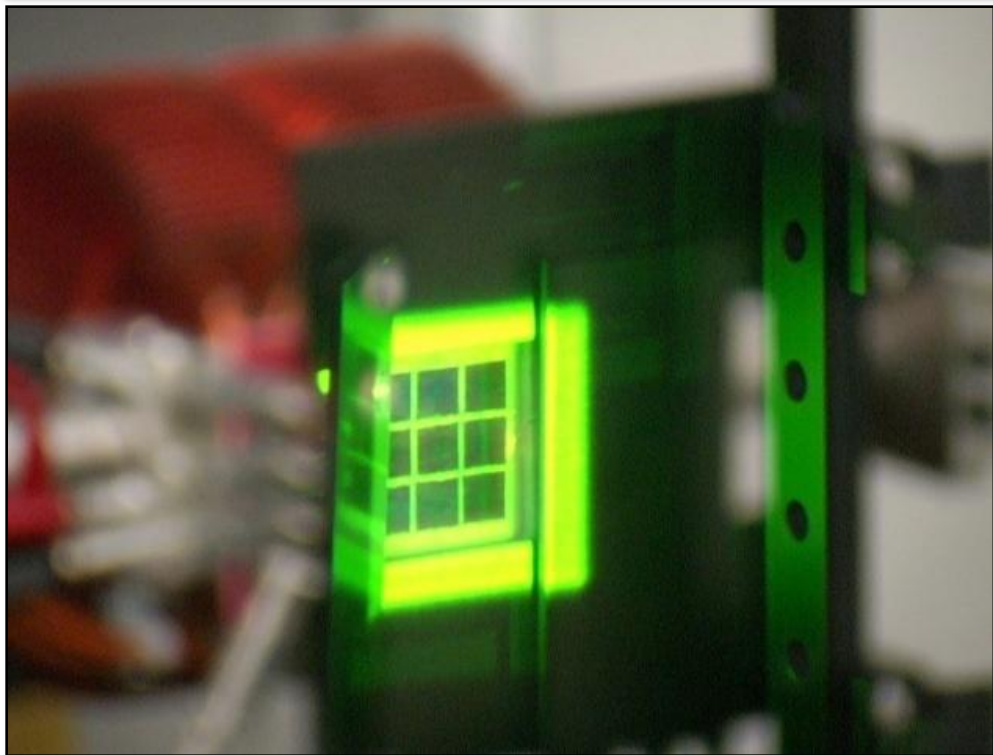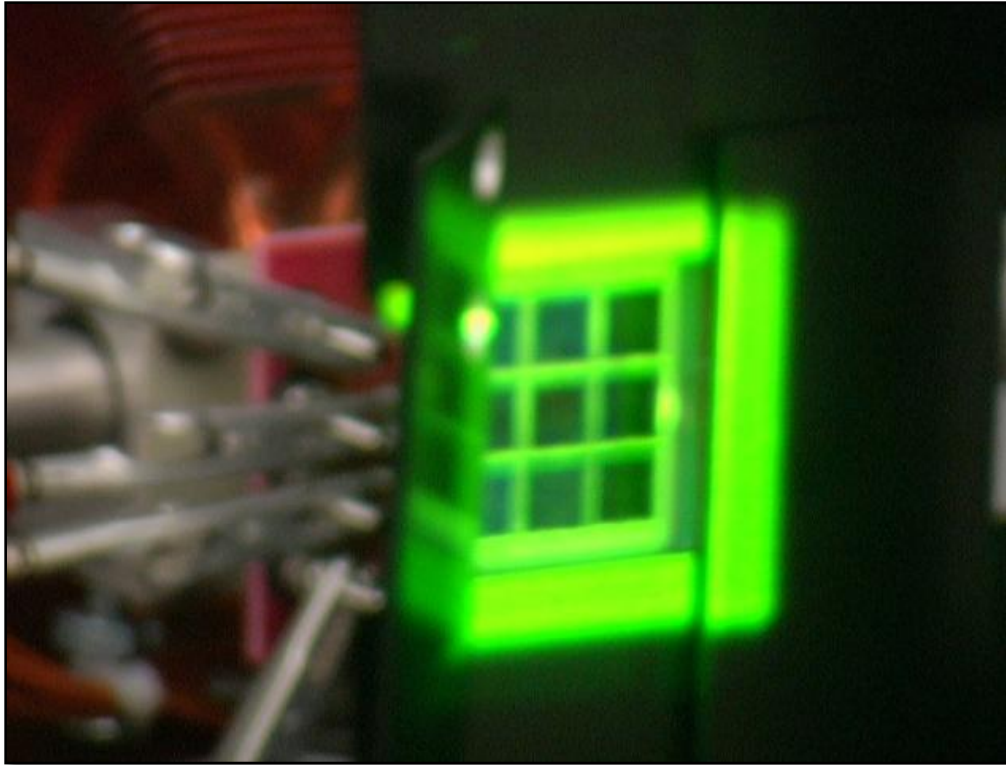
Figure 104:   Surface Reflections at 200 watt Intensity

CHAPTER VI

CONCLUSIONS AND FUTURE WORK

The primary data gathered from these experiments is instrumental in shaping the future of the HILPB program, as it progresses toward higher intensity and efficiency goals. The proof of concept objectives have been met, and further investigations into the details of the system have been performed. The following is a synopsis of the research achievements, with suggestions for future improvements.

6.1   Summary and Contributions

1. VMJ cells were successfully utilized with HILPB, and the maximum continuous power obtained from a receiver is 23.7778 watts.

2. The maximum continuous optical to electrical conversion efficiency obtained from a HILPB receiver is 49.83 % (nearing the 50-60 % theoretical limit), at low intensities with an 808 nm laser.

3. The peak power density produced by a single VMJ is 13.6 watts per cm², with an optical input 56.6 watts per cm^2.

4. The optimal frequency of the laser energy is in the 980 nm range (976 nm commercially available).

5. There is approximately a 10% absolute improvement in the efficiency of the photocells when using a uniform beam distribution versus a normal Gaussian beam.

6. The geometry of the HILPB receiver can be designed to favor the Gaussian laser beam, or the beam can be conditioned with optics to provide for a uniform distribution at the receiver.

7. The commercial off the shelf (COTS) thermal management system was not effective at keeping the temperature of the photocell array at an acceptable level during the highest power density portions of the experiments, thus resulting in drastic reductions in their conversion efficiency.

8. Conventional solar array blocking diodes are not applicable to HILPB.

The main contribution of this work was in designing, constructing and testing a preliminary engineering model of the HILPB receiver as a proof-of-concept hardware

115

device. For these initial tests, the receiver was able to meet the thermal and electrical demands of the system. With modifications to subsequent designs, the receivers were also able to be tested with a variety of laser sources to evaluate the performance of the VMJ cells for this application. These newer iterations allowed for the further investigations into parallel-cell back-feeding, optimal receiver geometry, non-uniform illumination and thermal effects at high intensities. The receivers have been tested to their capable limits, and to move forward with higher intensities and efficiencies it is necessary to design a more robust HILPB receiver.

6.2   Future Work

Further cell improvements will have an effect on the packing density of the receiver. The addition of welded leads to the VMJ cells will improve their robustness, increase the packing density and enhance the manufacturability of the receiver. The lead attachment may be accomplished through ultrasonic welding.

The excess unconvertible area due to the electrical connections between the cells could be minimized by using a substrate with embedded circuit traces, similar to a PCB. The rapid prototyping demand and the various cell configurations facilitated the usage of the delicate silver-plated kovar leads, but chemically etched bus paths directly on the receiver surface would increase the thermal conductivity and the current handling capability of the connections.

116

Another method to maximize the convertible area on the surface of the receiver would be to adjust the manufacturing of the cells in order to obtain an optimal radial geometry, in a way that reflects the Gaussian distribution of the laser beam. This could be accomplished by manufacturing the cells in a chevron shape with a taper inversely related to the Gaussian distribution, which would improve both the packing density and the uniformity of the junction illumination. An illustration of this concept is shown in Figure 105. A possible way to fabricate the angled cells may be to use laser-cutting techniques, which have been successfully employed to cut silicon wafers.
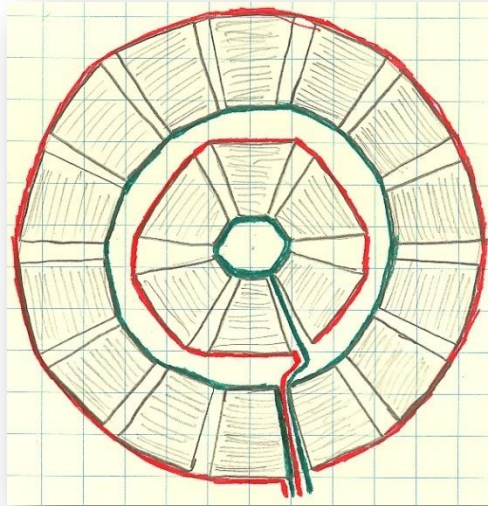
Figure 105:   Chevron Concept for a VMJ Radial Array

Another method to maximize the convertible area is to return to the original rectangular array design (made up of square VMJ cells), and condition the laser beam with optics into a flat profile. This beam manipulation could be done at either the laser or

117

the receiver end, for experimental purposes. By insuring a relatively uniform power distribution in the beam, the geometry of the receiver could be made simpler and more compact, allowing for a much higher power density.

At the very best cell efficiencies, 40-50 % of the impinging laser energy will still be lost into heat. With HILPB, large amounts of heat will be generated in a relatively small area. Although in their current form the VMJ cells are able to withstand temperatures up to 600 ºC, they do so with a considerably degraded efficiency. Therefore, thermal management is of the utmost concern in the design and operation of the HILPB system. The COTS system was effective for supporting the fundamental HILPB research, and now a new thermal management system must be designed to facilitate significantly higher energy intensities. A few preliminary designs have been constructed using anodized aluminum as the base thermal conductor, which may be ported for fluid circulation. A new mounting technique is used to attach the VMJ cells directly to the heat-sink face, eliminating the number of thermal barriers present in the receiver. This is possible since the anodized coating supplies the electrical isolation, eliminating the need for the Aluminum Nitride substrate. Kapton[TM] insulation material and copper foil may be used for the electrical routing. A new epoxy film is also being evaluated for the cell adhesion which has an improved thermal transfer rating, is dimensionally consistent and simplifies the fabrication process. Examples of this type of construction are shown in Figure 106.
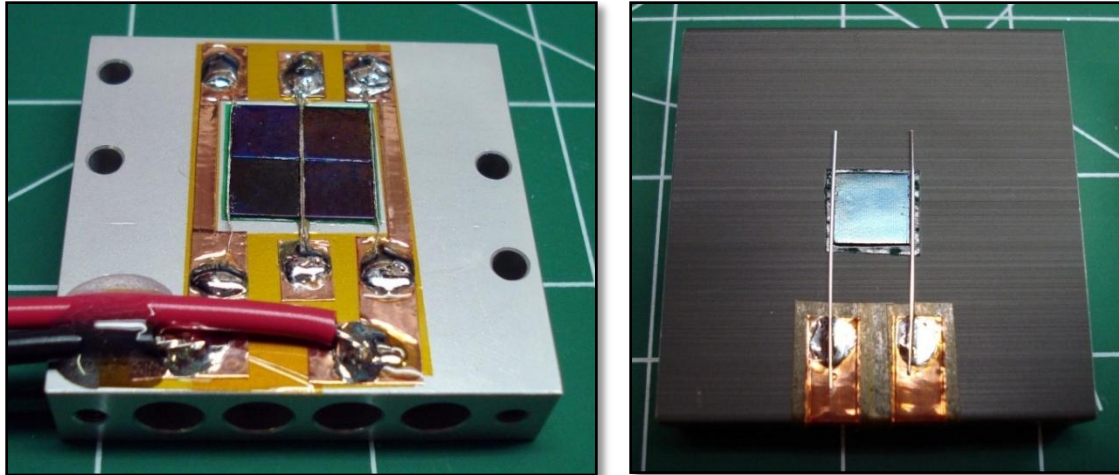
Figure 106:   Direct Bonding to Anodized Aluminum

As an alternative to dissipating the excess heat generated from HILPB, the heat may be harnessed for energy usage. An example of this would be the implementation of a fluid heat exchanger / micro-turbine system instead of a heat-sink, to convert the excess thermal energy into a usable electric form.

The energy scattering/reflection issue can be approached in a number of ways. Fundamentally, the new thermal management system will lower the overall temperature of the receiver, which will decrease the energy rejection effect. The effectiveness of other AR coatings on the surface of the cell may also be investigated. Another possibility would be to align the receiver slightly off axis from the beam. The data obtained from performing an experiment where the receiver is articulated in two different axes will provide the performance parameters for the beam tracking and control system in a HILPB system implementation.

Although the blocking diodes were more detrimental than beneficial to the overall performance of the receiver, they did correct the current flow. An active switching and control system can be developed to minimize the inherent losses resulting from unbalanced power levels from the cells caused by uneven illumination and manufacturing variability. The sensors and switches in the power electronics system need to be selected to minimize the amount of parasitic losses to the receiver. This may be accomplished through inductive current sensing and low-loss FET (field effect transistor) switches.

REFERENCES

1. Schawlow, A. L.; Townes, C. H., "Infrared and Optical Masers, " Physical Review, vol. 112, Issue 6, pp. 1940-1949, 12/1958.

2. Schawlow et al., "Masers and Maser Communications System," U.S. Patent No. 2929922, Mar 1960.

3. Tesla, N., "Apparatus for Transmission of Electrical Energy", U.S. Patent No. 649,621, May 15, 1900.

4. Tesla, N., "Means for Increasing the Intensity of Electrical Oscillations," U.S. Patent No. 685,012, Oct. 22, 1901.

5. Tesla, N., "Art of Transmitting Electrical Energy through Natural Mediums," U.S. Patent No. 787,412, April 18, 1905.

6. Tesla, N., "The Future of the Wireless Art," Wireless Telegraphy and Telephony, pg. 67-71, 1908.

7. Van Voorhies, Kurt L | Smith, James E, "Promises and prospects of worldwide wireless power transfer. An overview," Proc Intersoc Energy Convers Eng Conf, IEEE, Piscataway, NJ, (USA), vol. 4, pp. 341-346, 1991.

8. Aristeidis Karalisa, J.D. Joannopoulosb and Marin Soljačić, "Efficient wireless non-radiative mid-range energy transfer," Massachusetts Institute of Technology, Available online 27 April 2007.

9. Kurs A, Karalis A, Moffatt R, Joannopoulos JD, Fisher P, Soljacic M., "Wireless power transfer via strongly coupled magnetic resonances," Science Express on 7 June 2007, Science 6 July 2007: Vol. 317. no. 5834, pp. 83 – 86.

10. Brown, W. C., "Experimental Airborne Microwave Supported Platform," Raytheon Co Burlington, MA Microwave and Power Tube Div, Dec. 1965.

11. Jenn, D.C. Vitale, R.L., "Wireless power transfer for a micro remotely piloted vehicle," Dept. of Electr. & Comput. Eng., Naval Postgraduate Sch., Monterey, CA; Circuits and Systems, 1998. ISCAS '98. Proceedings of the 1998 IEEE International Symposium on, Publication Date: 31 May-3 Jun 1998, Volume: 6, On page(s): 590-593 vol.6.

12. NASA Video, date/author unknown, http://www.spaceislandgroup.com/biz/NASAPowerP1.mov

13. N. Shinohara, "Wireless Power Transmission for Solar Power Satellite (SPS)," Space Solar Power Workshop, Georgia Institute of Technology.

14. Brown., W. C., "The History of Power Transmission by Radio Waves". Microwave Theory and Techniques, IEEE Transactions on (Volume: 32, Issue: 9 On page(s): 1230- 1242 + ISSN: 0018-9480), September 1984.

15. J. D. Lan Sun Luk, A. Celeste, P. Romanacce, L. Chane Kuang Sang, J. C. Gatina, "POINT-TO-POINT WIRELESS POWER TRANSPORTATION IN REUNION ISLAND," 48th International Astronautical Congress, Turin, Italy, 6-10 October 1997 - IAF-97-R.4.08 - University of La Réunion - Faculty of Science and Technology.

16. Jull, G W | Lillemark, A | Turner, R M, "SHARP (Stationary High Altitude Relay Platform) Telecommunications missions and systems," GLOBECOM '85 - Global Telecommunications Conference, New Orleans, LA, Conference Record , Volume 2; UNITED STATES; 2-5 Dec. 1985. pp. 955- 959, 1985.

17. Fujino, Y., M. Fujita, N. Kaya, S. Kunimi, M. Ishii, N. Ogihata, N. Kusaka, and S. Ida, "A Dual Polarization Microwave Power Transmission System for Microwave propelled Airship Experiment," Proc. of ISAP'96, Vol.2, 1996, pp.393-396.

18. Cummings, T.; Janssen, J.; Karnesky, J.; Laks, D.; Santillo, M.; Strause, B.; Myrabo, L. N.; Alden, A.; Bouliane, P.; Zhang, M., "6 GHz microwave power-beaming demonstration with 6-kV rectenna and ion-breeze thruster," AIP Conference Proceedings Second International Symposium on Beamed Energy Propulsion n 702 2004 p.430-42.

19. Yang, G.; Ali, M.; Dougal, R., "A multi-functional stacked patch antenna for wireless power beaming and data telemetry," 2005 IEEE Antennas and Propagation Society International Symposium 2005 p.359-62 vol. 2A.

20. Myrabo, L. N., "Microwave power beaming infrastructure for manned lightcraft operations," AIP Conference Proceedings Fourth International Symposium on Beamed Energy Propulsion n 830 2006 p.651-62.

21. Ortabasi, U.; Friedman, H., "Powersphere: a photovoltaic cavity converter for wireless power transmission using high power lasers," Conference Record of the 2006 IEEE 4th World Conference on Photovoltaic Energy Conversion 2006 p.4 pp.

22. Blackwell, T., "Recent demonstrations of laser power beaming at DFRC and MSFC," AIP Conference Proceedings Beamed Energy Propulsion. Third International Symposium on Beamed Energy Propulsion n 766 2005 p.73-85.

23. Author Unknown, "To infinity ... and beyond! [power beaming for interplanetary vehicles]," Machine Design International v 79 n 5 2007 p.78, 80, 82, 84, 86, 88.

24. Brandhorst, H. W. , Jr., "POWOW: power without wires: a SEP concept for space exploration," IEEE Aerospace and Electronic Systems Magazine v 16 n 2 2001 p.3-7.

25. Edwards, B. C.; Bennett, H. E., "Space elevator feasibility test using laser power beaming," Proceedings of the SPIE - The International Society for Optical Engineering Laser and Beam Control Technologies v 4632 2002 p.141-7.

26. Luce, R.; Michael, S., "An experiment to demonstrate spacecraft power beaming and solar cell annealing using high-energy lasers," AIP Conference Proceedings Beamed Energy Propulsion. First International Symposium n 664 2003 p.461-72.

27. Einstein, A., " On the Heuristic Viewpoint Concerning the Production and Transformation of Light," Annalen der Physik, in AJP, 33, No. 5, May (1965).

28. Marales, Rolf Allan Lunders, "Performance of Advanced Triple-Junction (ATJ) Solar Cells," Pontificia Universidad Catolica De Chile, Escuela De Ingenieria, 2005.

29. Sater, B.L. Sater, N.D., "High voltage silicon VMJ solar cells for up to 1000 suns intensities," Photovoltaic Specialists Conference, 2002. Conference Record of the Twenty-Ninth IEEE, Publication Date: 19-24 May 2002, On page(s): 1019- 1022, ISSN: 1060-8371, ISBN: 0-7803-7471-1.

30. Sater, B., "The effectiveness of the Photovolt VMJ Cell Technology," Photovolt Inc., 2005, http://users.adelphia.net/~esch/papers/The_effectiveness_VMJ_Cell_Technology.pdf

31. Goradia, C | Sater, B L, "A first order theory of the p/+/-n-n/+/ edge-illuminated silicon solar cell at very high injection levels," IEEE Transactions on Electron Devices. Vol. ED-24, pp. 342-351. Apr. 1977.

32. Alda, Javier, "Laser and Gaussian beam propagation and transformation," University Complutense of Madrid, Madrid, Spain, Encyclopedia of Optical Engineering, 2003.

33. Jain, R. K.; Landis, G. A., "Transient response of gallium arsenide and silicon solar cells under laser pulse," Solid-State Electronics v 42 n 11 1998 p.1981-3 – 5Mhz Si & 1-2GHz GaAs.

34. Andreev, V.; Khvostikov, V.; Kalinovsky, V.; Lantratov, V.; Grilikhes, V.; Rumyantsev, V.; Shvarts, M.; Fokanov, V.; Pavlov, A., "High current density GaAs and GaSb photovoltaic cells for laser power beaming," Proceedings of 3rd World Conference on Photovoltaic Energy Conversion 2003 p.761-4 Vol.1.

35. Krupke, W. F.; Beach, R. J.; Kanz, V. K.; Payne, S. A.; Early, J. T., "New class of cw high-power diode-pumped alkali lasers (DPALs)," (plenary paper). Proceedings of the SPIE - The International Society for Optical Engineering High Power Laser Ablation V v 5448 n 1 2004 p.7-17.

36. Krupke, W. F.; Beach, R. J.; Payne, S. A.; Kanz, V. K.; Early, J. T., "DPAL: a new class of lasers for cw power beaming at ideal photovoltaic cell wavelengths," AIP Conference Proceedings Second International Symposium on Beamed Energy Propulsion n 702 2004 p.367-77.

37. Cook, J. R., "Atmospheric propagation of high energy lasers and applications," AIP Conference Proceedings Beamed Energy Propulsion. Third International Symposium on Beamed Energy Propulsion n 766 2005 p.58-72.

38. Cook, J. R.; Cusumano, S. J.; Whiteley, M. R., "Potential use of CW high energy laser on an airborne platform," AIP Conference Proceedings Fourth International Symposium on Beamed Energy Propulsion n 830 2006 p.400-10.

39. Stepanov, V. V.; Alekseyev, V. N.; Osipov, V. A.; Rezunkov, Y. A.; Sheremetyeva, T. E., "Laser beam control system to compensate the turbulent distortions of laser beam at introducing a lead angle," Res. Inst. for Complex Testing of Opto-electronic Devices, Leningrad Region, Russia, AIP Conference Proceedings. no.702 2004, p 283-92, 2004.

40. Kantrowitz, Arthur, "Propulsion to orbit by ground-based lasers," Astronautics & Aeronautics, vol. 10, no. 5, May 1972, p. 74, 75; Propulsion techniques - Action and reaction (A98-24576 05-20), Reston, VA, American Institute of Aeronautics and Astronautics, Inc., 1998, p. 351-353.

41. Edmund J. Conway, "Laser Power Transmission," NASA SP-509, Volume 2, Johnson Space Center, JAN 1, 1992.

42. Holloway, P F | Garrett, L B, "Comparative analyses of space-to-space central power stations," NASA TP-1955, Dec. 1981.

43. deYoung, R J | Tepper, W D | Conway, E J | Humes, D H, "Preliminary comparison of laser and solar space power systems," IECEC '83; Proceedings of the Eighteenth Intersociety Energy Conversion Engineering Conference, Orlando, FL, Volume 3; United States; 21-26 Aug. 1983. pp. 983-989. 1983.

44. Zapata, L E | deYoung, R J, "Flashlamp-pumped iodine monobromide laser characteristics," Journal of Applied Physics. Vol. 54, pp. 1686-1692. Apr. 1983.

45. Harries, W L | Meador, W E, "Kinetic modeling of an IBr solar pumped laser," Space Solar Power Review. Vol. 4, no. 3, pp. 189-202. 1983.

46. Weaver, W R | Lee, J H, "Solar pumped gas laser for the direct conversion of solar energy," J. ENERGY. Vol. 7, no. 6, pp. 498-501. 1983.

47. Wilson, J W | Lee, Y | Weaver, W R | Humes, D H | Lee, J H, "Threshold kinetics of a solar-simulator-pumped iodine laser," NASA TP-2241, Feb. 1984.

48. deYoung, R J, "Low threshold solar-pumped iodine laser," IEEE Journal of Quantum Electronics. Vol. QE-22, no. 7, pp. 1019-1023. 1986.

49. Insuik, R J | Christiansen, W H, "A radiatively pumped CW CO2 laser," IEEE Journal of Quantum Electronics. Vol. QE-20, pp. 622-625. June 1984.

50. deYoung, R J | Higdon, N S, "A blackbody-pumped CO2-N2 transfer laser," NASA TP-2347, Aug. 1984.

51. Akhmanov, Sergei A., Vysloukh, Viktor A., Chrkin, Anatolii S., "Optics of femtosecond laser pulses", Izdatel'stvo Nauka, 1988.

52. Alvidres, H., Hoetger, D., Fischer, M., "Thermal Control System Design," Texas Space Grant Consortium, 1995.

53. Bujard, P., "Thermal conductivity of boron nitride filled epoxy resins: temperature dependence and influence of sample preparation," Ciba-Geigy Ltd., Fribourg: Thermal Phenomena in the Fabrication and Operation of Electronic Components: 1-THERM '88, Inter Society Conference on; 11-13 May 1988.

54. Miwa, K.; Fukumoto, A., "First Principles Calculation of the structural, electronic and vibrational properties of gallium nitride and aluminum nitride ," *Physical Review B*, Volume 48 Number 11, Sptepember 15, 1993.

55. Liu, G; Cui, B; Chen, R J., "Thermal Expansion Behavior of Copper/Kovar Alloy Composite ," Northeast Univ. Technol. (China). Vol. 9, no. 4, pp. 498-501. Dec. 1988.

56. Daoqiang Lu; Tong, Q.K.; Wong, C.P., "Conductivity mechanisms of isotropic conductive adhesives (ICAs) ," Electronics Packaging Manufacturing, IEEE Transactions on [see also Components, Packaging and Manufacturing Technology, Part C: Manufacturing, IEEE Transactions on] , vol.22, no.3pp.223-227, Jul 1999.

57. Horowitz, Paul; Hill, Winfield, "The Art of Electronics ," Second Edition, Cambridge University Press, 1989.

58. Wong, Wayne A., Macosko, Robert P., "Refractive Secondary Concentrators for Solar Thermal Applications," SAE, AIAA, ASME, IEEE, AIChE, and ANS, IECEC - Intersociety Energy Conversion Engineering Conference, 34th, Vancouver, Canada; UNITED STATES; 2-5 Aug. 1999. 1999.

59. Ferriere, A | Rodriguez, G P | Sobrino, J A, "Flux distribution delivered by a Fresnel lens used for concentrating solar energy," Journal of Solar Energy Engineering (Transactions of the ASME). Vol. 126, no. 1, pp. 654-660. Feb. 2004.

60. Noor Mohammad, S | Abidi, S T H, "Theory of saturation photocurrent and photovoltage in p-n junction solar cells," Journal of Applied Physics. Vol. 61, pp. 4909-4919. 15 May 1987.

61. Edward D. Palik, "Handbook of Optical Constants of Solids," Academic Press, NY, 1985.

APPENDICES

TABLE IX: HILPB Receiver Construction Log

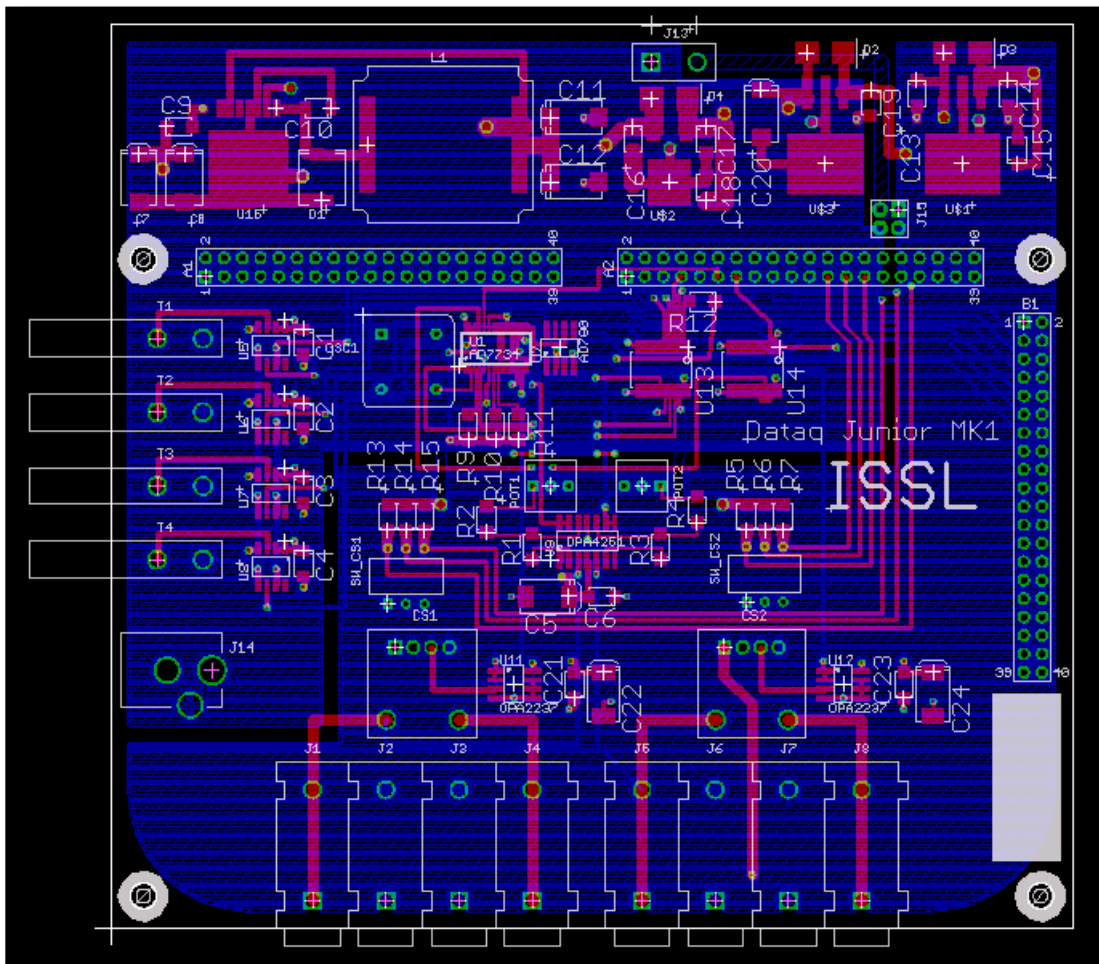| Construction Log		
Designator	**Cells**	**Notes**
MK-I	H3-14	single, consistant side down, lead ripped off during testing
	H3-11	obscured during assembly
MK-IB	E12-11	rebuild double, consistant side up
	H3-33	rebuild double, consistant side down
MK-II	E12-4	single, consistant side up, lead ripped off during testing & repaired at Northrop
		experienced a burn to the AR coating from the Gaussian laser set to 110W
MK-IIB	K3-5	rebuild single
		consistant side up
MK-III	K1-C	double, IR coating, thick cell
	SCA9-A	double, IR coating, small cell
MK-IV	K3-23	double, IR coating
	SCA9-B	double IR coating, small cell
MK-V	E12-10	top left corner
	E12-13	top right corner
	H3-7	bottom right corner
	F1-5	bottom left corner
MK-VI	K1-B	top left corner
	K3-3	top center
	K3-4	top right corner
	K3-15	right center
	K3-20	bottom right corner
	K3-19	bottom center
	K3-17	bottom left corner
	K3-8	left center
	K3-12	center
MK-VII	K3-1	top left corner
	K3-27	top center
	E12-8	top right corner
	E12-20	right center
	K3-11	bottom right corner
	E12-17	bottom center
	E12-18	bottom left corner
	K3-10	left center
	F3-13	center
MK-VIII-A (radial)	H3-5	top left corner
	K5-19	top center
	H1-14	top right corner
	K12-13	right center
	H1-29	bottom right corner
	K7-16	bottom center
	H1-31	bottom left corner
	K12-3	left center
	K11-9	center
	SCA9-D	top-right small cell
	SCA9-E	bottom-left small cell

126

Figure 107:   DATAQ PCB Artwork